THEORETICAL AND EXPERIMENTAL INVESTIGATIONS IN CHARACTERIZING AND DEVELOPING MULTIPLEXED DIAMOND-BASED NEUTRON SPECTROMETERS

A Dissertation

Presented to

The Faculty of the Graduate School

At the University of Missouri

In Partial Fulfillment

Of the Requirements for the Degree

Doctor of Philosophy

By

ERIC LUKOSI

Dr. Mark Prelas, Dissertation Supervisor

MAY 2012

The undersigned, appointed by the dean of the Graduate School,

have examined the Dissertation entitled

THEORETICAL AND EXPERIMENTAL INVESTIGATIONS IN CHARACTERIZING AND DEVELOPING MULTIPLEXED DIAMOND-BASED NEUTRON SPECTROMETERS

Presented by Eric Lukosi

A candidate for the degree of

Doctor of Philosophy

And hereby certify that, in their opinion, it is worthy of acceptance.

_____

Professor Mark Prelas

_____

Professor Sudarshan Loyalka

_____

Professor William Miller

_____

Professor Tushar Ghosh

_____

Professor Gavin King

The work presented here was made most possible through the everlasting support and love of my wife, Michelle, who tolerated the long hours it took to complete this work. Next is my father, who supported my academic and athletic pursuits all my life, teaching me that a healthy individual comes from both physical and mental exercise. His dedication to me resulted in the successes of my undergraduate studies. Finally, I would like to dedicate this work to my mother, since it is her who taught me that I am capable of achieving anything I put my mind to.

ACKNOWLEDGEMENTS

I would like to thank my advisor, Professor Mark Prelas, for giving me the opportunity of developing a research project under his guidance. This has allowed me the experiences of learning how to formulate and develop research, something that few graduate students get the opportunity to do.

I am also grateful to the other faculty members and staff at the Nuclear Science and Engineering Institute. Their support created a great atmosphere in which to learn and grow, both academically and socially. I would also like to thank John Palsmeier for his contributions to this work.

Finally, I would like to thank the following for providing financial support for my research: The U.S. Department of Education through the Graduate Assistance in Areas of National Need (GAANN) fellowship and the NRC grant 38-09-943.

TABLE OF CONTENTS

Acknowledgements....ii

LIST OF FIGURES....v

LIST OF TABLES....x

Abstract....xi

1. Introduction.... 1

2. Methods of Neutron Radiation Detection 3

2.1 Liquid Scintillation Counters 3

2.2 Neutron Capture 4

2.3 Super Heated Fluid.... 8

2.4 Elastic Recoil.... 9

3. Background in Diamond Based Neutron Detection 14

3.1 Neutron and Heavy Ion Interactions 15

3.2 Electron and Photon Interactions.... 18

3.3 Radiation Hardness.... 25

3.4 Electrical Properties.... 30

3.5 Diamond-Based Radiation Detector History.... 38

4. Single Plate Diamond-based Spectroscopic Neutron Detector Simulations.... 40

4.1 Simulation Software.... 41

4.2 Initial Investigations on Simulation Methodology and Detector Response to Neutron Reference Fields 44

4.3 Preliminary Simulations Comparing the Simulation Methodologies 44

4.4 Diamond Detector Exposure to Various Monoenergetic Neutrons Reference Fields 51

5. Multiplexed Diamond Arrays for Neutron Detection 56

5.1 Diamond Deficiencies, Multiplexing, and Simulating Charge Collection Efficiency 56

5.2 Post Processing For Multiplexed Array Simulations 61

5.3 14.1 MeV Neutrons and Multiplexing 63

5.4 Conclusions For the Simulated Multiplexing of Diamond Plates for Neutron Detection 78

5.5 Photon Interactions with Diamond and Multiplexed Diamond Arrays 80

6. Experimental Results 85

6.1 Electronic Grade Diamond Sample Characterization 85

6.2 Electronic Grade Diamond Sample Preparation 89

6.2.1 Electrical Contact Scheme 89

6.2.2 EGDS Cleaning and Metallization Process 92

6.3 Electrical Characterization of EGDSs 97

6.3.1 Current-Voltage Measurements 97

6.3.2 Alpha Particle Exposures 100

6.4 Series Multiplexing and Alpha Exposures 109

6.5 Pu/Be Neutron Source and Parallel Multiplexing 120

7. Conclusion 133

Bibliography 136

Vita 141

LIST OF FIGURES

Figure 1: Mass attenuation and mean free path of gamma rays in diamond. 21

Figure 2: Electron ranges in diamond. 23

Figure 3: e^--h pair creation per unit path length for carbon ions and electrons in diamond. 24

Figure 4: Monte Carlo simulation results on a single diamond plate for a) 2 MeV neutrons simulated with MCNP-PoliMi and the ENDF/B-VII and TENDL libraries and b) the differential scattering cross section calculated for these simulations. In part c) experimentally determined pulse height spectra for various monoenergetic neutron reference fields are shown from Zimbal *et al.* for the exposure of a similar diamond plate.[20] For further comparison of these simulation methodologies d) the simulation results from a 14.1 MeV monoenergetic neutron reference field. 46

Figure 5: MCNPX 2.7 simulation results for a) 0.5-5 MeV, b) 5.5-10 MeV, and c) 12-20.1 MeV neutron reference fields. Part d) shows a comparison between the ISABEL/Dresner (solid line) and ENDF/B-VII libraries (dashed line). 52

Figure 6: The neutron induced $^{12}C(n,\alpha)^{9}Be$ reaction cross section plotted against the results from the MCNPX 2.7 simulation results 55

Figure 7: Pictorial representation of specific stacking types of a) series and b) parallel multiplexing configurations. 58

Figure 8: Representation of the mathematical analysis of the MCNPX pulse height tally output of an a) series multiplexed and b) parallel multiplexed diamond detectors through spatial binning. 62

Figure 9: Plot of the charge collection efficiency versus normalized charge creation location across series multiplexed arrays of one, three, five, eight, ten, fifteen, and twenty plates in size. 65

Figure 10: Simulation results showing the difference in the pulse height spectra of single diamond plates for a) series and b) parallel multiplexing from an impinging 14.1 MeV neutron reference field. The difference in the pulse height spectra of the series and parallel multiplexing techniques is shown in c) and the FWHM of the single diamond plate parallel multiplexing technique is shown in d). 68

Figure 11: Pulse height spectra for the series (left) and parallel (right) multiplexing technique for three (a-b), five (c-d), and eight (e-f) plate array thicknesses. 72

Figure 12: Pulse height spectra for the series (left) and parallel (right) multiplexing technique for ten (a-b), fifteen (c-d), and twenty (e-f) plate array thicknesses. 73

Figure 13: Results from photon expsoures to series multiplexed diamond arrays for energies of a) and b) 500 keV, c) and d) 650 keV, and e) and f) 800 keV. 82

Figure 14: Results from photon expsoures to series multiplexed diamond arrays for energies of a) and b) 500 keV, c) and d) 650 keV, and e) and f) 800 keV. 83

Figure 15: Raman spectrum of EGDS 3. 86

Figure 16: The a) experimenal apparatus used to detetermine the spectral abosrbance of EGDS 1-8 and b) the results of this analysis for EGDS 3. 88

Figure 17: Thermal annealing temperature-time curve followed for the EGDSs during preparation. 96

Figure 18: Picture of fully prepared EGDS ready for experiments. 97

Figure 19: In part a) the measurement system used for the IV measurments is shown. In parts b) thorugh d) the IV characteristics of EGDS 1-8 are displayed. 99

Figure 20: In part a) the diagram of the EGDS mounting sample is displayed and the actual detector housing is shown in b). 101

Figure 21: ^{210}Po high activity source spectrum used for the EGDS exposures. 102

Figure 22: Basic circuit diagram describing the electronics used in all EGDS radiation measurements. 103

Figure 23: The spectral results from ^{210}Po alpha exposures on EGDS 1 with a varying applied voltage is displayed in a) and one of these curve with error bars found through Poisson statistics is shown in b). 105

Figure 24: CCE measurements using a positive bias for EGDS 1-8 in a)-f), respectively. 107

Figure 25: CCE measurements using a negative bias for EGDS 1-8 in a)-f), respectively. 108

Figure 26: Measured ^{210}Po alpha spectra for a series multiplexed array of EGDs one and two is shown in a) and the determined charge collection efficiency versus applied electric field is shown in b). 110

Figure 27: The simplified block diagram of the diamond detection system attached to the PC142 preamplifier in a) with b) a single diamond plate in bias, c) a diamond during a radiation interaction and d) two diamond plates in series where the diamond plate between the ground and the other diamond plate is under the influence of a radiation interaction..... 113

Figure 28: The current pulse introudced to the system is given in a), the current seen by the front end capacitor of the preamplifier is given in b), and the voltage rise and drop of the output of the preamplifier is given in parts c) and d), respectively..... 115

Figure 29: PSpice simulation results for the series multiplexing of two diamond plates in response to alpha particle interactions where a) the current pulse source, b) the current on the parallel capacitor with the current source or EGDS 1, c) the current on the parallel capacitor of EGDS 2, d) the current generated on front end capacitor of the PC142PC preamplifier, e) the voltage output rise and f) the decay of that voltage pulse from the 142PC preamplifier. 119

Figure 30: Neutron emission spectra for ^{252}Cf and Pu/Be neutron sources..... 123

Figure 31: Experimental setup of the exposure of each EGDS to a Pu/Be neutron source. 125

Figure 32: Measured pulse height spectrum induced by a Pu/Be neutron source on EGDSs a) one and two, b) three and four, c) five and six, and d) seven and eight..... 125

Figure 33: Picture of the parallel multiplexing of EGDSs 1-8..... 127

Figure 34: Spectral response of parallel multiplexed EGDSs 1-8 to a Pu/Be neutron source. 128

Figure 35: MCNPX simulation results for the expected pulse height spectrum on a single diamond plate using a Pu/Be source. 130

Figure 36: PSpice simulation results for the parallel multiplexed array for EGDSs 1-8. In a) the current across one of capacitors parallel to the current source is given. In b) the current through the input capacitor to the preamplifier is shown, and in c) and d) the output voltage from the preamplifier is given. 132

LIST OF TABLES

Table 1: Neutron interactions with natural carbon 17

Table 2: Electron interaction parameters with diamond. 23

Table 3: Energy peaks from the 20.1 MeV neutron induced pulse height spectrum using ISABEL/Dresner physics models..... 53

Table 4: Basic electronic characteristics of multiplexing..... 66

Table 5: $^{12}C(n,\alpha_o)^{9}Be$ 8.4 MeV peak analysis for varying multiplexing configurations..... 70

Table 6: Comparison of intrinsic detection efficiency calculated from diffusion theory and MCNPX with increasing active detection volume..... 78

Table 7: Thickness of all EGDSs used in this work. 85

Table 8: Determined electron mobility-trapping time constant product for EGDS 1-8. 109

Table 9: Determined hole mobility-trapping time constant product for EGDS 1-8. 109

Table 10: Determined relative efficiency of each EGDS in response to a Pu/Be source compared to the number of counts measured from a heavily moderated ^{3}He detector. 126

ABSTRACT

In this work a novel technique of multiplexing diamond is presented where electronic grade diamond plates are connected electrically in series and in parallel to increase the overall detection efficiency of diamond-based neutron detection systems. Theoretical results utilizing MCNPX indicate that further development in this simulation software is required to accurately predict the response of diamond to various interrogating neutron energies. However, the results were accurate enough to indicate that an equivalent diamond plate 1cm thick only lowers the energy resolution of the $^{12}C(n,\alpha_o)^{9}Be$ peak from a 14.1 MeV interrogating neutron reference field by a factor of two compared to a single diamond plate 0.5mm thick while increasing the detection efficiency from 1.34 percent for a single diamond plate to 25.4 percent for the 1cm thick diamond plate. Further, the number of secondary neutron interactions is minimal, approximately 5.3 percent, with a detection medium this size. It is also shown that photons can interfere with lower energy neutron signals when multiplexing is used, especially at lower impinging photon energies, although the full energy peak still does not dominantly present itself in the pulse height spectrum for multiplexed arrays approaching 1cm with respect to the interrogating neutron reference field vector.

Experimental results indicate that series multiplexing is not capable for use as a means of increasing the active detection volume of a diamond-based neutron spectrometer because of the interaction of diamond detection mediums in series with

each other and the input capacitor of a charge sensitive preamplifier, where severe signal degradation is seen due to the equal impedances of the single crystal diamond plates. However, parallel multiplexing is shown to have great promise, although there are limitations to this technique due to the large capacitance at the preamplifier input for a large parallel multiplexed array. Still, the latter multiplexing technique is shown here to be capable of producing the largest diamond detection medium in a single detector with spectroscopic capabilities reported to date.

1. INTRODUCTION

Throughout the twentieth century there have been many advances in radiation detection. There are several types of radiation and each has a preferred method of detection. These radiation types include electrons, positrons, protons, alpha particles, heavy ions, and neutrons. Almost all of these radiation types carry a charge and therefore their detection usually relies on the direct measurement on the created charge due to the interaction of these radiations with various detection media such as gases and semiconducting materials. However, the detection of neutrons has historically proven much more difficult because neutrons do not carry a charge. This means that measurement system concepts used for all the other listed radiation types are not directly applicable to the detection of neutrons. Neutron detection relies on the capture of a neutron or elastic scattering interactions with target nuclei and the observation of ions created by these reactions.

The accurate detection and determination of neutrons and their emitted energy is very important. This data is required for many fields of study and commercial processes, such as the advancement of nuclear reactors and determining core flux profiles, shielding designs for personal protection, probing of materials to determine crystal structures, detectors for oil logging, and the detection and monitoring of special nuclear materials. However, neutron detectors capable of accurate spectroscopy are generally large, require long measurement times, and utilize time of flight techniques. This is a major deficiency in the field of neutron detection and

requires attention. It is for this reason that the work contained within is dedicated to the pursuit of advancing the technology of neutron spectroscopy.

2. METHODS OF NEUTRON RADIATION DETECTION

Systems designed to detect neutrons usually rely on the detection of secondary particles created through neutron interactions with various materials. This includes the use of elastic scattering and nuclear interactions. These methods have proven satisfactory for pure neutron counting, however, much information can be lost in converting a neutron into a measurable quantity of interest, such as its precise energy. Systems that can provide precise neutron energy are usually cumbersome devices and require very long counting times and unfolding algorithms. In the following a brief discussion on various neutron detection systems will be given that outline the detection mechanisms and the general limitations of each.

2.1 Liquid Scintillation Counters

One of the more popular systems for neutron detection is the use of liquid scintillation counters. These detection systems rely on the neutron elastic scattering of hydrogen atoms contained within a scintillating material that creates light due to the proton (scattered hydrogen atom) interactions within the detection medium. This light is collected and converted into electrons via a photocathode and the signal is amplified through a photomultiplier tube (PMT). Energy information about the interacting neutron is obtained through measuring the total number of electrons, after amplification through the PMT, which is proportional to the number of photons striking the photocathode and consequently related to the incident neutron energy. However, gamma rays can easily interfere with neutron signals which requires discrimination

techniques and there is an inherent energy resolution of 15-25 percent due to the statistical nature of electron creation in the photocathode.[1]

To get past this inherent drawback the use of multiple liquid scintillating detectors have been used that rely on the use of time of flight (ToF) information for determining the neutron spectrum but these systems often have low timing resolution and require multiple detectors and complicated electronics. ToF can also be used for imaging of the neutron source and are called neutron cameras but require extensive post processing to obtain an image. Examples include an organic scintillator-based capture gated neutron spectroscopy system that has shown that discrimination between an Am/Be and a ^{252}Cf neutron sources is possible and is capable of detecting a single energy peak corresponding the impinging neutron energy through a combination of thermalization and neutron capture.[1, 2] This latter detection method, however, requires about 20μs per pulse and is not suited for strong fluxes or fast timing.

2.2 Neutron Capture

Another detection method relies on activation and subsequent detection of isotopes of interest either after irradiation or actively, where the activating particles are from a possible source of interest (e.g. ^{232}Th). Several isotopes are of interest for this type of neutron detection, including europium, gadolinium, indium, silver, and gold. Each of these elements have naturally occurring isotopes that absorb neutrons well, and using all of these elements simultaneously gives an indication of the history of the source, but it does not give any information to the energy spectrum of the neutron source and the information it does give is not done so in real time.[3]

Thermal neutron capture in ^{10}B, ^{6}Li, and ^{3}He are all widely used for neutron detection. Neutron capture from each of these nucleons have a high probability in the thermal region, but each generally follow the 1/v law for its neutron capture cross section.[4] [3] ^{3}He has the highest thermal neutron capture cross section of 5330 barns, followed by ^{10}B at 3840 barns, and finally ^{6}Li, at 940 barns.[1, 4] [3] ^{3}He and ^{10}B are both used in proportional counters, each giving relatively high efficiencies at thermal energies, both of which drop dramatically at increasing neutron energies. As an example, a typical ^{3}He detector has an intrinsic detection efficiency of around 77% at thermal energies to 2% from an impinging neutron energy of only 100 keV.[4] The same trend exists for ^{10}B, but because of the lower reaction cross section and the limited pressure allowed because of its polyatomic nature, the neutron detection efficiencies and energy resolution are lower, each being 5-15% and 5-30%, respectively. However, BF_3 tubes have a better gamma ray insensitivity against ^{3}He tubes in general, being on the order of 10R/hr, except if CO_2 is added to the ^{3}He gas mixture, but lowers the full energy peak and the timing resolution significantly thereby increasing the electronic dead time of the detection system.[4] [10] ^{10}B lined proportional counters have a lower efficiency and resolution than its BF_3 counterpart due to self shielding of the reaction products.[1] However, these counters have a weaker sensitivity to gamma rays, where neutron counts can still be discerned in gamma-ray fields as high as 1000 R/hr with only a 50% loss in neutron signals.[4] All of these chambers have a low resistance to radiation exposure where complete destruction of the usefulness of the tube can occur at fluencies as low as 10^{12} cm^{-2}.[5] This is caused by a buildup of electronegative products

and the lifetime of the counters can be increased through the use of a charcoal lining to absorb these contaminants.[1, 4] They also do not operate well at higher temperatures as both the output voltage amplitude and resolution decrease (for polyatomic gases and the amplitude increases for monatomic gases) as the temperature increases, becoming completely useless at temperatures of 100^{o}C.[1]

Lithium cannot be used in a gas filled chamber as no gaseous form exists. In comparison, there is no solid form of helium, so it cannot be included in liquid and organic scintillators. ^{10}B loaded scintillators, both in solid and liquid, have been used. A scintillator material such as B_2O_3/ZuS have proven useful for time of flight applications, but the useful thicknesses are only a few millimeters due to its opaqueness to its own light.[1] Lithium is only used in scintillating materials, except in the sandwich configuration, where a thin layer of lithium containing material is placed in-between two semiconductor diode detectors, which has proven useful for thermal neutron detection with low background through coincidence counting between the two diodes.[1] LiI(Eu) detectors are widely used for thermal neutron detection, but because of the nonlinear light output from the reaction products, where energy resolutions are as poor as 40%, they are not used for direct neutron spectroscopy.[1] Another disadvantage of scintillating materials is that the gamma ray sensitivity is much higher than in gas filled counters, where signals often overlap with those from neutrons and pulse height alone does not indicate the type of interacting particle, as is the case with organic scintillation detectors previously discussed.

Neutron spectroscopy can be done with lithium through the use of moderators of differing thicknesses or with a specific thickness where the count rate per unit flux or dose differs for various impinging neutron energies. The former requires an unfolding algorithm to determine the neutron energy profile and the energy resolution is usually not better than an order of magnitude. The latter are called fluxmeters and dosimeters, and are known in the commercial industry as REM balls.[1]

Fission chambers operate in the same manner as ^{10}B lined proportional counters and have the same problems. Here, however, the energy of the reaction products share about 160 MeV, and because of this these neutron detectors can operate in gamma fields as high as 10^7 R/hr.[4] This allows these devices to operate as spent reactor fuel monitors. However, the sensitivity is generally lower than that of a ^{10}B lined chamber, and so rather large fluxes are needed to get a good statistical response.[1, 4] In addition, the mass difference between a fissile material and a neutron is too large to allow for neutron spectroscopy.

For thermal neutron detection semiconducting materials can be combined with a conversion layer for detection. Materials such as ^{113}Cd, ^{10}B, and ^{6}Li can be used, and the resulting charged particles due to neutron interactions with the conversion layer are measured when they enter the semiconductor that the conversion material is on top of.[1, 4, 6] This method, however, can generally not be used effectively for spectroscopic neutron detection, especially at higher interrogating neutron energies, with these conversion isotopes but requires a hydrogenous layer, where the scattering of the hydrogen atoms is detected by the semiconducting material.[6] The detection efficiency

for various neutron energies has been evaluated at optimum thicknesses of the conversion layer (in the micrometer range), and the efficiency for neutrons at 10 MeV is not more than ten percent for a CH_2 conversion layer, with decreasing efficiency with decreasing neutron energy.[6] This shows that, even though a decent probability of detection can be realized, the energy imparted to the recoil atom varies significantly, and for good counting statistics many interactions must take place, such that an even distribution should be realized of voltage pulses produced by the recoil atoms. The end of this distribution in the pulse height spectrum is proportional to the incident neutron energy in the case of hydrogen scattering. Unfolding algorithms must be applied to the measured spectrum when the neutron source is polyenergetic

2.3 Super Heated Fluid

Another system of neutron detection is based upon super-heated fluid detectors, where the neutron interactions vaporize the suspended metastable droplets.[6] Spectroscopy and flux measurements are conducted through counting the number of tracks created visually or through acoustic detection. Neutron efficiencies are on the order of 3% with low gamma ray sensitivity.[1, 6, 7] Beam imaging has also been conducted with this type of system with resolutions on the order of a centimeter, but the system is sensitive to its surroundings and specific temperatures are required for operation, making this system not optimum for field use.[1]

2.4 Elastic Recoil

Systems based upon the detection of recoil nuclei have been realized and are readily available. These are based on using hydrogenous gases, as it is possible for the neutron to lose all of its energy in a single collision with hydrogen, or up to 64 percent in the case of helium. Detection systems based on this concept can be solid, liquid, or gaseous. Liquid based systems utilizing recoil for detection are scintillation-based, such as NE-213 organic scintillation devices, whose poor energy resolution has been previously discussed and whose light output is nonlinear with respect to energy. For gaseous systems, ion chambers or proportional counters are quite useful at obtaining neutron energies when the source of neutrons is monoenergetic, but unfolding the measured spectrum to obtain the true impinging neutron spectrum is possible for polyenergetic neutron fields. The recoil nuclei interact with the fill gas and the subsequent electrons are collected via a charged anode. ^{3}He can also be used in this manner, where the full energy peak is shifted by an amount equal to the impinging neutron energy. However, the reaction cross section is low at non-thermal neutron energies and the signals are often drowned out by the lower energy signals produced by slower neutrons. Hydrogen and helium have scattering cross sections around a barn from thermal to about 1 MeV. This means that a flat distribution is seen in the pulse height spectrum with a tail at the neutron energy in the case of hydrogen, and 64% in the case of ^{4}He. Proton recoil telescopes work to remove this rectangular response function thorough the detection of one scattering angle only and works only for collimated (or plane wave) beams of neutrons.[1] However, due to the fact that the

detecting medium is a gas the efficiency is very low and not suited for quick determinations or for unsteady particle flux systems. As such detection systems do not provide fast determination times with appropriate statistics.[1, 4, 5]

Another option is the use of semiconducting materials as the detection medium and charge transport medium simultaneously. This is already done for gamma ray detection systems such as high purity germanium (HPGe) detection systems, as well as detection systems for UV, x-ray, charged particle, and neutron detection. For neutron detection the reaction of neutrons with the semiconducting material along with the semiconductor operational properties (i.e. the electronic properties) dictates if, how, and the quality of neutron detection. The electronic properties of the semiconducting material are the most important in this detection regime. For instance, in most silicon-based detection systems the use of p-n junctions is used as an alternative to producing high quality (low impurity) silicon and the result of which has lead to many advances in the electronics industry. However, p-n junctions are very thin, on the order of microns, and any interactions taking place outside of this region is not measurable due to the charge transport properties dictated by Ambipolar transport.[8] HPGe detectors fit this description over silicon based detection systems.[1] However, neither silicon nor germanium have nuclear interactions that produce charged particles suitable for epithermal and fast neutrons typically seen in fission spectra. There have been recent reports on the use of boron carbide isotopically enhanced in ^{10}B as a thermal neutron detector through the use of the Seebeck effect through heating from neutron capture by ^{10}B and through charge collection driven by p-n junctions.[9-11] These detection

systems have found rather good thermal neutron detection efficiencies per unit path length, however, they are not currently suited for neutron spectroscopy.

Another option is in the elastic scattering of neutrons from the semiconducting material. This concept has not been investigated for any semiconducting material short of diamond and is similar to that used in organic scintillators and ion chambers. The equation for the amount of energy a neutron can transfer to a target nucleus is well known and can be found in many texts.[1, 6]

$$E_R = \frac{4M_n M_R E_n}{(M_R+M_n)^2} Cos^2(\theta) \quad (1)$$

Here E_R is the recoil nucleus energy and M_R is its mass, E_n is the impinging neutron energy, and θ is the scattering angle of the recoiling target in the lab frame. It is clear that in this equation the energy of the recoiling nucleus is proportional to the ratio of the neutron to scattering nucleus masses when the scattering nucleus mass is large compared to that of the neutron. Applying this to the aforementioned semiconductors it is found that the maximum energy that can be transferred to a ^{12}C, ^{28}Si, or ^{74}Ge atoms is 28.6, 13.4 and 5.3 percent of the impinging neutron energy, respectively. This simple data shows that the resultant voltage pulse height acquired due to neutron scattering from germanium is small and is low for silicon. In addition, the p-n junction requirement is still required for silicon giving a very low detection efficiency.

It is also important to note that heavy nucleons exhibit elastic scattering cross sections that are dependent on the angle of the recoiling nucleus and high energy scattering of neutrons off of any nuclei. The reason is that the higher order quantum number “L” values in the Legendre Polynomials representing the particle wave becomes

significant at larger masses for the quantum mechanical theory of differential scattering cross-sections.[12] This leads to a non-even distribution in the deposited energy due to fast neutron scattering and if significant moderation does not occur in the detection medium, then there will be characteristic fluctuations from an evenly distributed spectrum. For spectroscopic detection of neutrons, complete thermalization is the goal for acquisition of a single peak. However, the use of preferential energy depositions due to a unevenly distributed differential scattering cross section that would present itself in the spectrum could be used to determine the neutron energy by utilizing an unfolding algorithm, which would be specifically useful for polyenergetic neutron sources.

The neutron detection systems so far discussed is not an all-inclusive list but it does indicate the difficulties of neutron detection, specifically while maintaining spectroscopic information in various operational conditions. Diamond has been mentioned in passing in this section through utilizing it as a semiconducting material that detects neutrons within its bulk. Its relatively low-Z makes it very insensitive to gamma rays, a major issue in many spectroscopic neutron detection systems. In addition, the radiation hardness, electrical properties, and various neutron interactions producing various charged particles that can occur with carbon make it a suitable candidate for further investigation as a neutron detection system. However, there are currently limitations in diamond growth technologies such that the maximum crystal size that can be realized, which is suitable for neutron detection, is severely limited. This limits the overall detection efficiency that can be realized with diamond without technological advancements or innovative techniques. This indicates that a diamond-

based neutron detection system is currently not capable of competing with other, commercially available, spectroscopic neutron detectors in most applications. As such the remainder of this document is concerned with detailing the detection mechanisms of diamond for neutrons, the expected responses to various neutron energies, and innovative techniques to increase the active detection volume without the immediate requirement of advancing CVD diamond growth technologies.

3. BACKGROUND IN DIAMOND BASED NEUTRON DETECTION

Relatively speaking, diamond based detection systems that have demonstrated an excellent electronic capability is rather new. Before the millennium diamond based detection systems required high quality natural diamonds. This was because diamond growth proceeded in a manner to that which occurred in the earth, through high temperature and high pressure (HPHT) treatments of graphite. Although this produces diamond the crystalline quality and level of impurities is almost always inadequate for electronic purposes.[13] As such very little work had been conducted in utilizing diamond for neutron detection outside of a few very pure diamond crystals that indicated the potential of diamond for this application.[14, 15] The advent of chemical vapor deposited (CVD) diamond occurred around the same time as HPHT growth methods but did not lead to an advancement in crystalline quality until late in the twentieth century due to economic viability over other semiconducting materials.[16] When interest and significant effort in low pressure growth techniques of diamond was finally pursued it took only a couple decades before highly intrinsic single crystal diamonds were produced.[17] Since then there have been several reports on the use of diamond as a detection medium in various high energy physics experiments, all of which have indicated the potential of diamond based neutron and heavy ion detection systems. The results of all these investigations has lead to an increase in understanding of diamond based sensors and their results will be shown in the following sections as the relevant properties of diamond for neutron detection are presented.

3.1 Neutron and Heavy Ion Interactions

The interaction of heavy ions with diamond is the same as that of any other material. Simplistically, any charged particle traversing in matter will liberate electrons and create dislocations in the condensed matter thereby creating free electrons as well. In diamond, these electrons are moved from the valence band into the conduction band. It is these electrons that are used to detect the presence of radiation. In the case of neutrons reactions with the target nuclei must take place that create particles that can be detected, namely charged particles. For diamond the isotopic composition is the same as that of natural carbon, comprised of ^{12}C and ^{13}C with abundances of 98.9 percent and 1.1 percent, respectively. The various types of neutron interactions that can occur with these isotopes at fast neutron energies seen naturally and in low energy physics are given in Table 1. As can be seen there are many reactions that can take place. However, many of these reactions have high threshold energies that make their use for neutron detection impractical in most fission spectrum-based neutron sources. Others have cross sections that are too low for significant detection versus other reaction mechanisms.

The reactions that are most important for neutron energies between epithermal and 15 MeV are reaction numbers 2, 4-7, 8, 9, 14, and 15. Reaction numbers 1, 3, and 13 have low threshold energies but result in the release of gamma ray energy to release the excess energy, which is not efficiently detectable in diamond due to the low Z-value of diamond. Further discussion on high energy photon interactions with diamond will be discussed in section 3.2. Reaction channel number two is elastic scattering of neutrons

off of ^{12}C. As indicated in equation 1 the maximum amount of energy that can be lost by a neutron in this reaction mechanism is 28.4 percent of its impinging energy. Of course this reaction mechanism also exists for ^{13}C but has not been evaluated thoroughly enough to be included in the Evaluated Nuclear Data File (ENDF) database.[18] Reaction numbers 4-7 deal with the inelastic scattering of neutrons off of ^{12}C that impart enough energy to the nucleus that the emission of an alpha particle for de-excitation of the nucleus will occur. The product of this reaction is ^{8}Be which is highly unstable and will decay into two alpha particles with a half-life of approximately 70 attoseconds.[18] Therefore these reactions essentially result in the creation of three alpha particles that have a variable energy release for any neutrons above the threshold energy and will therefore create a continuum of energies in the pulse height spectrum.[15]

At a neutron energy of 6.2 MeV, neutron absorption can take place and causes the release of an alpha particle with the ^{9}Be nucleus in the lowest excited energy state.[15, 19] Following the same reaction channel, the reaction can leave ^{9}Be atom in the first exited state at an energy of 1.68 MeV, where the energy threshold of this reaction is 8.8 MeV.[15] Looking at the threshold energies listed in Table 1 it is clear that reaction channels 2, 8 and 15 are the best suited to detect and determine the presence of monoenergetic neutron reference fields. The reason for this is because reaction number 2 stands alone at lower neutron energies and the edge of the pulse height spectrum signifies 28.4 percent of the impinging neutron energy. Experimental verification of this was conducted by Zimbal *et al.* in 2010.[20] In this work it was shown that the pulse height spectrum followed the shape of the differential scattering cross section for elastic

scattering in the range of 2-2.82 MeV. For neutron energies above about 8 MeV reaction numbers 8 and 15 stand apart of the pulse height spectrum and their location signifies the neutron energy and has been seen in various works.[7, 20-23] However, other reactions will take place and manifest themselves in the observed pulse height spectrum at and above 8 MeV and must be accounted for, particularly reactions 4-7.

Table 1: Neutron interactions with natural carbon

Reaction number	Reaction	Q-Value (MeV)	Threshold Energy (MeV)
1	$^{12}C(n,\gamma)^{13}C$	4.946	0
2	$^{12}C(n,el)^{12}C$	0	0
3	$^{12}C(n,n')^{12}C^{*}$	-	4.450[2]
4	$^{12}C(n,n')^{12}C^{*}(3\alpha)$	-7.275	7.886
5	$^{12}C(n,n')^{12}C^{*}(3\alpha)$	-	9.64[2]
6	$^{12}C(n,n')^{12}C^{*}(3\alpha)$	-	10.8[2]
7	$^{12}C(n,n')^{12}C^{*}(3\alpha)$	-	11.8[2]
8	$^{12}C(n,\alpha_o)^{9}Be$	-5.701	6.181
9	$^{12}C(n,\alpha_1)^{9}Be^{*}$	-7.381	8.800
10	$^{12}C(n,p)^{12}B$	-12.59	13.64
11	$^{12}C(n,d)^{11}B$	-13.73	14.89
12	$^{12}C(n,np)^{11}B$	-15.96	17.30
13	$^{13}C(n,\gamma)^{14}C$	8.176	0
14	$^{13}C(n,el)^{13}C$	0	0
15	$^{13}C(n,\alpha)^{10}Be$	-3.835	4.132
16	$^{13}C(n,n\alpha)^{9}Be$	-10.65	11.47
17	$^{13}C(n,t)^{11}Be$	-12.42	13.39
18	$^{13}C(n,p)^{13}B$	-12.66	13.64
19	$^{13}C(n,d)^{12}B$	-15.31	16.50
20	$^{13}C(n,np)^{12}B$	-17.53	18.89

[1] All data unless otherwise specified was obtained from the National Nuclear Data Center maintained by Brookhaven National Laboratory.[18]

[2] Data reported obtained from Pillon *et al.* reported in 1995.[15]

3.2 Electron and Photon Interactions

The quantification of the affect of photons on diamond is of upmost importance when concerned with neutron detection. Many neutron detectors are sensitive to gamma rays and many neutron sources emit photons. Photons are detrimental because the differentiation between neutron and gamma ray signals can be difficult, especially at lower energies, such as with an NE-213 detector, and many detection systems are sensitive to high photon flux fields, both in signal generation and in radiation hardness. It is for this reason that an analysis of high energy photon interactions with diamond is presented here.

It has already been shown that diamond can operate near the neutron generation region in a Tokomak, but in no case was there quantification of the effect of photons on the differential pulse height spectrum. Indeed, all sensors modeled so far have used diamond films and plates with thicknesses generally no greater than 500μm and often are much thinner than this. This diamond detector thickness is advantageous as the electrons produced in photon interactions (i.e. photoelectric, Compton, and pair production electrons), have ranges comparable to or longer than the depth of the diamond detection medium in the thinnest dimension such that their detection is limited. Still, diamond has been utilized as a photon beam dose monitor, fast electron detector, and UV sensor for space applications.[23-28] Preliminary exposures in 2004 with single crystal diamond with a ^{109}Cd and ^{137}Cs sources were conducted, where a broad 22 keV peak and the 478 keV Compton edge was observed, respectively, with a 5x5x0.5mm high purity single crystal diamond plate.[23] Another group did high exposure

field gamma ray doses from ^{60}Co on a 0.53mm thick high purity single crystal diamond sensor and showed that the signal produced had a signal to noise ratio of ~10^5, with a response time of 0.5 seconds, and a current output of 30-50nA at an applied dose rate of about 2.5Gy/min.[26]

Polycrystalline CVD diamond has also been investigated as a UV sensor for photodiode and space applications and showed similar results.[24, 28] A more recent experiment tested the response of a single crystal diamond to varying wavelengths in the visible and UV spectrum and to soft x-rays. They showed that the diamond detector's sensitivity to x-rays created from an x-ray tube with operational settings of 35kV and 17mA with a diamond plate thickness of approximately 20µm was 0.45 nC/R, and that the diamond current output to visible and UV exposure was flat until the wavelength went below a value of 225nm, which corresponds to the band gap energy of diamond (5.47eV).[13, 29] This group is also the first to show the temporal response from a gamma ray pulse with a width of approximately 1.5ns and that the response speed was below this pulse width.

At higher photon energies, the gamma ray sensitivity is dominated by the three major reactions, being the photoelectric, Compton, and pair production. Each of these has their respective dominance range, and a full discussion on this can be found in the references.[1, 6] For lower energy photons, the main interaction is the photoelectric effect, where the entire energy of the photon is absorbed into the kinetic energy of the scattered electron minus the binding energy. For medium energies, the main interaction

of photons is Compton scattering, where the amount of energy that can be transferred to an electron is described by[1]

$$E_e = E_\gamma \left(1 - \frac{m_o c^2}{m_o c^2 + E_\gamma (1 - Cos(\theta))}\right), \quad 2$$

where $m_o c^2$ is the rest mass of an electron, E_e is the energy imparted to the electron, E_γ is the incident gamma ray energy, and θ is the scattering angle of the photon. For photon energies of several MeV pair production becomes a significant factor. In Figure 1, the gamma ray mass attenuation coefficient and mean free path of photons in diamond are displayed,[30] where it can be seen that the mean free path of a 100 keV gamma ray is about 1 centimeter. This means that roughly 63 percent of the impinging gamma rays at this energy will undergo a reaction at this distance into diamond. However, there is the probability of Compton scattering at this energy, and therefore complete energy deposition may not occur. Still, once a reaction occurs, the deposited energy is then dependent on the rate of energy loss of the created electrons in diamond. The Bethe-Bloch equation for fast electron stopping power is described by[1]

$$-\left(\frac{dE}{dx}\right)_c = \frac{2\pi e^4 NZ}{m_o v^2 (4\pi\varepsilon_o)^2}\left(Ln\left(\frac{m_o v^2 E_e}{2I^2(1-\beta^2)}\right) - ln(2)\left(2\sqrt{1-\beta^2} - 1 + \beta^2\right) + (1-\beta^2) + \frac{1}{8}\left(1 - \sqrt{1-\beta^2}\right)^2\right), \quad 3$$

where N is the number density of the material, Z is the absorber atomic number, β is the electron's fractional speed compared to the speed of light, I is the mean excitation energy, m_o is the electron mass, v is the electron velocity, ε_o is the permittivity of free space, and E_e is the electron energy. As known in classical electrodynamics, accelerated

charged particles radiate energy when accelerated, and is another source of energy loss. However, even for a 2 MeV electron in diamond, the ratio of the ionization versus radiative energy loss is less than two percent.[1] The overall effect of these photon interactions are represented by the mass attenuation coefficient of elemental carbon, displayed in Figure 1.[30]

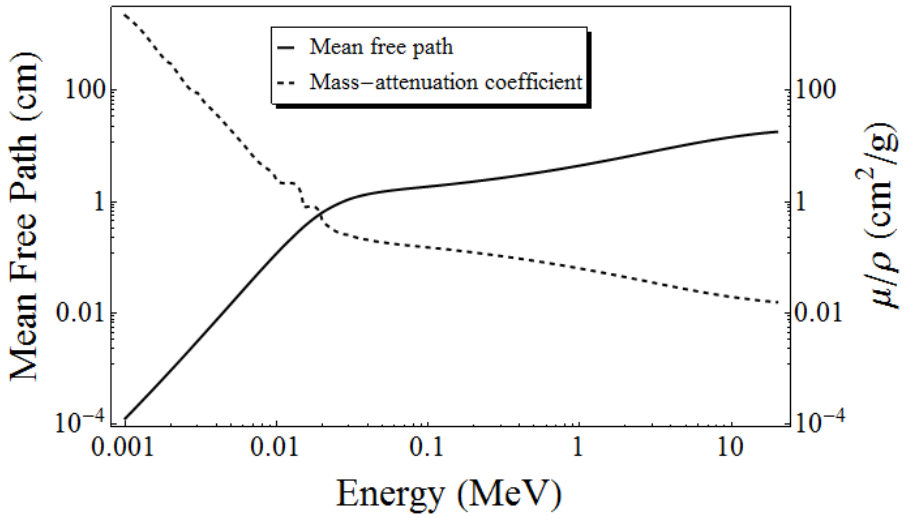

Figure 1: Mass attenuation and mean free path of gamma rays in diamond.

The electron ranges in amorphous carbon have been determined through the use of the ESTAR database.[31] With the electron range data, the following equation is used to determine the average number of electrons created per unit length.

$$N_o = E/(W \cdot R(E) \quad 4$$

Here, E is the electron energy, W is the average amount of energy required to create an ion pair in diamond, and R is the range of the electrons at the specified energy. Note that no data could be found for the W-value for fast electrons in diamond or carbon, where the W-value can differ by a small amount between differing ionizing charged

particles.[1] To this effect, the W-value has been assumed to be equal to 13.2eV, which is the value generally accepted for heavy charged particle interactions with diamond.[13, 32] Using equation 4 and the linear range of electrons,[31] the number of e-h pairs created per unit path length and the total number of ion pairs created for an infinite diamond medium from interacting electrons in carbon is given in Table 2. A graphical version of the range of electrons in diamond is given in Figure 2.

The largest thickness typically seen in commercial CVD diamond films is 500µm, where many radiation detection applications have used much thinner diamond films. The cross sectional dimensions are rarely larger than 5x5mm, but can be as large as a square centimeter for single crystal diamond plates. Since gamma rays interact volumetrically for such thin diamond films, the electrons are created volumetrically and the electron trajectory can be in any forward direction. Table 2 also indicates the number of charge carriers per unit path length, but can be deceiving as the units given imply many more charge carriers will be created than actually will, as the ranges are quite short for lower energies. In addition, the number of e^--h pairs in diamond created by carbon and electrons as defined by equation 4 is given in Figure 3. Here it can be seen that the number of e^--h pairs created from ionized carbon is often larger by more than an order of magnitude versus electrons. Taking into account the much shorter range of carbon atoms versus electrons, the pulse width and rise time should be much larger for electrons than for carbon atoms and pulse shape discrimination should be possible for very large crystals, an innovation yet to be accomplished.

Table 2: Electron interaction parameters with diamond.

Energy (MeV)	Range (mm)	N_o (#·10^3/mm)
0.01	0.0008	9.37
0.05	0.0138	2.74
0.09	0.0383	1.78
0.1	0.0458	166
0.5	0.569	0.666
0.9	1.24	0.549
1	1.42	0.534
1.25	1.86	0.509
1.5	2.30	0.494
1.75	2.75	0.483
2	3.19	0.475
2.5	4.07	0.466
3	4.93	0.461
3.5	5.79	0.458
4	6.64	0.457
4.5	7.47	0.456
5	8.30	0.456

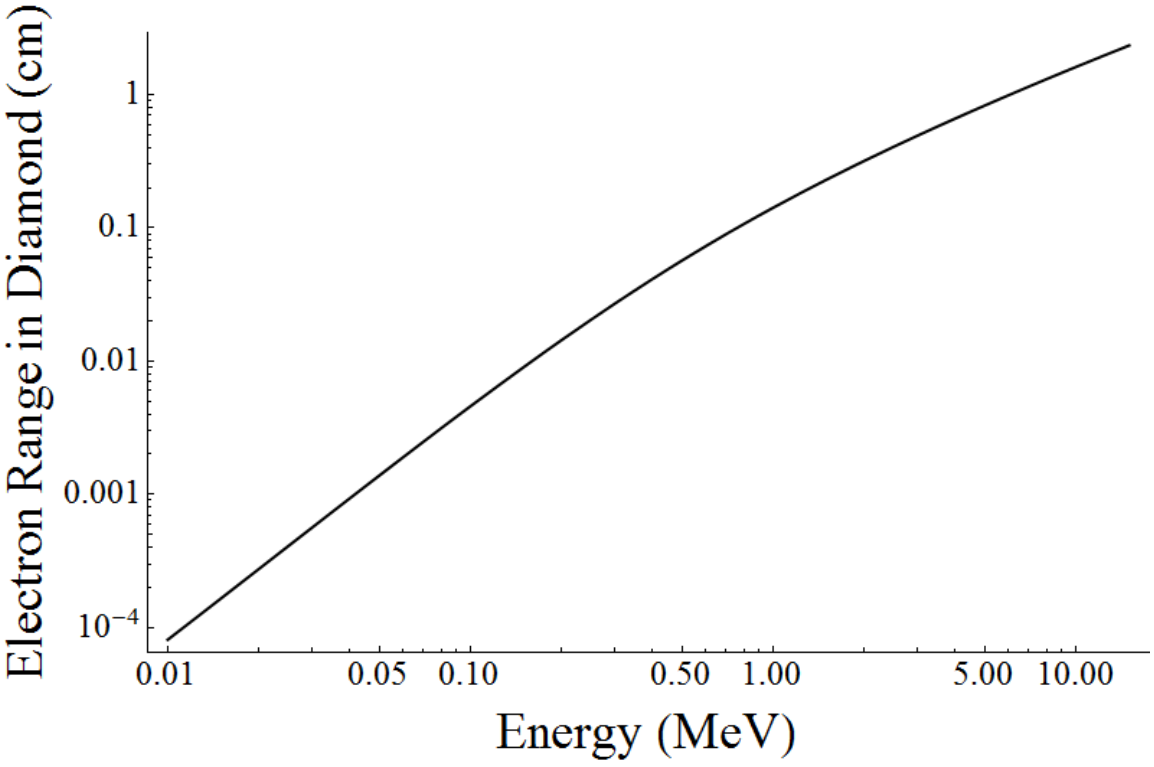

Figure 2: Electron ranges in diamond.

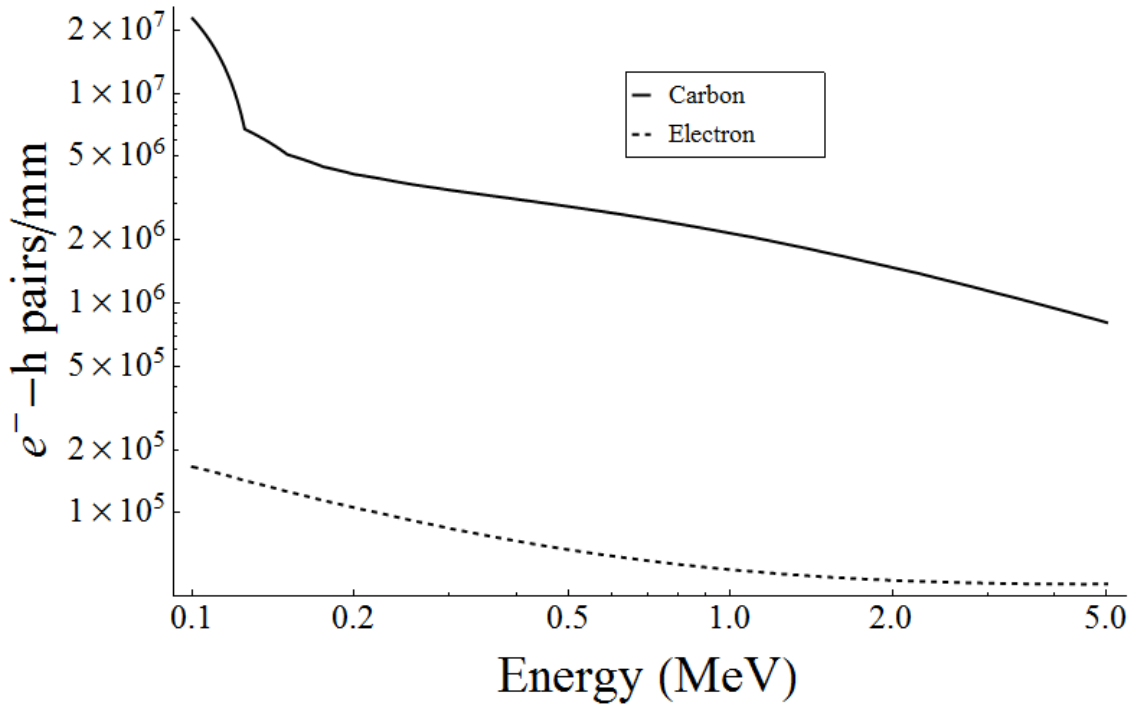

Figure 3: e^--h pair creation per unit path length for carbon ions and electrons in diamond.

As of yet there has been no experimental quantification between the gamma ray and neutron induced pulses in high flux fields of each when using a diamond detector. However, we know from Figure 2 and Table 2 that the range of electrons in carbon is roughly 0.6mm for a 100 keV electron and 1.4mm for a 1 MeV electron. This indicates that, since the electrons are assumed to be created volumetrically and follow a random walk-like path, a significant number of the electrons are expected to escape. A more in depth analysis is required to determine the actual ratio of distorted to non-distorted tracks of electrons in the diamond, but as the thickness of the diamond increases, the ratio will obviously decrease. This indicates that there should definitely be gamma ray counts in an exposure to a mixed neutron/photon field with perhaps a more broadened

photoelectric peak and increased Compton scattering level at lower energies. Schmid *et al*. in 2004 found that the Compton edge from a ^{137}Cs source was clearly present, but there was no discernable photoelectric peak.[23] Even with a ^{109}Cd 22 keV x-ray the photopeak was broad and the Compton minimum was quite high. Therefore, it seems safe to assume that any gamma ray at or above 661.6 keV will not produce a photopeak in the pulse height spectrum and that only a distribution of counts will be created in the region defined by the Compton continuum for diamond crystals of 0.5mm thickness or thinner. This claim will be further investigated in simulations presented in section 5.5.

3.3 Radiation Hardness

The radiation hardness of a detection medium is also an important characteristic. Radiation damage to semiconductors is mainly attributed to dislocations and other similar defect creations leading to bulk changes in the characteristics of the detection medium. For instance, radiation damage consisting of dislocations in a silicon lattice (interstitials) is often irreversible and leads to degradation of detector performance. The consequences of high neutron doses in silicon include an increase in leakage current, and change of the space charge in the depleted region, charge trapping, a compensating electric field due to changes in the effective doping concentration, and deep trap formation in the oxide layers on the silicon-silicon oxide interface.[6, 33] For instance, it has been shown that a fluence of only 10^{14} cm^{-2} for 1 MeV neutrons has increased the effective doping concentration significantly and other hadron bombardments at three orders of magnitude lower fluencies have produced significant leakage current in silicon based diodes.[33] These effects limit the use of silicon

as a detection system in high dose fields without often replacement or refurbishment due to degradation.

Diamond is quite interesting as many investigators have found the exact opposite effect for neutron irradiation versus silicon. It is true that the same damage types occur in diamond as they do in silicon, but the effect on the electronic properties differs greatly. First off, the sp3 bonded carbon atoms in diamond have shown to be much more resistant to radiation damage than most other materials due to its large displacement energy of 42eV.[22, 34-37] It has been estimated that a neutron scattering event will cause a primary knock-on carbon atom that will dislocate other carbon atoms. Calculations show that approximately 1850 carbon displacements will take place in one micrometer from a 1 MeV neutron scattering event and the total number of displacements increases to 27,100 for a 14.7 MeV neutron scattering event.[36] This is significant because it damages the diamond lattice and can affect the electron and hole transport through the creation of traps. However, it has been suggested that the traps created (vacancies) replace the previously present impurity sites and these new traps have a lower capture cross section and therefore, the electronic properties improve, meaning an increase in detector resolution and a decrease in the dark current. This has been seen in some investigations but not in others.[22, 35-38] In no case, however, did the transit times of the charge carriers decrease due to irradiation, indicating that, whether or not the created defects due to neutron exposure have a lower trapping cross section or not, they are neutral (no compensating electric field) and are often self annealing (self interstitial pairs).

This effect has been observed on single crystal diamonds from irradiation with 26 MeV protons and 20 MeV neutrons at a fluence of 10^{16} cm^{-2} for each and an electron dose of 7MGy as reported by the works of the authors of and discussed in the references,[37, 38] where the defects created by protons and neutrons exhibited the same characteristics on the electronic properties of the single crystal diamond detectors. It was also shown in these studies that after this large fluence exposure of protons and neutrons with their diamond detector reduced the charge collection efficiency (CCE) to fifteen percent and near full recovery of the CCE was obtained by annealing at 800^{o}C through migration of the realignment of the dislocated carbon atoms or by priming through ^{90}Sr electron fluence exposures of approximately 10^{14} cm^{-2}.

A 2.5MGy fluence of gamma ray dose from ^{60}Co showed only signal degradation from the cable, indicating CVD diamond is good for detection in high gamma fluxes.[39] It has also been shown that a 25 percent decrease in mean amplitude in alpha signal response results from a broad energy range (centered around 2 MeV) neutron irradiation of a fluence of $3*10^{15}$ n/cm^2 in high purity polycrystalline diamond, but the counting statistics remained about the same (i.e. same level above background noise).[39]

Another experiment of radiation hardness on polycrystalline diamond with 14 MeV neutron fluence of $8*10^{14}$ n/cm^2 14 MeV neutron fluence exposure to a polycrystalline diamond detection medium indicated that the charge collection distance (CCD) was reduced to about one half of its initial value and that annealing at 500^{o}C, re-metallization, and priming (radiation pumping) of the polycrystalline diamond detector

with long exposures to ^{90}Sr electrons after this lead to an increase of the CCD to 70 percent of its initial value.[36]

14.8 MeV neutron exposures to the LiDia detector configuration (see section 3.5) were conducted by M. Pillon *et al.* in 2008, where the detection properties were tested between exposures.[22] The total neutron fluence given was $2.03*10^{14}$ cm^{-2}. They saw that the energy resolution of the characteristic $^{12}C(n,\alpha_o)^9Be$ peak at 8.4 MeV improved after the first exposure, and subsequent exposures did not show any affect on the spectroscopic capabilities of diamond. They also calculated the dislocation per atom coefficient for their setup to be $8.42 \cdot 10^{-8}$, along with the ratio of transmuted atoms to original number of atoms, which turned out to be $1.08 \cdot 10^{-10}$. The DPA given is an order of magnitude lower than that reported by S. Almaviva *et al.* in 2009, where their exposure fluence was an order of magnitude higher in the fast neutron regime, but the interrogating neutron energies do not match and no thermal neutron absorption estimation by ^{12}C was taken into account, so no quantitative comparison is possible between these two results.[22, 35] Finally, the transmuted to original atom ratio quoted mainly consists of the already present ^{11}B with helium and hydrogen as well. However, transmutation requires large neutron energies, and the effect becomes much less pronounced as the interrogating neutron energy decreases.[22]

The LiDia detector,[40] which basically consists of an intrinsic layer of diamond grown on a p-type diamond substrate which itself was grown on a type Ib HPHT diamond and is coated with ^6LiF, was also tested at an experimental reactor facility and was exposed to neutron fluencies of $1.73*10^{16}$ cm^{-2} with a fast neutron fluence of

$3.4*10^{15}$ cm^{-2} (E_n>1 MeV). After irradiation, the diamond plates were investigated with catholuminesence (CL) experiments with an SEM. The end result was that the post irradiation showed a shift in the spectra to channels about three times lower and an approximate 50 percent CCE and 10.3 percent energy resolution versus a 100 percent CCE and 1.4 percent energy resolution before irradiation.[35] One of the most important results of this analysis was that they did not see a removal of the defect concentrations, and hence the electronic properties, through post irradiation in CL spectra after high temperature annealing at 850^{o}C for two hours and that the CL spectra obtained for the area under the part of the detector covered by the ^{6}LiF conversion layer showed additional damage. These additional features of the latter are similar to that of amorphous carbon and some removal of this feature was seen after the annealing step. The results of the affect of high fluencies on the electrical properties of single crystal diamond coincide with the work of A. Lohstroh *et al.* in 2010.[34]

The rate of vacancy formation, [V_o], was also estimated by through the equation

$$[V_o] = \rho_d * DPA \qquad 5$$

with the code SPECTER, where DPA is the dislocations per atom and ρ_d is the density of diamond.[35] They found that the dislocation rate from their source was $3.4 \cdot 10^{-6}$ and indicates an approximate vacancy concentration of $5.91 \cdot 10^{17}$ cm^{-3} and an equal amount of damage was estimated from the tritium and alpha particles released by the ^{6}LiF conversion layer.

Diamond resistance to heavy ion implantation has also been investigated for carbon and xenon at energies of 100 keV and 320 keV, respectively. The first observed

sign of a change in the bulk resistance of the diamond due to the conversion of sp3 insulating bonds to sp2 conducting bonds occurs at fluencies of greater than 10^{14} ions/cm^2 at room temperature.[13] At this point, called the critical dose, the resistance of the diamond bulk degrades substantially as the fluence value increases. It has also been shown that thermal annealing only returns the crystal to its diamond structure if the fluence is kept below the critical dose level, and annealing the sample after reaching the critical dose level results in significant bulk deformities, such as a buried conductive layer of sp2 bonded carbon or fine grain polycrystalline graphite.[13] These results seem to coincide with the CL spectral results discussed previously.[35]

The end result is that single crystal diamond is more radiation tolerant than polycrystalline diamond, where single crystal diamond can withstand up to 10^{14} n/cm^2 fluencies and still maintain its pristine operability, and at higher fluencies, can be treated to restore some of its detection capabilities. Since most irradiation experiments occurred at high neutron energies, which will create a statistically larger number of defects in the detector per interacting neutron, it can be inferred that higher fluences of lower energy neutrons in a diamond detector can be tolerated thereby maintaining its electrical properties, such as that seen in a fission spectrum. However, thermal capture can become significant if the total fluence is high enough to convert ^{12}C to radioactive ^{14}C in significant quantities.

3.4 Electrical Properties

The most prudent characteristic of diamond that needs to be addressed when concerned with radiation detection is its electrical properties. Of interest is the affect of

the diamond crystal type, doping and impurity affects, the electron and hole mobilities and drift velocities, the response time of the material to charge creating events, and the material's bulk resistance. These properties give an indication of the sensitivity and size that can be realized in a semiconductor detection system.

First off, to create an electron-hole pair, radiation must interact with the medium and create the ion pair, where it has been shown that the energy required is 13.2eV for high purity diamond plates.[13, 32] However, how the diamond transports the created electrons and holes is an important property, and the first thing to address in this respect is the type of diamond available for detection.

Two main types of CVD synthetic diamond are currently available, polycrystalline and single crystal. The difference between these two is that polycrystalline is composed of large single crystal grains, on the order of micrometers, while single crystal is as its name suggests. Polycrystalline, due to the grain boundaries, exhibits poor electronic properties and varying response curves due to the location of radiation interaction, whereas single crystal diamond does not have its electron and hole mobilities affected by any grain boundaries and sometimes does not exhibit polarization effects.[36, 39, 41] For single crystal diamond polarization has been seen in a few investigations, some developing over time and some more instantaneous, but simply turning on and off the voltage or applying a higher voltage has, in some cases, removed the effect.[34, 35] The polarization effect is suspected to be due to the buildup of space charge, which can occur when there are significant traps (defects) within the diamond material or at the diamond-metal contact interface. In addition, polycrystalline diamond has a typical

energy resolution of approximately 50 percent.[39] Polycrystalline diamond has also exhibited much larger dark currents over single crystal diamond and increasing the bias applied to the polycrystalline diamond film lowers its energy resolution but increases the energy resolution of single crystal diamond.[36, 38] These results along with the fact that polycrystalline has a much lower tolerance to radiation damage indicates that single crystal diamond is the best diamond detection medium for high fluence and spectroscopic applications.

The effect of doping and impurities is an important factor on the electronic properties of diamond. Doping is used in other semiconductors to create depletion layers through p-i-n junctions and because achieving purities in semiconducting materials capable of exhibiting intrinsic properties is hard to achieve. For diamond, however, doping has proven to be quite difficult for uniformity and of high concentrations while maintaining the crystal lattice structure.[13] The two main impurities that are included in diamond during the CVD growth process is nitrogen and boron, both in the parts per million or less for plates of any intrinsic electronic quality, where these levels are extremely important on diamond's ability to be used as a detection medium.[42] Boron provides an acceptor level in the band gap and nitrogen a donor level. The energy level of the boron in the band gap is 0.37eV above the valence band and the nitrogen energy level sits 1.7eV below the conduction band, where the band gap of diamond at room temperature is about 5.47eV.[32] The nitrogen energy level is far too deep to be utilized for the creation of an n-type diamond although it is common to make p-type diamond through significant boron doping.

Research has shown that nitrogen and boron impurities are the sources of trapping and de-trapping that limit the complete collection of generated charge from radiation interactions, where impurities in the parts per million range severely degrade spectroscopic capabilities, even for thin single crystal diamond plates.[39, 43] For diamond of decent type IIa quality with nitrogen impurity levels in the parts per million range, the passivation of these traps can be accomplished through pumping/priming the sample with high energy electrons or x-rays at significant doses, the same process that was discussed in recovering a diamond detector response after extreme radiation exposures as discussed in section 3.3. This is possible because of the deep energy level the nitrogen impurity creates in the band gap below the conduction band minimum such that the filled trap remains filled at standard temperature, although the boron energy level is too close to the valence band maximum where thermal excitation will create a p-type diamond if the boron concentration level is not kept very low.

Transport of electrons and holes in a semiconductor is described through the mobility and trapping time constant.[8, 44] The mobility indicates the ability of electrons and holes to move in response to an electric field applied across a given material and the trapping time constant is the mean time it takes for an electron or hole to become trapped in the material. The drift velocities for electrons and holes in diamond vary greatly depending on the quality of the diamond and in the crystal orientation, but are around 10^7 cm/s for single crystal diamond.[13] The drift velocities for polycrystalline diamond are much lower due to grain boundary affects. Advantageously, the drift velocities of diamond reach their maximum at relatively low applied fields, although not

a problem for higher required bias applications because of its high breakdown voltage of 10MV/cm.[32]

The mobility and trapping time constant can be calculated from the drift velocities determined experimentally through the use of a large bandwidth oscilloscope[41] or the product of the mobility and trapping time constant can be determined through measuring the CCE versus applied voltage utilizing Hecht's theory and a spectroscopic grade alpha source or a monochromatic photon source.[17, 23, 45] Mobilities for electrons and holes have been reported to be as high as 4500 $cm^2/V{\cdot}s$ and 3800 $cm^2/V{\cdot}s$, respectively, and was also estimated that the trapping time constant is on the order of microseconds from an experiment using a monochromatic photon source and the TOF technique.[17] This same author reported on a later date that the product of the mobility and trapping time constant was at best, for the diamonds investigated, $3300{\cdot}10^{-6}$ cm^2/V and $1400{\cdot}10^{-6}$ cm^2/V for electrons and holes, respectively.[45] These results indicate that the general order of magnitude values of the mobility and trapping time constants reported by this author in their previous work agree with their later results. However, many other experiments have shown much lower values for both the mobility and trapping time constant, such as that reported by M. Pomorski *et al.* in 2006 and G.J. Schmid *et al.* in 2004, where in the former the values reported vary by as much as twenty percent for the largest reported values of the mobility and trapping time constant.[23, 41] Both of these reports were based upon the use of commercially available electronic grade diamond from Element Six and used alpha sources for these measurements rather than a monochromatic photon source.[46] Still, the values obtained

showed that complete charge collection over a thickness of 500μm with moderately applied biases (<1V/μm) was achieved. In addition, it has been shown that commercially available single crystal CVD diamonds available from Element Six exhibited flat topped current pulses induced by alpha particle interactions and were measured by a large bandwidth oscilloscope, indicating that the width of these pulses were about two orders of magnitude smaller than the trapping time constant.[41, 46] Using these results as an indication on the capability of commercially available electronic grade single crystal CVD diamonds from Element Six lies on the assumption that these diamond plates are of consistent quality, a fact that will be tested in the experiments to be conducted.

The discussion on the mobility and trapping time constants as well as the recovery of the CCE due to radiation damage has been discussed but not been demonstrated for its importance. The CCE of a diamond detector is significant because if all the generated charge from a radiation interaction can be collected then spectroscopic information can be attained and the interacting radiation can possibly be identified. Most of the relevant data to the charge collection efficiency has already been discussed, mainly being in the fact that it relies on the mobility, μ, trapping time constant, τ, applied electric field, E, location of charge carrier creation, x, and detector thickness, W. Hecht's theory governs the charge collection efficiency, which is mathematically described in equation 6.[6]

$$Q_c = Q_o \left[\frac{\mu_e \tau_e E}{W} \left(1 - e^{-\frac{x}{\mu_e \tau_e E}} \right) + \frac{\mu_h \tau_h E}{W} \left(1 - e^{-\frac{W-x}{\mu_h \tau_h E}} \right) \right] \qquad 6$$

The charge collection efficiency is defined as the ratio of the collected charge, Q_c, to the generated charge through radiation interaction, Q_o. Equation 6 and variations

thereof are the equations used by the studies quoted earlier for determination of the mobility and trapping time constant of diamond for electrons and holes through photon and alpha exposure experiments, except for the TOF method. In these and other studies it was found that complete charge collection occurs for applied biases between 0.1-4 V/μm.[23, 26, 38]

In addition to the near one hundred percent CCE owing to the high mobility and trapping time constants of electronic grade single crystal CVD diamond there is also the fact that the timing resolution of this material is very appealing. In particular it has been shown that the pulse height rise time from radiation interactions is less than fifty picoseconds.[41] The pulse width is dependent on the crystal thickness and applied electric field but is generally in the nanosecond range.[41, 47] This indicates that diamond can both serve as a high count rate detector with minimal dead time and also for high resolution time of flight measurements utilizing the appropriate measurement electronics.

Even though the charge collection can be nearly one-hundred percent in a diamond detector there is still the intrinsic energy resolution. This natural energy broadening occurs because the creation of electrons from charged particle interactions is a statistical process and will not always create the same number of charges as the previous charged particle, even though they may have the same energy. Generally it is assumed that the creation of electrons from radiation interactions is a Poisson process, such that the energy resolution is limited by[1]

$$R = \frac{FWHM}{H_o} = \frac{2.35}{\sqrt{N}}, \quad (7)$$

where R is the energy resolution, H_o is the pulse amplitude and N is the mean number of electron-hole pairs created from the radiation interaction. The ionization energy, which takes into account the statistical process of electron-hole formation and therefore represents the mean value, for diamond is 13.2eV and for an ^{241}Am alpha particle of energy 5.486 MeV the total number of electrons created in diamond should be 415600 electrons.[13, 32] This indicates that the energy resolution lower limit should be 0.365 percent. Experiments have shown that the energy resolution of diamond detectors, that have not been corrected for other sources of noise, vary between 0.3-3 percent.[22, 23, 26, 35, 48] The lower value in the range quoted indicates that the energy resolution of the detection system used in one of these reports[22] may be below that predicted by Poisson statistics, a phenomenon seen in other semiconducting materials and is described through a fano factor,[1] although the number of significant figures quoted does not explicitly imply this result. In any case it is clear that the energy resolution of diamond-based radiation detectors is excellent and approaching that seen in silicon surface barrier detectors.

The resistance of the material is also an important quantity because it indicates the level of background current, or dark current, within the system, or indicates the charge collection sensitivity of the system. Germanium and silicon are both low band gap materials, yielding low bulk resistivity and consequently, high dark current values, which is not good for charge sensitive measurements (also due to impurities).[1] This also indicates, which is well known, that cooling of these two semiconducting materials is

vital during charge collection measurements as thermal excitation of electrons from the valence band and donor levels into the conduction band can occur at room temperature. High purity diamond, on the other hand, has very low dark current values, characteristic of its large band gap of 5.47eV, which indicates that diamond is both stable at room temperature and insensitive to visible light.[29, 32] The experimental dark currents reported in the literature depend on the thickness of the material and the contact metals used in electrode formation. The former defines the diamond's resistance through the intrinsic resistivity and the cross sectional area of the electrode and the latter also defines whether the contact is Schottky or Ohmic. Schottky contacts exhibit rectifying behavior whereas Ohmic contacts follows Ohm's law. Further discussion on this topic can be found in section 6.2.1, but it suffices to say that for the diamond plate thicknesses discussed so far the current pulled across a diamond plate is in the picoampere to nanoampere range,[26, 41, 47] indicating that diamond based sensors have a very low intrinsic noise.

3.5 Diamond-Based Radiation Detector History

All of the properties listed in section 3 were found through investigation of diamond based detection systems. There have been a multitude of investigations of diamond-based neutron and photon detection systems. Photon detection systems have been generally gauged at constructing UV sensors for various applications.[24, 26-28] Neutron detection utilizing diamond has had a much more colorful history in the past decade or so because of the need of good spectroscopic neutron detectors requiring little associated electronics and no multiple detector systems. This need is based upon

the fact that fusion experiments create a very large dose rate present in these facilities during operation. Diamond has been investigated for this task because small diamond crystals are practically insensitive to photons and electrons when their irradiation rate is much less than the time needed to remove the created electron-hole pairs, meaning that the system is not saturated to produce a continuous current output.

The main investigation of diamond-based neutron detection systems have been for new diagnostic sensors for ITER. There have been several investigations targeted at their development, such as the characterization of diamond timing capability,[38, 41, 47] energy resolution of alpha particle induced signals and comparison to silicon based alpha spectrometers,[21, 42, 48, 49] and characterization of their response to various mono- and polyenergetic neutron fields.[15, 19-21, 23, 29, 40, 48, 50] In addition, diamond has been explored in conjunction with thermal neutron conversion layers so that their sum may act as a real time thermal and fast neutron detection system.[40, 48, 49, 51-53] Finally, recent work has focused on the response of diamond to neutron fields for the finely characterized response over a large range of reference fields for the development of unfolding algorithms to determine the impinging neutron energy spectrum from the measured pulse height spectrum.[20, 21, 29, 50] These works give promise to diamond detection systems and there is still much work to be done, both in further characterization of detector response and determination of the detector stability over differing diamond crystals. Both of these are vital to the development and wide acceptance diamond-based detection systems.

4. SINGLE PLATE DIAMOND-BASED SPECTROSCOPIC NEUTRON DETECTOR SIMULATIONS

The preceding sections have outlined the basic properties of diamond as it pertains to radiation detection. The next task in developing a sensor system is to determine the response of a diamond detection system to various radiation particles. As was outlined in section 3.5 there have been several investigations in this respect. The most utilized application of diamond for neutron detection has been for the detection of neutrons from the tritium-deuterium fusion reactions. The measurements of this reaction is important because the international community is looking for radiation hard spectroscopic neutron detectors that has a good spectroscopic capability for the upcoming ITER.[7] This includes both the total fusion rate and diagnostic measurements of the core such as plasma temperature. There have been many experimental results pursuing diamond as a neutron detector for this application, as has been well established in preceding sections, but there is still much work to be done. Specifically, the change in the neutron energy due to plasma temperature in the fusion reaction can be relatively small and therefore requires that the precise response of the diamond detection system to various monoenergetic neutron energies be known. There have only been two theoretical papers published on the response of diamond to neutrons[19, 50] and a couple papers for experimental response outside of the pinnacle 14.1 MeV DT fusion and thermal neutrons utilizing conversion layers.[20, 21] As such the accurate modeling of a diamond detector response to various monoenergetic neutron sources is of upmost importance. In the following work will be presented at approaching a

simulation methodology to accurately simulate detector response to neutrons of varying energy. The determination of diamond to other radiation types, specifically photons, is also important because of the need to characterize its affect on diamond detection systems which could possibly interfere with neutron induced signals, especially as the detection volume increases.

4.1 Simulation Software

To theoretically estimate the expected pulse height spectrum coming from diamond-based neutron detectors a simulation software called Monte Carlo N-Particle eXtended (MCNPX) 2.7 was chosen for this work because this version of the program has been extended to allow for the transport of heavy ions down to 1 keV.[54] However, the neutron induced reaction libraries with carbon that produce charged particles in the ENDF/B-VII[55] libraries do not exist below 20 MeV. To overcome this limitation TENDL libraries,[56] MCNP-PoliMi,[57] and the ISABEL/Dresner physics models[58] were investigated for their validity based upon expected and theoretical results. The TENDL libraries contain the secondary charged particles from various neutron interactions that the ENDF/VII-B libraries do not for impinging neutron energies below 20 MeV. However, the format of the library files (ACE format) for both library sets are written such that the secondary particles are not correlated and as such energy is not conserved. A modification of MCNP 4C (a similar and preceding program to MCNPX) has been conducted to account for the format of the interaction libraries not correlating secondary particles produced in interactions to conserve energy and the resulting program is called MCNP-PoliMi. This program takes interactions and uses crude energy

conservation laws to determine the energy deposited in the system to model real detection systems. However, as this modification is a part of MCNP the secondary interactions that produce anything other than neutrons, photons, and electrons are not transported. Due to these facts there are limitations to this version of MCNP and this will be investigated. The third option is to use physics models as energy is conserved in all reactions that are simulated, which is absolutely required for any accurate simulation of detector response. It has been found that the ISABEL/Dresner physics models in MCNPX 2.7 produces results that are qualitatively accurate for impinging 14.1 MeV neutrons, as will be shown in section 5.3. However, these models do not necessarily predict all possible interactions, cross sections of those reactions, and angular distributions of secondary particles accurately. The results from these various base simulation techniques will be discussed in the following sections.

In all simulations it was assumed that all diamond plates were metalized with a Ti/Pt/Au pattern of 100nm/50nm/100nm thicknesses as this electrical contact pattern has found much use in the past and produces contacts that exhibit somewhat Ohmic behavior. [59-61] Further discussion on this contact scheme can be found in section 6.2.1. The diamond plate dimensions chosen in these simulations were equivalent to that available commercially, being 4.5x4.5x0.5mm^3 and natural abundances between ^{12}C and ^{13}C was assumed.

The radiation sources (neutron and photon) in all simulations were configured to apply a plane wave of particles equally across the broad face of all multiplexed diamond arrays. Every source particle simulated was configured to impinge on the diamond

detector and so the results of all simulations are normalized to the cross-sectional area of the detector, such that any results obtained are normalized to the intrinsic efficiency of the detection system. Radiation particle interactions and subsequent energy depositions were measured through an F8 detector tally with a pulse height light (PHL) modifier and 10 keV energy bins with energy binning ranges appropriate to the simulated source particle energy. The MCNPX source code was also modified to change the NTALMX (an acronym indicating the number of tallies that can be called in a given simulation) input from 100 to 1000 so that a sufficient number of tallies could be simulated for this work, although MCNP-PoliMi did not have this modification included in its source code because it is not required for the resulting simulation data as it is formatted. In all simulations peak broadening from the statistical nature of radiation interactions with matter was not taken into account above the base algorithms of the code to better illustrate the relative effect of sharp peak broadening as the active diamond detection volume increases due to a reduction of charge collection as the charge collection distance increases. To analyze this effect the location of radiation particle interaction and secondary charged particle trajectories must also be taken into account.

The effect of the interaction location of a neutron and trajectory of the secondary particles is harder to account for in an MCNPX simulation. The most ideal simulation would be to tally the location and time of creation of every electron resulting from any particle interaction and applying a transport equation to determine the fate of each. However, this is not practical. In contrast, simply measuring the energy deposited

in a diamond plate is not sufficient as the broadening due to the loss of charge from collection across various distances due to the location of creation is not taken into account. Of course in MCNP-Polimi this cannot be taken into account because charged particles other than electrons are not transported by the code. Further discussion on accounting for charge collection will be given in section 5 after preliminary results have been presented on the use of TENDL cross section libraries over physics models in MCNPX.

4.2 Initial Investigations on Simulation Methodology and Detector Response to Neutron Reference Fields

The most pertinent task in this work is to simulate monoenergetic neutron reference fields to test the validity of the methodology for the three different simulation techniques to compare each of them to each other and to experimental results. As such neutron reference fields in the range of 0.5-20.1 MeV were simulated using one of the simulation methodologies previously described. In the following sections the results from these analyses are presented.

4.3 Preliminary Simulations Comparing the Simulation Methodologies

As a preliminary investigation to the validity of the simulation methodology neutron reference fields of energies 2 MeV and 14 MeV were investigated. The first neutron energy range was conducted because Zimbal *et al.* in 2010 reported on the exposure of a diamond plate of similar dimensions to 2-2.82 MeV neutrons and provides

an opportunity of comparing these simulation results with experimental results.[20] In addition, as was indicated previously there have been many studies on diamond for use in fusion experiments due to the high radiation tolerance of diamond. As such the determination of the simulation methodologies to 14 MeV neutrons was also conducted since the expected pulse height spectrum from this interacting neutron energy has been experimentally verified on multiple occasions.

The pulse height spectra resulting from the simulations utilizing the three methodologies for 2 MeV and 14 MeV neutrons are given in Figure 4. In part a) the results from the ENDF/B-VII, TENDL, and physics models for the 2 MeV simulations are displayed. Note that the ENDF/B-VII libraries were previously denoted as not capable of creating secondary charged particles below 20 MeV. However, the physics control of neutrons in MCNPX allows for the creation of heavy ions with conserved energy in the reaction, however, this control does not apply to higher energy neutron interactions resulting in charged particle production. As such the ENDF/B-VII cross section library for heavy ion scattering can be investigated. The shape of the displayed pulse height spectra should follow the trend of the differential scattering cross section for each library/physics model used.

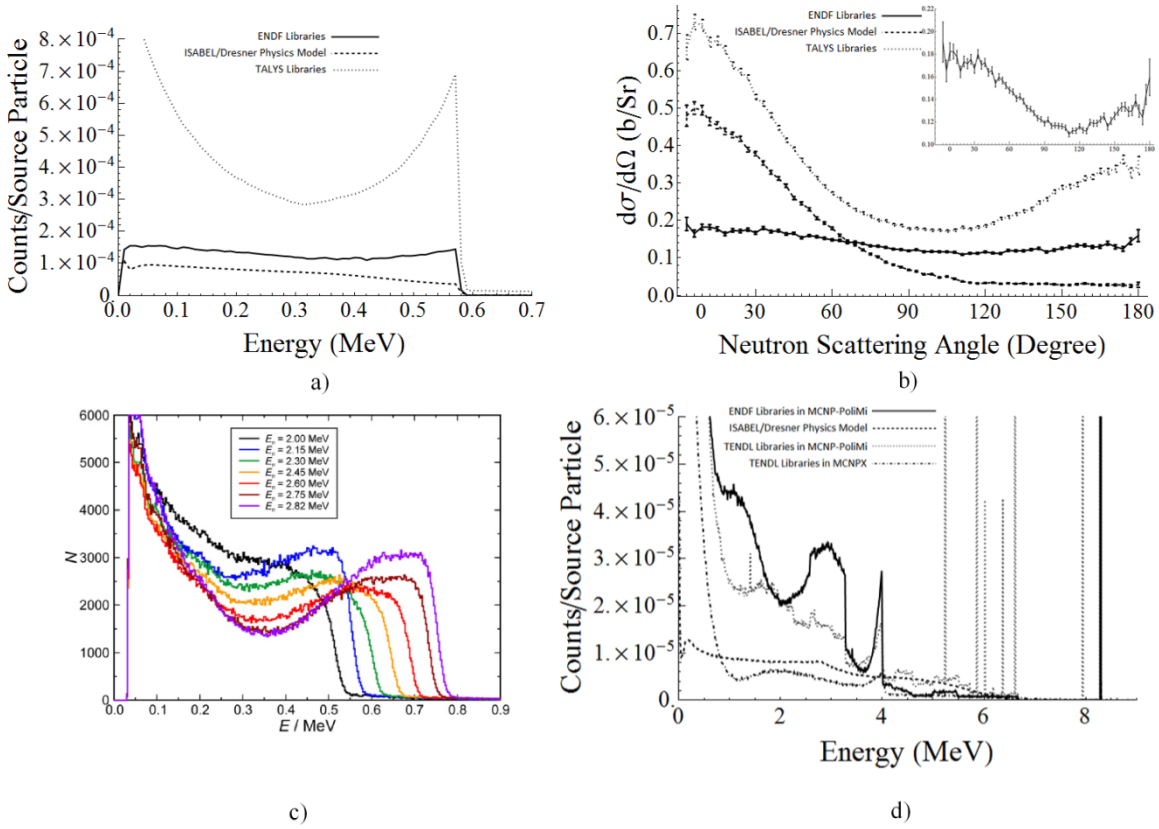

Figure 4: Monte Carlo simulation results on a single diamond plate for a) 2 MeV neutrons simulated with MCNP-PoliMi and the ENDF/B-VII and TENDL libraries and b) the differential scattering cross section calculated for these simulations. In part c) experimentally determined pulse height spectra for various monoenergetic neutron reference fields are shown from Zimbal *et al.* for the exposure of a similar diamond plate.[20] For further comparison of these simulation methodologies d) the simulation results from a 14.1 MeV monoenergetic neutron reference field.

To determine the differential scattering cross sections for the simulation methods utilized a spherical shell around a cube of diamond with one micron sides was simulated. The sphere was a shell and was broken up into sub shells defined through through a change in the inclination angle by three degrees with a 2π azimuthal angle. This created a total of 60 regions and the neutron surface flux traveling through each of these subregions of the spherical shell, N, was determined through MCNPX simulations.

These results were normalized to the total number of simulated particles N_o and then plugged into the equation that determines the intrinsic efficiency of a detection medium, given in equation 8.

$$\varepsilon = \frac{N}{N_o} = 1 - Exp[-n\sigma t] \qquad 8$$

Here n is the number density of the diamond, σ is the cross section for scattering, and t is the thickness of the detector with respect to the incident neutron vector. Solving for σ and dividing by the area of the subregion of the spherical shell the differential scattering cross section of the ENDF, TENDL, and ISABEL/Dresner physics models were determined and is displayed in Figure 4 b). It can be seen that the shape of the produced spectra shown in a) does indeed match the differential scattering cross section shape in all three cases. This has been shown to be the case in experimental results,[20] as seen in Figure 4 c). It can also be seen that the TENDL library has an overall interaction probability at 2 MeV greater than the ENDF library and by what is predicted in the ISABEL/Dresner physics models. In addition, it can be seen that the ISABEL/Dresner physics models predict that neutrons will preferentially scatter in the forward direction thereby depositing more energy in the lower energy region of the pulse height spectrum versus the higher energy end. This is a significant drawback to using the physics models in simulating a diamond detector response to neutrons typically seen in fission and fusion.

In Figure 4 d) the simulated response using MCNP-PoliMi with both the TENDL and ENDF libraries, the ISABEL/Dresner physics model, and the TENDL libraries in MCNPX 2.7 are shown from 14 MeV neutrons. The first curve that should be discussed is the TENDL library using MCNPX. It can be seen in Figure 4 d) that the resultant pulse

height spectrum determines the contribution from elastic scattering well but not any other reaction. The well studied $^{12}C(n,\alpha)^{9}Be$ peak at 8.3 MeV does not exist for this simulation output, although it is not apparent in the figure because of the various overlapping peaks at the same energy from the other three curves. The lack of information in the pulse height spectrum in this case is due to the fact that energy is not conserved in the sampling of secondary particles, as previously indicated. The ENDF and TENDL libraries in MCNP-PoliMi produce interesting results. The ENDF libraries do not accurately simulate the region above maximum energy deposition through elastic scattering from 14 MeV neutrons, which deposits a maximum energy of 3.98 MeV. The produced curve matches the differential scattering cross section very well for 14 MeV neutrons. There exist some other features above the maximum energy deposition for the elastic scattering interaction. Even though there are no secondary charged particles created in the ENDF/B-VII libraries for carbon below 20 MeV, some of the reactions still exist and this could be due to the breakup of carbon into three alpha particles. In addition, this could also be due to the crude way MCNP-PoliMi determines the energy imparted to a recoil nucleus from an inelastic scattering event.

The region above 4 MeV and below the $^{12}C(n,\alpha)^{9}Be$ 8.4 MeV peak is dominated by the breakup of ^{12}C into three alpha particles, a process that deposits a wide varying energy within the detection medium due to conservation of momentum concerns. The distribution in this range does exist in the pulse height spectrum but the overall height of the spectrum is rather low. In contrast the TENDL libraries in MCNP-PoliMi exhibit numerous peaks in this energy region. These peaks are attributed to the various

threshold energies of the breakup reaction along with the $^{12}C(n,\alpha)^{9}Be^{*}$ that leaves the ^{9}Be residual in the first excited state, which can be verified through inspecting Table 1 for the various neutron interactions that can take place and their threshold energies. However, there is also a distribution in this region of peaks due to the three alpha interaction with ^{12}C, and this results implies that the distribution in this region seen for the simulations utilizing the ENDF/B-VII libraries are probably due to the intrinsic error of MCNP-PoliMi for inelastic scattering events, although further investigation of this claim should be conducted.

These results imply that the TENDL libraries have a more accurate library, at least as is simulated in MCNP-PoliMi. However, the conservation of momentum of the secondary particles, which are not transported in MCNP-PoliMi, defines these sharp peaks rather than a broad energy distribution as is seen in experimental results. Finally, the ISABEL/Dresner physics model produces the closest shape compared to experimental results when the overall height from each region of the pulse height spectrum is taken into account. Nonetheless it is unclear which reactions are taking place and which ones are not in the higher neutron energy regime, such as the various ^{12}C breakup reactions. Still, the ISABEL/Dresner physics models seem to produce the best match to experimental results at higher neutron energies.

In addition, the results of the simulations utilizing the ISABEL/Dresner physics models also indicate that protons are created at an impinging neutron energy at or above 2.15 MeV, although there is no cross section known that should produce protons from natural carbon interactions with neutrons at such low energies. Through further

investigation it was found that the proton creation did not occur from neutron interactions with ^{12}C but with ^{13}C. Looking at Table 1 there are only two interactions that could produce protons, and each have very high energy thresholds and should not be possible at such a low interrogating neutron energy. Furthermore, the energy of the proton created is widely distributed and the overall creation probability for 2.82 MeV neutrons is approximately $1.5x10^{-7}$ per source neutron. With this in hand it is clear that this does not affect the overall measured pulse height spectrum but should be taken as an indication that, when using physics models rather than data tables, great care should be taken in analyzing the results.

From this analysis it is clear that there is no one simulation technique using developed codes, physics models, and cross section libraries that will accurately simulate the expected pulse height spectrum from a diamond detector over a large range of interacting neutron energies. However, the best match at higher energies seems to be the ISABEL/Dresner physics models. Even though these physics models do not accurately describe neutron interactions (i.e. absolute and differential cross section values) they are better suited for higher energy interactions. As such the ISABEL/Dresner physics models are best suited for simulations at higher neutron energies. It is for this reason along with the need to maintain consistency in the results that the ISABEL/Dresner physics models were utilized in the remainder of the neutron simulations.

4.4 Diamond Detector Exposure to Various Monoenergetic Neutrons Reference Fields

To further the investigation on the response of diamond-based neutron spectroscopic detectors a single diamond plate with properties previously defined were exposed in simulations utilizing the ISABEL/Dresner physic models to neutron reference fields between 0.5-10 MeV in steps of 0.5 MeV. Above 10 MeV energy steps of 2 MeV were made up to 18 MeV. Finally, 20.1 MeV neutrons were simulated. The reason for this final energy is because the ENDF/B-VII cross section libraries do not include neutron induced charge particle production data below 20 MeV and so 20.1 MeV was chosen to compare the physics models to tabular data to further the investigation on the affect of uncorrelated secondary particle sampling.

The results from the simulated exposures of the single diamond plate detection system are shown in Figure 5. The number of pulses per source particle in the spectra obtained here was multiplied by the impinging neutron energy to scale the results from all collected spectra. This was found adequate since the same number of source particles were simulated in all simulations and means that the number of interactions depositing energy at a given energy decreases as the neutron energy increases thereby lowering the overall pulse height spectrum. This effect is proportional to the impinging neutron energy and as such was used as the scaling factor. In part a) it can be seen that the energy deposited is relatively flat for 0.5 and 1 MeV neutrons and as the neutron energy increases the pulse height distribution begins to show an overall negative slope. This was already seen for 2 MeV neutrons in section 4.3 and is the expected result.

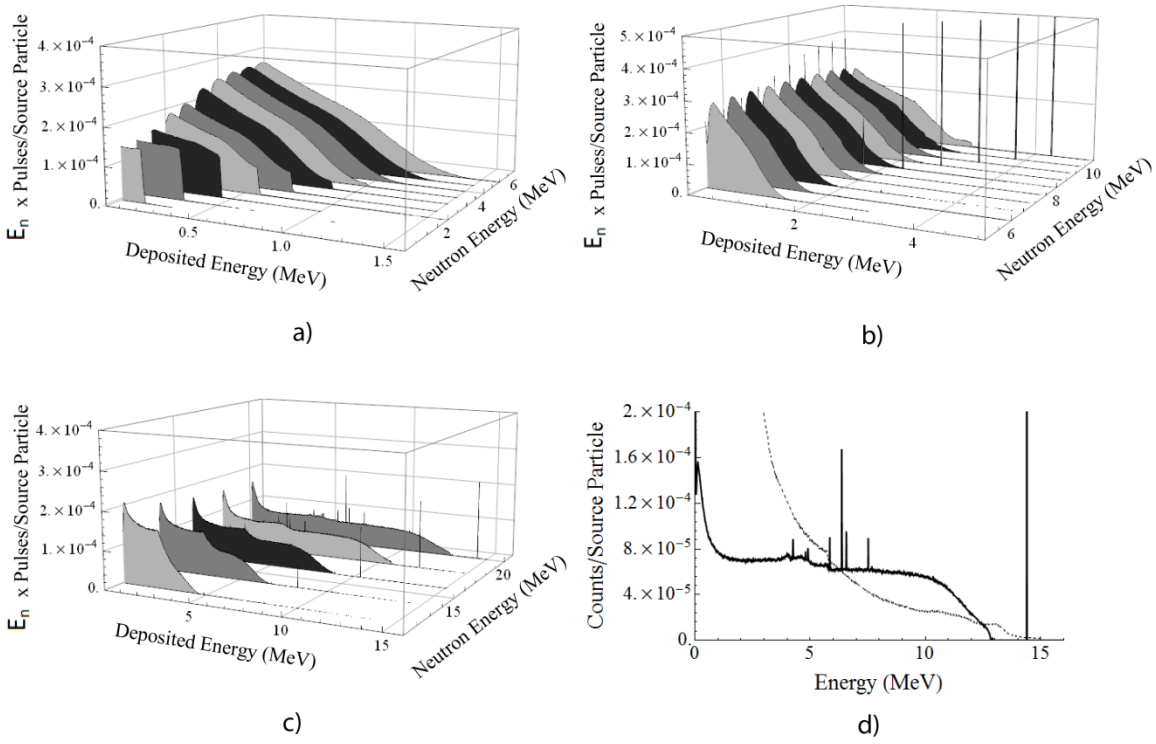

Figure 5: MCNPX 2.7 simulation results for a) 0.5-5 MeV, b) 5.5-10 MeV, and c) 12-20.1 MeV neutron reference fields. Part d) shows a comparison between the ISABEL/Dresner (solid line) and ENDF/B-VII libraries (dashed line).

As the neutron increases to higher energies other reactions start to take place as can be seen in Figure 5 b), which clearly shows the $^{12}C(n,\alpha)^{9}Be$ reaction, which has a threshold energy of 6.2 MeV, and can be seen clearly in all pulse height spectra as a peak above an impinging neutron energy of 7 MeV. Also, above about 8 MeV the $^{12}C(n,n')^{12}C^{*}(3\alpha)$ reaction starts to show in the bulk of the pulse height spectrum, thereby creating a very noticeable edge. As the neutron energy increases further many other reactions start to manifest themselves in the pulse height spectrum (see Figure 5 c) and d)). At 20 MeV elastic scattering can only deposit 5.68 MeV in energy but the bulk of the spectrum extends up to about 12.8 MeV, indicating that several other reactions

are attributing to the calculated pulse height spectrum. Looking at Figure 5 d) it can be seen that at an interrogating neutron energy of 20.1 MeV there are several peaks arising out of the continuum part of the pulse height spectrum. The energy at which these peaks reside in the pulse height spectrum are given in Table 3, where the peak number corresponds to the peak location from lower energy. Included in this table is the subtraction of the peak energy from the incident neutron energy to yield the reaction Q-value. This data was compared to Table 1 in section 3.1 and the reactions that took place to produce these peaks were predicted. It can be seen that only four of the seven peaks can be identified in the continuous region in the pulse height spectrum.

Table 3: Energy peaks from the 20.1 MeV neutron induced pulse height spectrum using ISABEL/Dresner physics models.

Peak Number	Energy (MeV)	Reaction Q-Value (MeV)	Predicted Reaction
1	4.259	15.841	$^{12}C(n,np)^{11}B$
2	4.799	15.301	$^{13}C(n,d)^{12}B$
3	4.900	15.200	-
4	5.849	14.251	-
5	6.369	13.731	$^{12}C(n,d)^{11}B$
6	6.569	13.531	-
7	7.519	12.581	$^{12}C(n,p)^{12}B$

There has been one experiment that conducted exposures to a diamond detection system to higher energy monoenergetic neutrons. Of interest is the results from the 20.54 MeV neutron reference field exposure conducted by Pillon *et al.* reported in 2011.[21] In this work two peaks were pointed out, namely peak numbers five and seven identified in this work. This leaves five other peaks not identified in the simulation results presented here. However, through careful comparison all of the peaks

identified in this work show up in the experimental results quoted, where the peak broadening and height over the continuum of the pulse height spectrum is such that strong visible peaks with good statistical certainty corresponding to the results presented here are not able to be quoted in that work. However, the features are evident and the origin of these features requires further analysis in future studies.

In addition, the quoted experiment also determined the cross section of the $^{12}C(n,\alpha)^{9}Be$ through determining the pulse height observed normalized to the geometrical efficiency and the neutron fluence.[21] To give the same analysis this peak was analyzed at each energy surveyed in this work. Note that these simulations are already normalized to the detector area and the fluence since all neutrons emitted enter the diamond and all results are normalized to the total number of source neutrons simulated. All that remains is to account for the thickness of the detector with respect to the incident neutron vector. This was accomplished through using equation 8 and solving for the cross section. The results of this analysis are shown in Figure 6. As can be seen the simulated cross section for the reaction greatly varies with respect to the accepted values quoted in the ENDF/B-VII database. This gives another clear indication that the neutron libraries for MCNPX and other Monte Carlo codes need to be modified to allow for a more accurate detector modeling capability or the codes themselves need to be modified to account for this limitation, such as MCNP-PoliMi attempts to do.

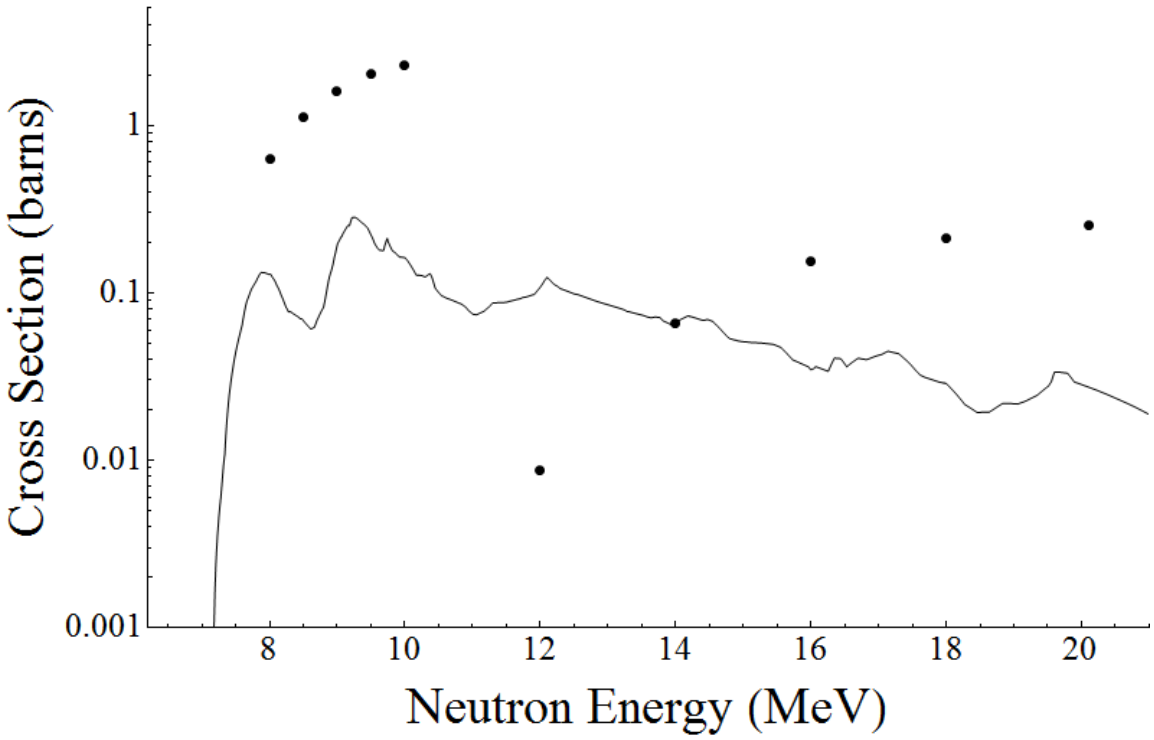

Figure 6: The neutron induced $^{12}C(n,\alpha)^{9}Be$ reaction cross section plotted against the results from the MCNPX 2.7 simulation results.

5. MULTIPLEXED DIAMOND ARRAYS FOR NEUTRON DETECTION

5.1 Diamond Deficiencies, Multiplexing, and Simulating Charge Collection Efficiency

One of the current primary deficiencies in diamond-based radiation detection is in the intrinsic and geometrical efficiencies that can be realized. The geometrical efficiency is governed by the cross sectional area of the detection medium that can be obtained as well as the geometry of the system. The intrinsic efficiency is limited for neutron detection and is based upon the mean free path of a neutron in diamond. For a typical neutron energy spectrum, such as ^{239}Pu, it has been shown that the intrinsic detection efficiency of diamond is a mere 4.1 percent per millimeter.[23] Since electronic grade diamond plates commercially available do not have thicknesses greater than one millimeter and cross sectional areas not greater than one square centimeter this indicates that the overall detection efficiency of a diamond-based neutron detection system is very low. This limits any diamond-based neutron detection system to applications utilizing large neutron fluxes or where the diamond can be placed very close to the neutron source. To get past this deficiency and make diamond-based neutron sensors more diverse a novel and evolutionary innovation of multiplexing is proposed. In multiplexing several diamond plates are utilized and connected to each other electrically, where signals arising from any given diamond plate is collected by the

same electronic acquisition system. In this fashion the neutron detection efficiency is increased without advancing growth technologies of diamond.

There are three ways to multiplex diamond. The first is connecting the diamond plates in series, such as resistors in series. The second way is connecting them in parallel similar to resistors in parallel. The third would be to connect the diamond plates in a configuration that utilizes both series and parallel multiplexing. There are face value advantages and disadvantages of the first two multiplexing techniques, which are similar to what is seen when done with resistors, being an increase or decrease in dark current. In addition, to obtain one-hundred percent charge collection efficiency the required bias would necessarily increase for series multiplexing, which could scale to unreasonable values if the multiplexing got too large. This is why a combination of the two is given as the third multiplexing technique as it should give a compromise between the two and optimize results. Two types of series and parallel multiplexing designs are shown in Figure 7. Also note that in the figure it can be seen that the contact area in the series multiplexing array has electrical contacts that come short of the diamond edge by 0.2mm. In the parallel multiplexing array configuration the electrical contacts cover the entire edge of all the diamonds and was chosen to be so because in a real experiment the ends of the diamonds would likely be capped with metal rather than just on the edge of the surface. These facts will have important consequences on the results as will be seen.

In the following sections the concept of multiplexing will be theoretically investigated for its affect on the pulse height spectrum induced by 14.1 MeV neutrons

and photons of various energies. The effect of multiplexing on the interaction of the current pulse traveling through multiple diamond plates in a series configuration or the effect of multiple capacitances in a parallel configuration on the preamplifier operating to supply a gain has yet to be discussed. This analysis resides within the experimental section of this work in chapter 6. However, simulations were conducted on various multiplexed arrays of diamond crystals to various radiation sources. Regardless of the outcome of the experimental results of the concept of multiplexing, the results in the following sections are valid in the sense that they represent the spectrum expected from larger diamond detection mediums, irrespective of whether this larger active detection volume comes from multiplexing or a larger continuous single crystal diamond.

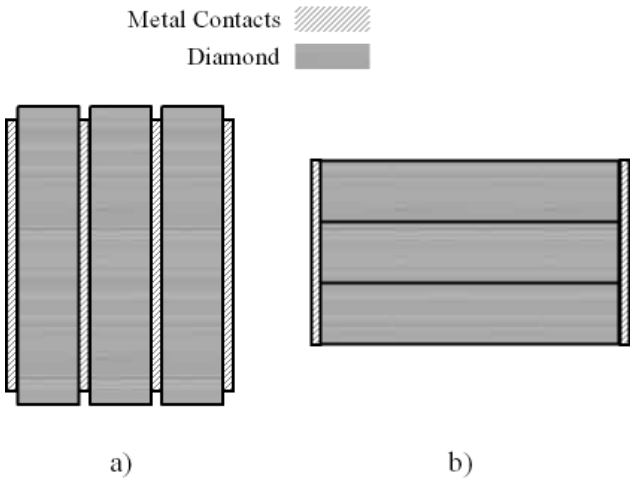

Figure 7: Pictorial representation of specific stacking types of a) series and b) parallel multiplexing configurations.

The characterization of charge collection on a single crystal diamond plate is a very important quantity to take into account. As an active diamond detection medium

increases in size through any means the distance that the created charged particles must travel increases. As pointed out in Section 4.1**,** the location of interaction and charge creation needs to be taken into account. MCNPX does not track electron creation location from secondary ions created from neutron interactions and in addition does not model electronic systems, meaning that crystal properties and concepts akin to condensed matter physics are not generally accounted for.

To deal with this difficulty each diamond plate was meshed into a series of cells. The first choice would be to make an infinite number of cells that would allow for CCE corrections to any location of charge creation. Unfortunately, this would completely disregard the trajectory of the secondary particles created because these secondary particles would travel through a very large number of bins, depositing little energy in each, resulting in an inaccurate pulse height spectrum. In addition, the smaller the mesh regions are the lower the interaction probability of radiation particles within that region; which could therefore lead to unreasonable simulation times to obtain good statistics. On the other extreme, making very large cells would neglect the location of charge creation and the application of Hecht's theory to the evolution of the pulse height spectrum.

To accommodate each of these limitations a medium between these two extremes was chosen where each diamond plate, in any multiplexing configuration, was spatially meshed into 50μm cells in thickness with respect to the direction of charge collection. This was found acceptable because the range of secondary particles in diamond from neutron interactions, mainly recoil carbon atoms, alpha particles, and

other heavy ions do not exceed 30µm for neutron energies typically seen from 14.1 MeV neutron interactions.[40] With these mesh region sizes simulations were conducted in multiplexed arrays where each diamond plate in the array was broken up into 50µm cells. Note that the interface between these regions has no significance in the transport of neutrons in the multiplexed detection array and the purpose is purely to determine the effect of charge collection on the energy resolution with multiplexing. The simulations produced pulse height spectra for each mesh region and these spectra were post processed to give the final results, which is clarified in the following section. Of course this indicates that if charge particles created during the simulation cross the cell boundaries this trajectory cannot be accounted for producing a single pulse residing in a single pulse height spectrum but the deposited energy will be spread among the two mesh regions. This is a limitation of the modeling technique and its effect will be seen and discussed in the results of this work, although it should be stated that it is shown that the effect is not significant enough to inhibit drawing valid conclusions about the effect of multiplexing with charge collection efficiency.

Finally, it should be noted that the incident plane wave entered all series multiplexed arrays at the charge collection electrode where the charge collection direction and incident particle vector were anti-parallel. For the parallel multiplexed arrays the charge collection direction and incident neutron vector were perpendicular. This geometrical description is further clarified in Figure 8 in section 5.2.

5.2 Post Processing For Multiplexed Array Simulations

After a simulation was run, post processing was required to extract the final pulse height spectrum for the various conditions modeled. The evolution of a pulse height spectrum due to radiation interactions within a detection medium at a specific location can be approximated through the use of Hecht's relation, given in equation 6. The data extracted from these simulations were exported into Mathematica 8.0[62] to apply equation 6 to each energy bin for each spatial region. The resulting data of each spatial region was approximated as a continuous function across the energy bins through an interpolation function and the interpolation function of each spatial region, after corrected for charge collection, was summed together for all regions of the detection system to produce the resulting pulse height spectrum. Interpolation was required because a series of bins, which is the output of the MCNPX simulations, is not easily manipulated through correction using equation 6 because each bin must be shifted to lower energies based upon its location in the diamond (i.e. mesh region) and the bin structure of each mesh region will be different than any other mesh region in the simulation resulting in data that cannot be summed together to produce a final pulse height spectrum. The effect of charge collection is best accounted for by creating a continuous function that can be multiplied by a constant rather than recreating the bin structure for each mesh region and then combining the resultant pulse height spectra that have dissimilar energy bin values and would therefore introduce a source of error. Note that this method assumes that no charge is lost due to charge transfer between the plates, charge transferred between the plates is injected into the conduction band

and traverses in the same manner as it did in the source diamond, and no polarization within the diamond occurs due to charge buildup within the bulk, meaning that the contacts are completely Ohmic and that no charge build up occurs at the metal-diamond interface. This analysis technique of the evolution of the pulse height spectrum with increasing diamond crystal thickness is pictorially described through Figure 8 and mathematically through equation 9, which is the summation of the product of equation 6 and the interpolation function, I, of each mesh region, j, over the total number of mesh regions N. Also note that the neutron source is impinging on the charge collection electrode in the series multiplexing configuration in the simulation and post processing methodology used in this analysis.

$$PHS = \sum_{j=1}^{N} I_j \left[\frac{\mu_e \tau_e E}{W} \left(1 - e^{-\frac{x_j}{\mu_e \tau_e E}} \right) + \frac{\mu_h \tau_h E}{W} \left(1 - e^{-\frac{W - x_j}{\mu_h \tau_h E}} \right) \right] \qquad 9$$

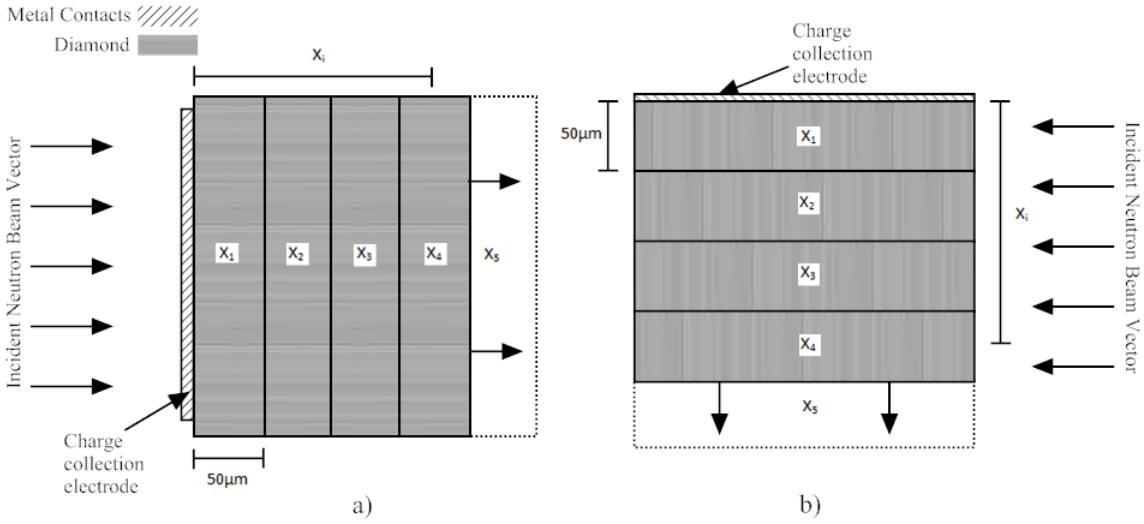

Figure 8: Representation of the mathematical analysis of the MCNPX pulse height tally output of an a) series multiplexed and b) parallel multiplexed diamond detectors through spatial binning.

It is important to note that in series stacking x_j will extend across all diamond plates and the summation total increases as the number of diamond plates simulated in the multiplexed array increases. However, in parallel stacking the number of meshes remains constant because the charge collection direction and the thickness increase direction in the diamond array are perpendicular and is therefore independent of stack size. This actually indicates that increasing stack size in a parallel configuration will not change the pulse height spectrum due to charge collection concerns but only due to secondary neutron interactions and mesh boundary effects whereas the series stacking technique will have its pulse height spectrum evolve due to both charge collection, mesh boundary effects, and secondary neutron interactions. It has been found that high purity single crystal CVD diamond can collect near 100 percent of the generated charge across 530μm with an applied electric field of 0.377V/μm.[26] It will be assumed in this work that this field is sufficient for charge collection and will be used in all calculations. Finally, the best reported value for the product of the mobility and trapping time constant in the literature is 3,300 cm^2/V and 1,400 cm^2/V for electrons and holes, respectively,[45] and for an upper limit on the estimate of what a diamond-based detection system can do this value will be used for all simulations that require charge collection efficiency corrections.

5.3 14.1 MeV Neutrons and Multiplexing

As indicated previously deuterium-tritium fusion neutron detection is one of the most important applications of diamond because of its high radiation tolerance. As a study of multiplexing early in its development it is important to simulate a

monoenergetic neutron source that has been well characterized with diamond detectors. As such 14.1 MeV neutrons were simulated with both series and parallel stacking. Specifically, stack sizes of one, three, five, eight, ten, fifteen, and twenty plates were simulated to estimate the effect of stacking on the charge collection and of multiple neutron interactions. In this section only the ISABEL/Dresner physics models were utilized.

A plot of equation 6 over these stacks sizes for series multiplexing is given in Figure 9 using the mobility and trapping time constants and electric field values indicated previously. It can be seen that the charge collection efficiency is highest when the radiation induced charge creation events is within the center of the multiplexed array. Toward the edges of the active detection volume, near the charge collection electrodes, the charge collection efficiency drops because of the loss of charge carriers that must travel a significant distance across diamond array for collection into the associated electronics. An interesting feature is seen in these figures in that at one electrode (the cathode) the charge collection efficiency is higher than at the other electrode (the anode). This is due to the mobility and trapping time constant products for electrons and holes not being equal to each other. In addition, it can be seen that for an array of 20 plates the charge collection efficiency is 91.1 percent at its lowest and about 98 percent near the center of the diamond detection array. The charge collection efficiency at the anode for all of these multiplexed arrays along with the parallel stacked arrays is given in Table 4. Note that for parallel multiplexing the charge collection efficiency and required bias remains the same because the size of the multiplexed array

is perpendicular to the charge collection distance. In addition, it can be seen that the bias required increases and the charge collection efficiency decreases for the series multiplexing technique as the array size increases. This gives an inherent limitation on the array size that can be utilized for detection before unreasonable biases or unacceptable charge collection efficiencies are reached.

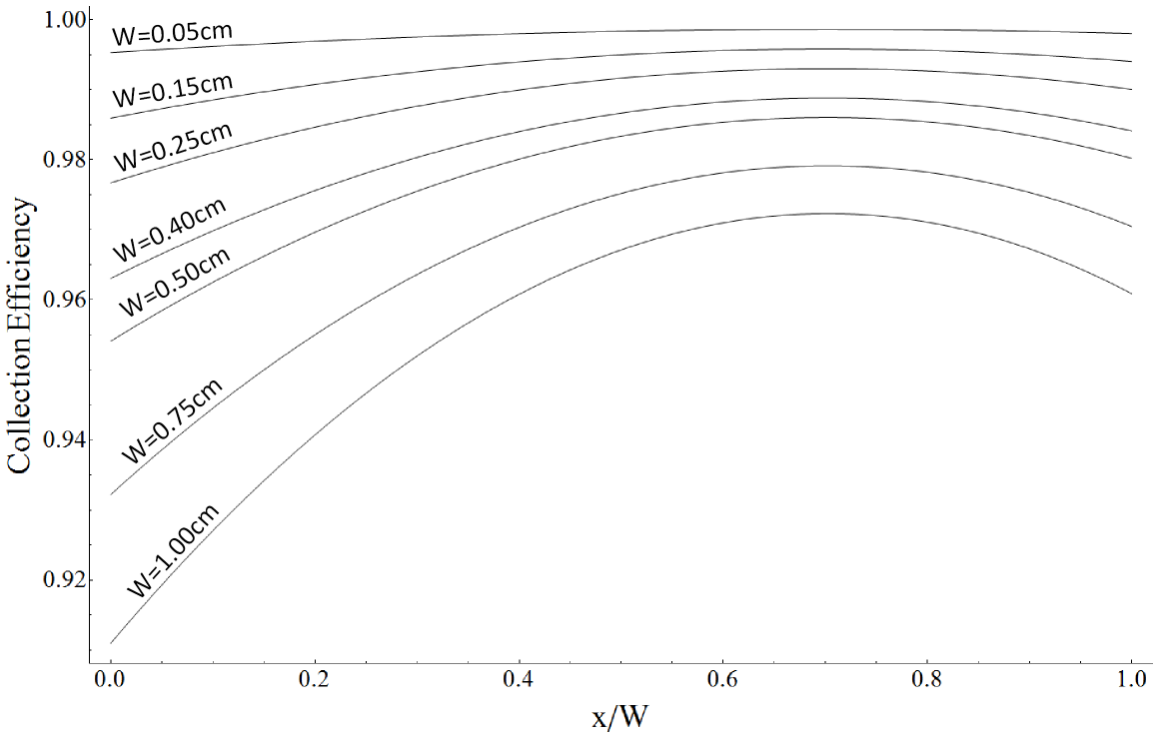

Figure 9: Plot of the charge collection efficiency versus normalized charge creation location across series multiplexed arrays of one, three, five, eight, ten, fifteen, and twenty plates in size.

Each stacking thickness was simulated both with and without meshing to characterize the effect of the change in the charge collection efficiency with increasing collection distance and the effect of meshing on the resultant pulse height spectra. For

the unmeshed arrays it was assumed that the CCE was equal to one. The simulation results are also analyzed to determine the number of secondary neutron interactions with the detection material. The latter is important because secondary interactions of neutrons with any detection material can blur the measured output spectrum, removing a significant amount of the energy resolution. The reason for this loss of energy resolution is that the secondary interactions do not take place for every neutron that enters the multiplexed diamond detection array. This means that counts will arise in the pulse height spectrum that do not correspond to any particular reaction but a sum of reactions. This effect can be taken into account in an unfolding algorithm to determine the true pulse height spectrum from the observed pulse height spectrum, but the process is simplified if secondary interactions are minimized.

Table 4: Basic electronic characteristics of multiplexing

Diamond Stack Thickness (mm)	Series		Parallel	
	CCE[a] (%)	Required Bias (V)	CCE[a] (%)	Required Bias (V)
0.5	99.5	189	95.9	1697
1.5	98.6	566	95.9	1697
2.5	97.7	943	95.9	1697
4.0	96.3	1508	95.9	1697
5.0	95.4	1885	95.9	1697
7.5	93.2	2828	95.9	1697
10	91.1	3770	95.9	1697

[a] The CCE values given are for charge collection when the charge is created at the cathode.

From the neutron reactions with natural carbon, as described in Table 1, it is can be inferred that the $^{12}C(n,\alpha_o),^{9}Be$ reaction deposits enough energy at a high enough probability that the deposited neutron energy can be separated from other neutron

interactions showing up in the pulse height spectrum. This peak is a great diagnostic tool for determining higher impinging neutron energies. As such the evolution of this peak with multiplexing was investigated along with secondary neutron interactions.

As one of the preliminary pieces of data, it is important to characterize the pulse height spectrum obtained from one diamond plate with and without meshing to illustrate the effect of the simulation method used. To give the most complete picture of the effect of meshing, both parallel and series multiplexing results are displayed in Figure 4. As can be seen in part a), the difference in the pulse height spectra between the series multiplexed meshed and unmeshed simulations is mainly in the lower energy part of the pulse height spectrum. This effect is due to the trajectory of secondary ions from neutron interactions with ^{12}C traveling across mesh boundaries, depositing energy in multiple mesh regions, which results in lower energy depositions in each spatial region they travel through. This is one reason why the meshed data produces a higher number of counts in a given energy bin per source particle at the lower end of the spectrum and a correspondingly lower number of pulses in the mid energy range of the pulse height spectrum. In addition, since a single secondary particle can create two lower energy pulses summing to the total initial energy of the particle if it traverses inside two mesh regions then the observed meshed pulse height spectrum for a given multiplexed detector array will produce more pulses than for an unmeshed array, as it is highly unlikely that a neutron will interact with a diamond region 50µm thick twice. This effect is also observed in the parallel multiplexing technique as displayed in Figure 4 b). Comparison between parallel and series multiplexing, or charge collection, techniques is

displayed in Figure 4 c) and indicates that parallel stacking produces more pulses overall than series stacking. This is because there is a larger active detection volume for the parallel versus the series multiplexing technique due to the way the charge collection electrodes were simulated.

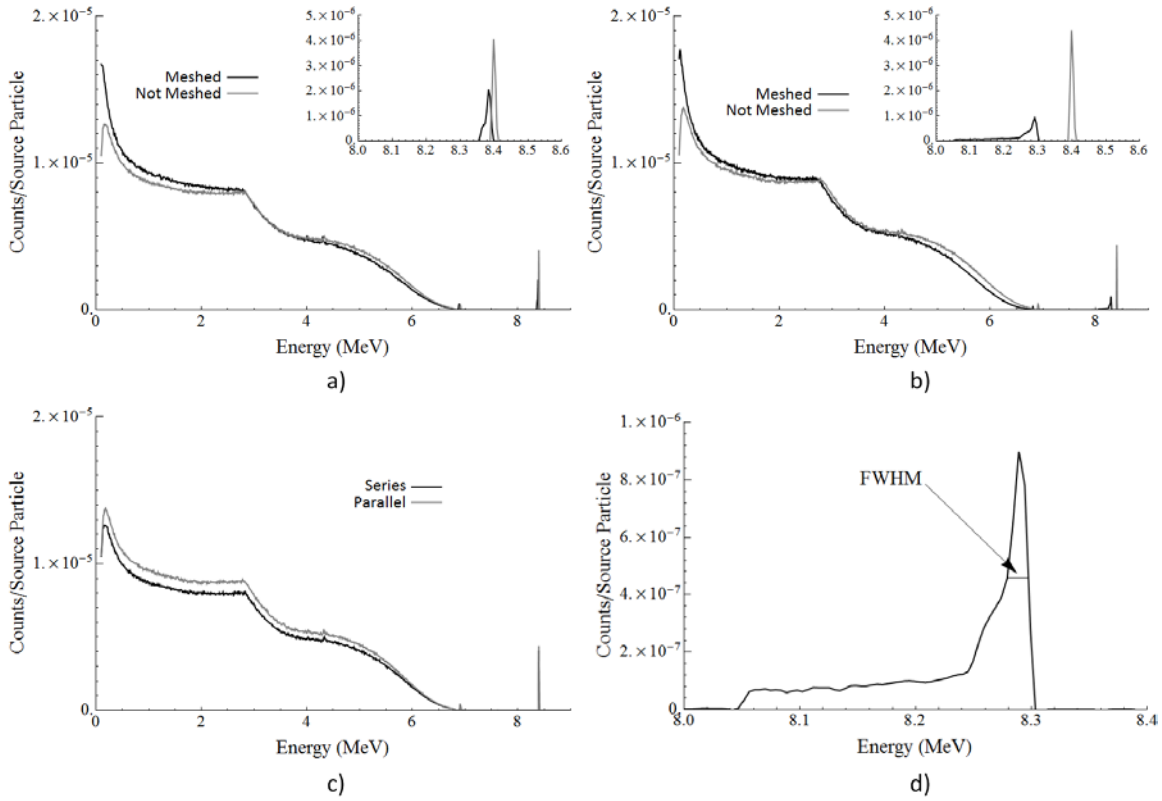

Figure 10: Simulation results showing the difference in the pulse height spectra of single diamond plates for a) series and b) parallel multiplexing from an impinging 14.1 MeV neutron reference field. The difference in the pulse height spectra of the series and parallel multiplexing techniques is shown in c) and the FWHM of the single diamond plate parallel multiplexing technique is shown in d).

The simulation results for parallel stacking in Figure 4 b) shows the effect of charge collection over a large distance as the 8.4 MeV peak from the $^{12}C(n,\alpha_o)^{9}Be$ reaction is significantly broadened versus an unmeshed simulation. Further, the series

stacking comparison between meshing and no meshing for this peak is minimal, where the peak seems to be shifting slightly to lower energies. It is important to note that there exists a strong peak at the highest energy in the pulse height spectrum corresponding to the $^{12}C(n,\alpha_o)^9Be$ reaction. The relative height of this peak versus the lower tail is due to the fact that charge collection efficiency is high and relatively constant through the diamond but tails off to lower collection values only when the location of charge creation approaches the electrodes. Since neutron interactions are a volumetric effect most of the resultant pulses reside in the peak seen in the displayed pulse height spectrum. A better view of this effect can be seen for parallel stacking, shown in Figure 4 d), where it can be seen that the dimension of charge collection is still small enough not to create a significant broadening of the main peak. However, it can be seen that the peak resides at an energy of 8.29 MeV, which is 0.11 MeV lower than where this peak resides without utilizing meshing. For a charge collection distance of 0.45cm the lowest charge collection efficiency is 95.9 percent and the maximum is 98.6 percent. The difference of the expected peak location (8.4 MeV) to the observed peak location is 0.986 and the same difference except with respect to the tail end of the pulse distribution in the pulse height spectrum is 0.958. These results indicate that the observed broadening is indeed due to a lack of complete charge collection.

Even though the minimum energy resolution, or energy bin, was set to 10 keV, it is important to quantify the full width at half maximum (FWHM) and the energy resolution between meshed and unmeshed data of the 8.4 MeV peak for these simulations. This information is given in Table 5. These results indicate that charge

collection over larger multiplexed arrays does cause measurable changes in the pulse height spectrum. Figure 9 d) shows a close up of the 8.4 MeV peak of the meshed one plate parallel multiplexed array to give a better view of the peak shape and FWHM.

Table 5: $^{12}C(n,\alpha_o)^9Be$ 8.4 MeV peak analysis for varying multiplexing configurations.

Array Size	Peak Properties	Series		Parallel	
		Meshing	No Meshing	Meshing	No Meshing
1	FWHM (keV)	13.6	10.0	18.2	10.0
	Resolution (%)	0.161	0.119	0.219	0.119
3	FWHM (keV)	15.9	10.0	18.1	10.0
	Resolution (%)	0.190	0.119	0.218	0.119
5	FWHM (keV)	18.7	10.0	18.1	10.0
	Resolution (%)	0.225	0.119	0.219	0.119
8	FWHM (keV)	17.9	10.0	18.1	10.0
	Resolution (%)	0.215	0.119	0.219	0.119
10	FWHM (keV)	17.6	10.0	18.0	10.0
	Resolution (%)	0.213	0.119	0.217	0.119
15	FWHM (keV)	17.8	10.0	18.0	10.0
	Resolution (%)	0.216	0.119	0.218	0.119
20	FWHM (keV)	17.5	10.0	18.0	10.0
	Resolution (%)	0.215	0.119	0.217	0.119

The other stacking sizes that were previously indicated show similar results with the chosen mobility-time trapping constant product and electric field. The results for three, five and eight plate and the ten, fifteen, and twenty plate multiplexing configurations for both the series and parallel stacking techniques are shown in Figures 11 and 12, respectively. Looking at these figures it can be seen that the FWHM of the generated peak for the parallel stacking configuration stays the same in all cases. The energy resolution, or the FWHM, increases as the stack size increases in the series multiplexing configuration as is expected based on Hecht's Theory.

Another interesting feature is the data given in Table 5 for the FWHM of the $^{12}C(n,\alpha_o)^9Be$ peak as the multiplexed array gets larger. It can be seen that the resolution worsens quickly as the stack size increases from a stack size of one to a stack size of five but then the resolution gets better and maintains a relatively constant value as the stack size increases further. The reason is that the charge collection correction broadens the observed peak more for larger stack sizes at the lower end but only lowers the peak height in the region where the maximum value resides. This is due to the fact that the main peak location is defined through the broad peak-like region in the charge collection efficiency curves shown in Figure 9 and indicates that a well defined peak will still manifest itself in the pulse height spectrum. This indicates that the energy resolution remains rather good for such a large multiplexed array, about 0.22 percent, and that the peak remains about a factor of five above its long distribution at lower energies. However, it is suspected that this peak will broaden and lower as the stack size increases until the peak starts to become statistically undistinguishable from the broad distribution created from the charge collection corrections thereby drastically decreasing the energy resolution of the detection system, although this work does not indicate at what crystal thickness this will occur.

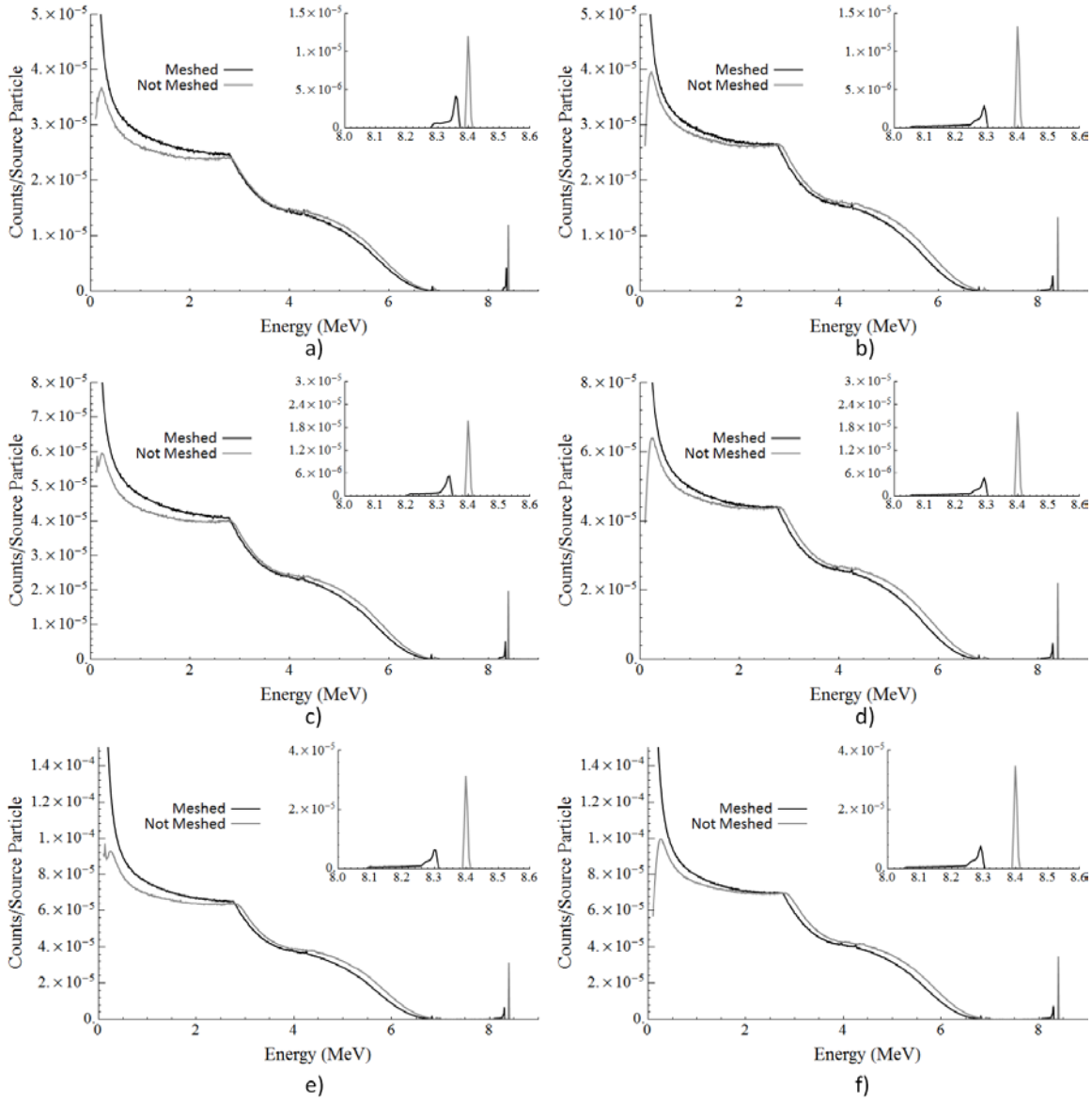

Figure 11: Pulse height spectra for the series (left) and parallel (right) multiplexing technique for three (a-b), five (c-d), and eight (e-f) plate array thicknesses.

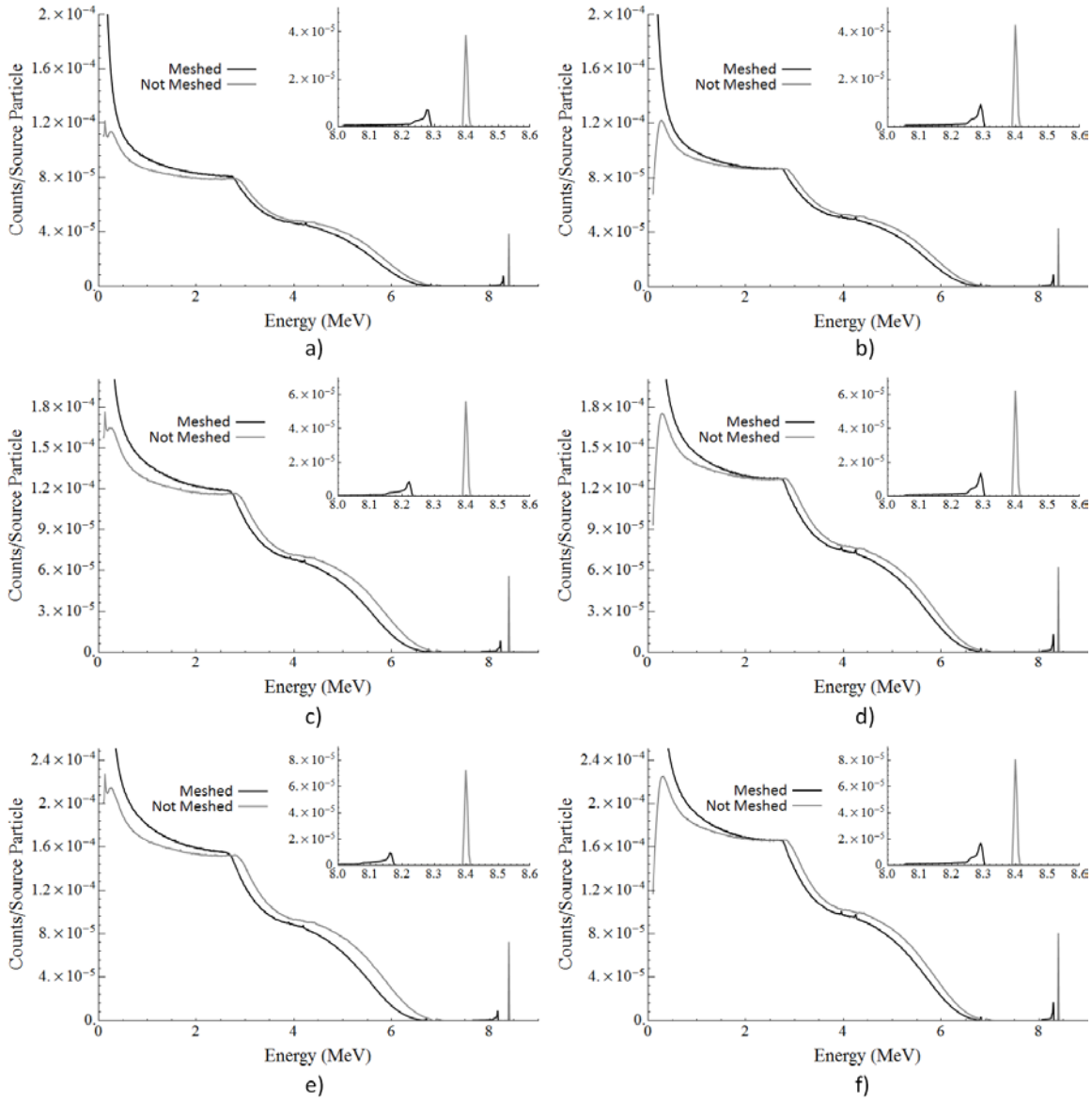

Figure 12: Pulse height spectra for the series (left) and parallel (right) multiplexing technique for ten (a-b), fifteen (c-d), and twenty (e-f) plate array thicknesses.

It can also be seen that for larger crystal arrays the pulse height spectra between meshed and unmeshed simulations start to separate. The main reason of this observed effect is that each mesh region is corrected by a different amount and the farther from the charge collection electrode the mesh region is the more corrected the spectrum is.

Hence, for large stack sizes the spectrum is distorted and shifted to lower energies and the disparity of the shifting of each mesh region with respect to the charge collection electrode is the cause for the removal of some of the spectral features seen. It is important to realize that the cause in the change in the sharp $^{12}C(n,\alpha_o)^9Be$ peak to its broadened state due to charge collection will also affect all channels in the pulse height spectrum. This is one reason for the slight broadening of the sharp edge that is seen at 2.8 MeV in the larger stack sizes versus smaller stack sizes. However, through analyzing the results it is apparent that this 2.8 MeV edge also broadens for unmeshed simulations, where the only difference between the spectra of unmeshed results is in the stack size of the multiplexed array. This implies that, as the detection medium increases, more secondary particles traverse through more than one mesh region, which is seen in the parallel multiplexed simulations where charge collection is independent of stack size. Further, the separation between meshed and unmeshed simulation results in the parallel multiplexing simulations increases as the stack size increases and is purely due to the mesh boundary effects with secondary particle trajectories. This indicates that the distortion of the spectral shape is due to charge collection and the “pure” shifting of the undistorted spectrum to lower energies is due to the technique used to simulate charge collection efficiency across multiplexed arrays. Secondary neutron interactions could also be playing a role as well, which could also cause a blurring of the edge in the pulse height spectrum around 2.8 MeV. Obviously there is more than one cause for the evolution of the observed pulse height spectra as the multiplexed arrays get larger in size.

It is also important to note that the neutron field strength entering every mesh region for the series multiplexed arrays is lower than the field strength entering the preceding mesh region, thereby lowering the observed pulse height spectrum in that region. This property yields pulse height spectra results between two mesh regions separated far apart similar to the spectra seen in Figure 10 c). The change in the neutron field strength was determined for the 200^{th} mesh region and the 1^{st} mesh region for the twenty plate series multiplexed array by comparing the height of the $^{12}C(n,\alpha_o)^9Be$ peak of each and taking the ratio of the former to the latter and was found that this reaction occurred 1.27 ± 0.07 times more often in the first mesh region than the last mesh region. Holding all other variables constant this indicates that the neutron field interacting with the 200^{th} mesh region is about 79 ± 4 percent of the impinging neutron source field strength on the entire array.

The modeling technique used here collected the charge at the face of the first mesh zone and for the series multiplexed arrays on the face closest to the entering neutron field. Therefore, the more significant the CCE correction factor on a mesh region the lower the weight that this region has on the resultant pulse height spectrum as determined from equation 9. This indicates that the pulse height spectrum should be further corrected through charge collection efficiency concerns if the charge collection electrode were opposite to the location of the entrance of the neutron plane wave into the series multiplexed array. For the parallel multiplexing technique the mesh direction and incident neutron field vector are perpendicular and therefore this effect goes unobserved.

Another important point that was brought up earlier is the limitation of stack sizes for series and parallel configurations. For series configurations the applied voltage across the array must be increased significantly as the stack size increases, such that a stack of twenty diamond plates would require an applied field of 3.9kV, which would introduce its own problems for any portable system. Parallel stacking, on the other hand, only requires a set voltage application for any number of plates included in the multiplexing array. However, the leakage current of the detection system also goes up in this configuration and the energy resolution is lower for any stack size versus a series configuration until the charge collection distances are equal between the two multiplexing configurations; although parallel multiplexing could be used in different configurations to remove this inherent drawback of the simulated parallel multiplexing configuration. In addition, the quantification of the leakage current for the parallel stacking configuration is of importance. It has been shown that the leakage current across an electronic grade single crystal CVD diamond plate 530µm thick is less than 2pA for various contact types at an applied voltage of 1,000V.[26] Therefore, even for a stack size of twenty plates the total leakage current at operational voltages could be as low as 40pA and therefore well below any external thermal noise introduced by any associated detection electronics.

To further the discussion on the effect of multiple energy depositions in the diamond detection medium from a single neutron, as was qualitatively discussed previously in the evolution of unmeshed multiplexed array results, further evaluation was conducted. Transport theory states that the probability of a neutron interacting

with any medium has an exponential behavior associated with the neutron's path length within the material and the macroscopic cross section of the material. A mathematical description can be found in equations 8 and 10, where ε is the intrinsic efficiency of neutron interaction, Σ_t is the total macroscopic cross section of diamond for the relevant neutron interactions as it pertains to detection, and x is the neutron path length [1].

$$\varepsilon = 1 - e^{-\Sigma_t x} \qquad 10$$

It has been found in this work that Σ_t is equal to 0.0232 mm^{-1} for 14.1 MeV neutrons and mapping equation 10 over the detection medium thicknesses modeled we obtain the data given in Table 6, which is compared to the results obtained in the MCNPX simulations. As can be seen from the supplied data MCNPX yields more interactions per source neutron than transport theory, where the difference between the two increases as the series multiplexed array increases. Further, taking the ratio of the largest stacking thickness to the lowest stacking thickness results gives 18 for transport theory and 18.96 for MCNPX. Taking the ratio of the latter to the former yields a value of 1.05, which may be due to the number of source neutrons that undergo a secondary interaction while traveling through the detector. The difference between singlular results between transport theory and the MCNPX simulations for a single diamond plate is attributed to the cross section values determined through the ISABEL/Dresner physics models which differs from accepted values. This can be seen in Table 6 where equation 10 was used along with the data in column 4 to determine the macroscopic cross section estimated by the ISABEL/Dresner physics models. It can be seen that for a single diamond plate the physics models estimates a larger cross section

interaction than the accepted value and increases as the stack size increases, which is attributed to the suspected secondary interactions taking place, as previously discussed.

Table 6: Comparison of intrinsic detection efficiency calculated from diffusion theory and MCNPX with increasing active detection volume.

t (cm)	Detection volume (cm^3)	Transport Theory ε (10^{-3})	MCNPX		Ratio of MCNPX/Diffusion Theory
			collisions (10^{-3}/source neutron)	Cross Section (mm^{-1})	
0.5	0.01	11.5	13.4	0.0270	1.17
1.5	0.03	34.2	40.2	0.0274	1.18
2.5	0.05	56.3	66.8	0.0277	1.19
4.0	0.08	88.6	106	0.0280	1.20
5.0	0.10	109	132	0.0283	1.21
7.5	0.15	160	195	0.0289	1.22
10	0.2	207	254	0.0293	1.23

5.4 Conclusions For the Simulated Multiplexing of Diamond Plates for Neutron Detection

The results of these analyses indicate that large multiplexed arrays for both series and parallel stacking techniques produce pulse height spectra with minimal energy resolution loss. It was found that, even for a twenty plate thick multiplexed array, the number of multiple neutron interactions is low and the intrinsic detection efficiency is 25.4 percent when utilizing the ISABEL/Drenser physics model and 20.7 percent when using accepted values for the cross section. The latter agrees well with the difference found in the impinging neutron flux entering the last to the first mesh region, which was found to be 21.1 $\pm$ 0.4 percent. This gives further value to the claim

that approximately five percent of the impinging neutrons are undergoing a secondary interaction within the multiplexed diamond array of 20 plates. It should be noted that the quoted efficiency here competes well with the intrinsic detection efficiency of other systems, such as proton recoil and NE213 neutron detectors, which have efficiencies on the order of one and thirty percent, repsectively.[1] In addition, the reduction of energy resolution due to multiplexing is minimal based upon simulation results and provides a resolution competitive with or better than other neutron spectroscopic detection systems. Further work is required for this novel stacking technique to quantify its capability in detecting multi-energy neutrons and its resolution and intrinsic detection efficiency for such neutron sources. Specifically, a more accurate modeling technique needs to be identified or developed to characterize the response of various multiplexed diamond detection arrays that match the body of experimental work that has been presented for single diamond plates.

Nonetheless, it has clearly been theoretically demonstrated that this multiplexing technique can possibly lead to new spectroscopic neutron detection systems made from off the shelf components that are capable in determining neutron sources with good intrinsic detection efficiency and energy resolution without the immediate need to advancing CVD diamond growth technologies to produce larger diamond crystal volumes. Diamond-based neutron spectrometers will be smaller in size than competitive systems and will be more robust in the field. Experimental analysis of these claims will be presented in section 6.

5.5 Photon Interactions with Diamond and Multiplexed Diamond Arrays

As a final study in the theoretical portion of this work the interaction of various monoenergetic photon sources on series multiplexed diamond arrays were conducted. This work is important because, as the multiplexed array of diamond crystals increases in size, gamma rays that may exist in the environment could interfere with neutron detection through overlapping signals. In addition, as multiplexed arrays get larger they become more capable of gamma ray detection. Therefore, a second goal of this study is meant to give preliminary results to the capability of multiplexed diamond arrays with a primary task of gamma ray detection.

No meshing was conducted in this part of the work because of the long ranges that scattered electrons will have in a multiplexed diamond array. A single pulse height tally was considered for each array simulated and the thickness of the array increased in the same direction as that of the photon source. Also note that these simulations are concerned with a photon flux interacting with diamond when the interaction rate is much less than the speed at which the associated electronic acquisition system can respond. As such the system is operating in pulse mode and not in current mode.[1]

The photon energies simulated in this work were 500 keV, 650 keV, 800 keV, 950 keV, 1.1 MeV, and 1.4 MeV. The number of plates in the multiplexed diamond arrays simulated in this work was one, three, five, eight, ten, fifteen, and twenty. The results from this analysis are displayed in Figures 13 and 14. It can be seen that for single plate exposures the full energy peak has a peak magnitude in the pulse height spectrum that

is over two orders of magnitude lower than the main distribution. The main distribution of the pulse height spectrum is comprised of the Compton continuum and the edge seen corresponds to the Compton edge, whose location in the pulse height spectrum is described by equation 11, where E_γ is the energy of the incident photon on the multiplexed diamond array.[63]

$$Compton\ Edge\ (MeV) = E_\gamma \left(1 - \frac{0.511}{0.511 + 2E_\gamma}\right) \quad 11$$

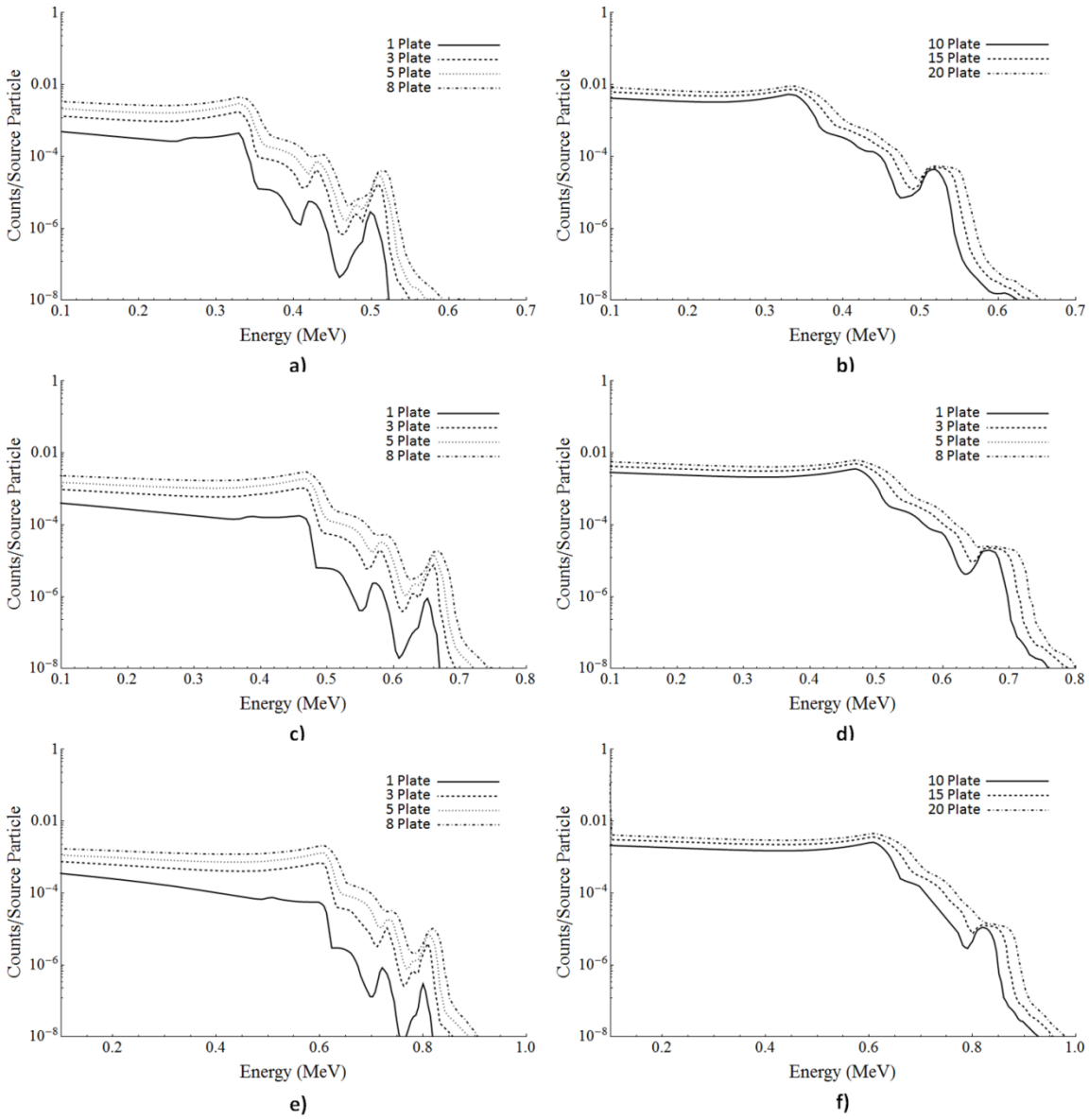

Figure 13: Results from photon expsoures to series multiplexed diamond arrays for energies of a) and b) 500 keV, c) and d) 650 keV, and e) and f) 800 keV.

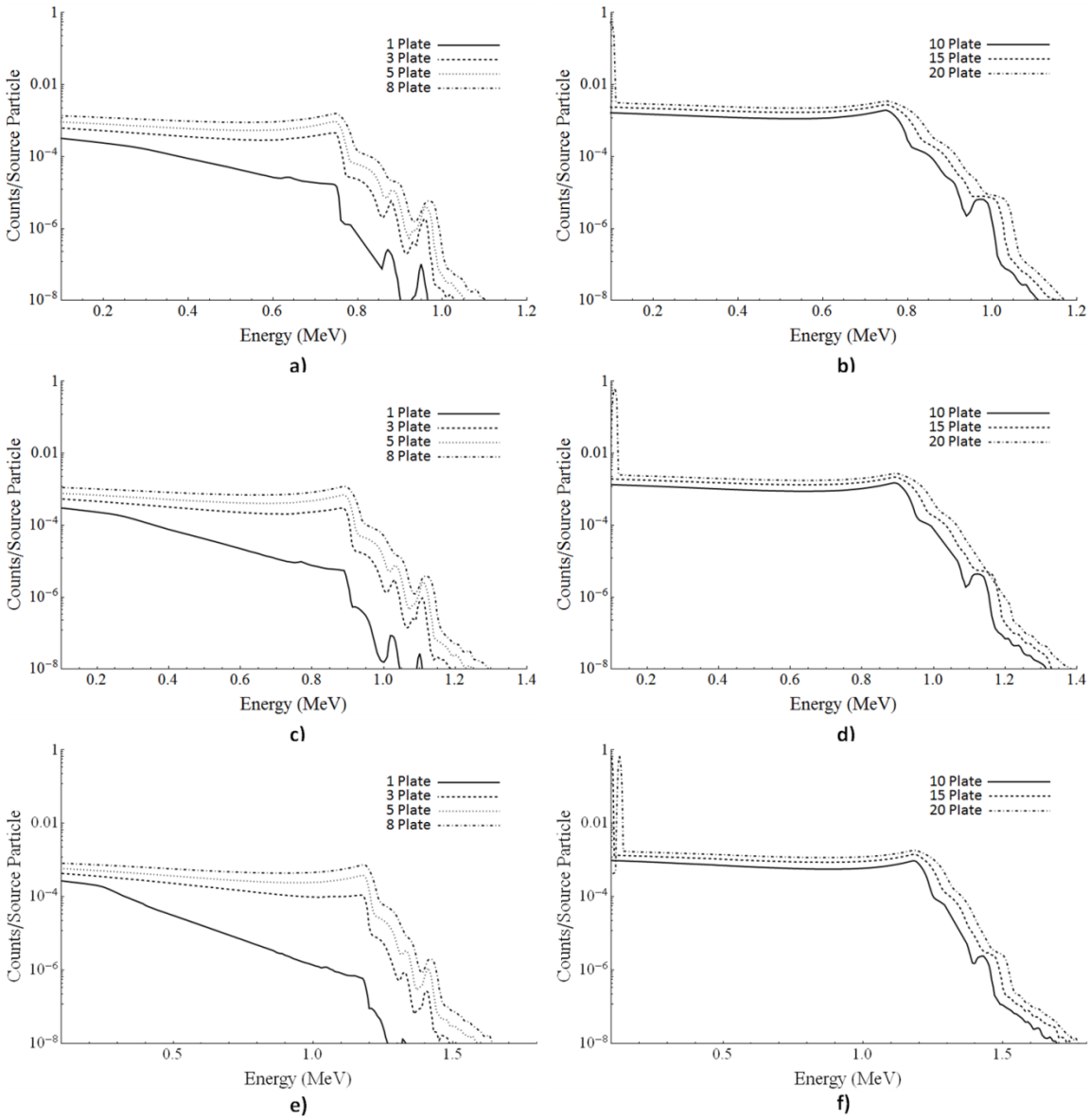

Figure 14: Results from photon expsoures to series multiplexed diamond arrays for energies of a) and b) 500 keV, c) and d) 650 keV, and e) and f) 800 keV.

As the number of diamond plates in the multiplexed array increases the number of interactions increases thereby evolving the pulse height spectrum. Specifically, the number of interactions increases by around two orders of magnitude as indicated in the plots of the results, which is why a log plot was chosen so that a comparative plot could

be presented. In addition, the full energy peak increases in overall probability per impinging source neutron at the same rate as the Compton continuum part of the spectrum, indicating that a full energy peak is not likely to be seen in a real experiment utilizing a large array of diamond crystals. In addition, as the photon energy increases the full energy peak in the observed spectra occur at a lower probability, further indicating that an array of diamond plates is not good for high energy photon counting utilizing this peak. Still, the use of the Compton edge and continuum is possible for photon detection and in the case of neutron detection the effect of photons need to be taken into account as the probability of seeing this interaction even for a single diamond plate at lower photon energies is approximately the same as that for neutron interactions. This indicates that the signals from each will overlap and discrimination techniques would be required to tell the two apart.

6. EXPERIMENTAL RESULTS

Now that several simulations have been presented on the advantages of larger diamond crystals for neutron and photon detection experimental results are required to give a tangible hold on the concept of multiplexing. In the following sections the processes that were taken to prepare the acquired diamond samples, the results from alpha particle and neutron exposures, and the analysis of multiplexing will be presented.

6.1 Electronic Grade Diamond Sample Characterization

Eight electronic grade single sector (typically) diamond crystals were acquired from Element Six for this work.[46] The diamond samples are quoted to have a nitrogen concentration of less than five parts per billion and a boron concentration of less than fifty parts per trillion. These impurity concentration levels is the main factor that allows these diamond samples to be characterized as electronic grade, per the discussion in Section 3.4 on the electronic properties of diamond. The diamond samples all have a cross sectional area of approximately 2x2mm^2 and the thicknesses of each are given in Table 7, where the samples have labels EGDS (electronic grade diamond sample).

Table 7: Thickness of all EGDSs used in this work.

EGDS	1	2	3	4	5	6	7	8
µm	521	511	495	495	467	498	470	511

To characterize the samples obtained the EGDSs were scanned using two apparatuses. Note that only EGDS 3 was tested in these characterizations because the

diamond samples were obtained from the same vendor and it was assumed that the properties of one diamond sample is the same as all the others within the tolerance of the measurement systems used. The first characterization device utilized was a NuSpec-DeltaNu microRaman**.** The obtained spectrum is displayed in Figure 15. It can be seen that there is a single peak at 1332cm^{-1} and is the expected spectrum from a single crystal diamond. The measurement was taken at various locations across EGDS 3 and the results were identical, indicating a very homogeneous sample.

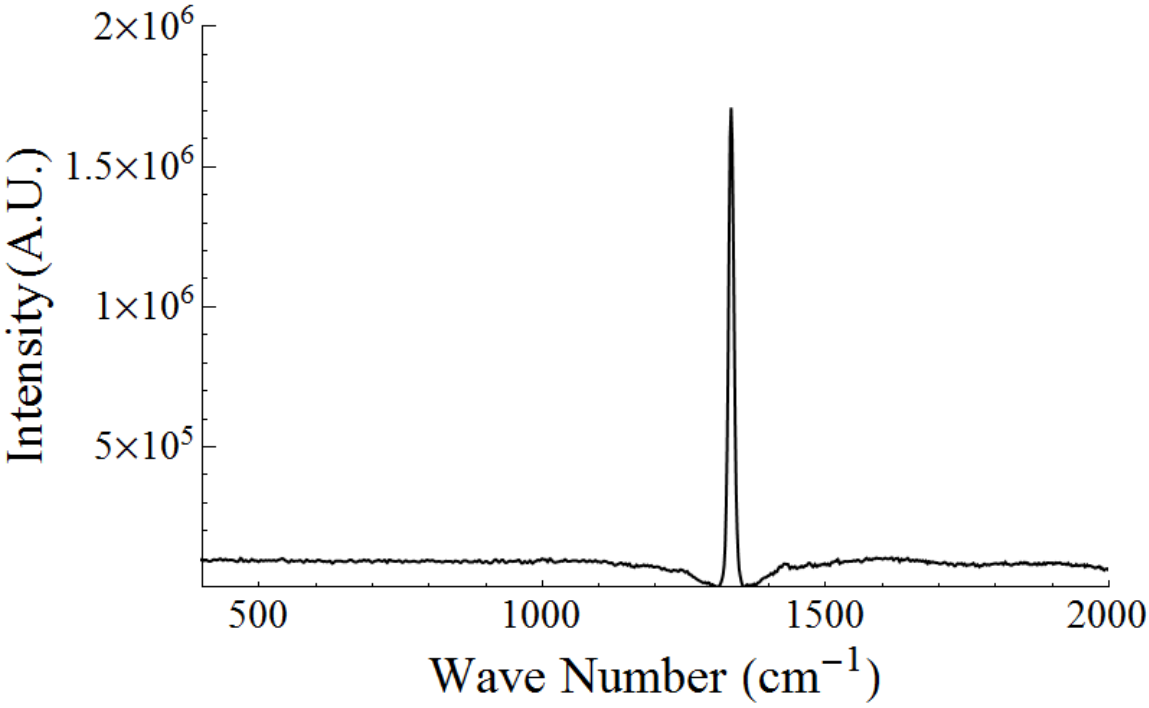

Figure 15: Raman spectrum of EGDS 3.

The second characterization conducted was the measurement of the transmission spectrum of EGDS 3 to monochromatic light in a wavelength range from 200-900nm. This was conducted using an S.I. Photonics Model 440 UV/Visible

Spectrophotometer. The band gap of diamond has been previously defined to be 5.47eV at room temperature which corresponds to a wavelength of 227nm. By measuring the transmission of the sample to monochromatic light the band gap of the material can be determined by observing the location where the transmission of the sample sharply decreases. In addition, this measurement technique allows for the characterization of any significant energy levels within the forbidden region of the band structure of the diamond sample, such as the 1.7eV energy level created by nitrogen.

An additional attachment was constructed for the spectrophotometer that allowed the precise mounting of two fiber optic cables perfectly aligned with each other. This system created a small region between the two fiber optic cables where the sample could be placed, protected from any ambient light. A picture of this measurement apparatus and the results from EGDS 3 are displayed in Figure 16. From these results it can be seen that photon absorption starts to take place around 236nm, which corresponds to an energy of 5.25eV. This energy is lower than the band gap of diamond but it must be pointed out that quantum thermal excitation must be taken into account in these results, such that excitation starts at a value slightly lower than the band gap energy. This has been seen in other UV-Vis measurements on diamond.[13, 29] Significant absorption does not start to take place until a wavelength of about 227nm, which corresponds to an energy of 5.47eV, which is the expected result for the band gap energy of diamond.[32] In addition, the impurities present in the diamond sample are below the spectrophotometer's capability to distinguish in the measured transmission spectrum, as is indicated by the flat line at wavelengths greater than 236nm. This give

credence to the quality of the diamond obtained and was considered sufficient preliminary evidence in this work that the diamond was of a quality worthy of testing their electrical properties.

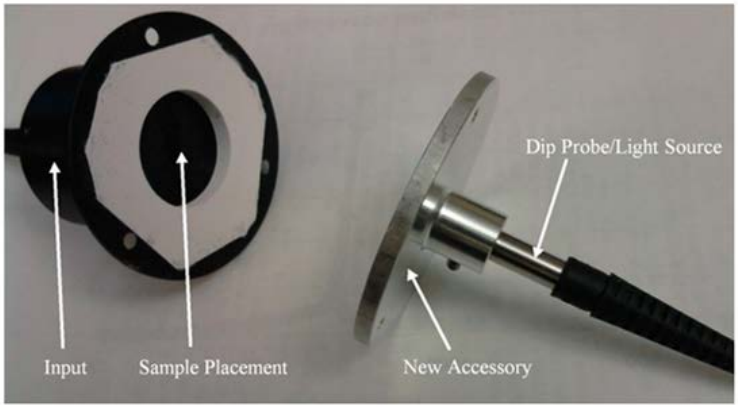

a)

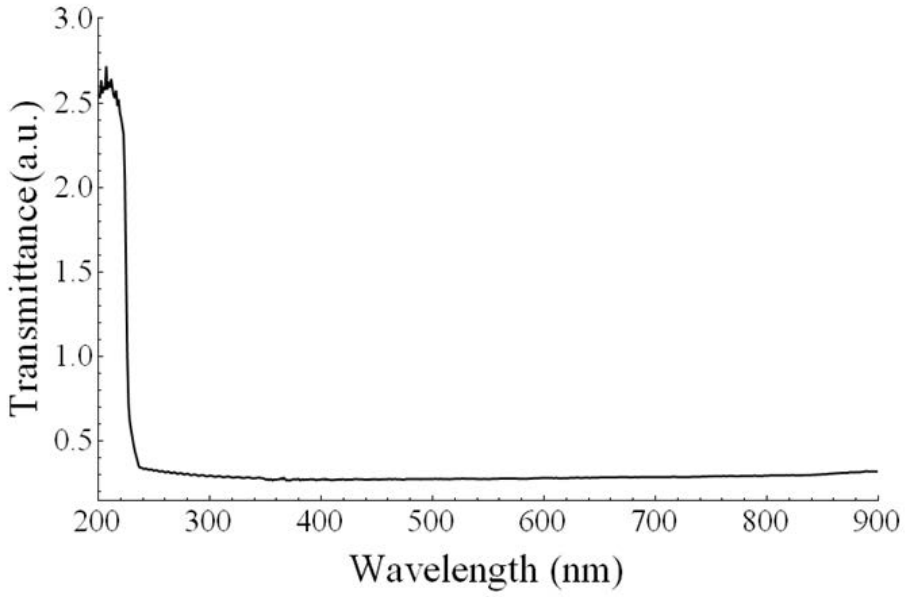

b)

Figure 16: The a) experimenal apparatus used to detetermine the spectral abosrbance of EGDS 1-8 and b) the results of this analysis for EGDS 3.

6.2 Electronic Grade Diamond Sample Preparation

6.2.1 Electrical Contact Scheme

After the virgin EGDS characterization was complete the samples were prepared for electrical contact formation, which required the chemical cleaning and surface preparation of all EGDSs. The chemical cleaning is meant to remove any contaminants on the surface of the diamond samples that could cause poor adhesion or trapping centers. Chemical processes can also prepare the diamond through surface termination and is a very important aspect to take into account in sample preparation. Two types of surface terminations are most common. The first is hydrogen termination. Hydrogen termination has been found to increase surface conductivity significantly.[28, 64, 65] This is not beneficial to radiation detection that lies in the interaction of the radiation particles within the bulk of the active detection medium. The reason is that the potential applied to collect the created charge from the radiation interactions is strongly diverted along the surface rather than through the bulk. This increases the dark current of the system as the system is now operating in an equivalent circuit of two resistors with the surface representing a resistance much less than that of the bulk. This effect can be alleviated through oxygen termination. An oxygen terminated surface exhibits a high resistivity[61] and it has been suggested that oxygenation of diamond surfaces increases contact adhesion when utilizing carbide forming metals.[26, 66] This implies that the oxygenation step should take place either before or after contact formation, depending on whether carbide forming metals are used in contact formation on diamond.

The formation of metal contacts on diamond can be tricky due to the nature of semiconducting diamond and its surface. The main fabrication issues are the difficulty in the mechanical adhesion of the contact, which is more difficult the lower the surface roughness is, the need of good injecting contacts, being polarization free, and the need of stable and durable contacts with reproducible results.[26] The problem of mechanical adhesion has already been discussed, where oxygen termination seems to alleviate this problem when carbide forming metals are used. Second, polarization occurs when the electrical contacts are not able to extract electrons faster than they are produced, creating an opposing electric field and degrading sensor performance by limiting electron flow and giving non-uniform electric fields within the detection medium.[26]

The oxide layer produced on the diamond surface for surface termination and for contact mechanical adhesion also produces a MOS structure when metal is deposited on top. Because of this insulating oxygen layer, no current should be generated when no bias is applied across the semiconductor.[67, 68] However, the work function of an oxygen terminated diamond surface can be as high as 5.8eV and that of titanium and chromium (carbide forming metals) are 4.3eV and 4.5eV, respectively.[26, 67, 69] This means that a potential barrier exists and impedes electron flow, which can create polarization effects in high flux fields or long exposure times.[15, 21] However, several research groups have used these metals in contact formation, but they were only Ohmic after a post metallization annealing process.[70-72] A. Gibliati *et al.* did a study on using titanium and chromium and indicated that they are partially rectifying, but did not indicate an annealing step after contact deposition, which could mean that the carbide

properties at the interface were not present.[26] It has been suggested in that work that an oxide layer forms at the interface between the diamond sample and the carbide forming metal thereby increasing the contact resistance and creating non-Ohmic properties.[26, 61] It should be noted that tunneling is often the reason behind Ohmic contact formation and the results from the investigations conducted by the group making this claim showed that the contact pattern EGDS/DLC/Pt/Au produced an Ohmic IV (current-voltage) curve whereas EGDS/Ti/W and EGDS/Cr/Au contacts produced somewhat Ohmic contacts.[26, 59-61] By somewhat Ohmic it is meant that the IV curve was not linear, indicating that the resistance of the EGDS was not constant over the voltages used in the voltage sweep. However, the shape of the curve was not concave enough to follow an exponential trend, indicating that these contacts were not completely Schottky, or rectifying. In addition it is claimed that the creation of a graphitic, or diamond like carbon, region a few nanometers thick between a high work function metal and the diamond surface creates a tunneling junction for the electrons to enter and leave the diamond sample.[26, 43, 52]

This may be the effect seen by many other research groups, where high temperature annealing graphitizes the surface under the metal contact, such as titanium, thereby forming a defect layer which could lower the barrier, increase tunneling, or both,[60, 72, 73] although the true effect of oxygen termination on the surface is not known at this point.[71] In any case, Ohmic contact formation has been well established using carbide forming metals and post annealing treatments, whereas the use of DLC has also been shown to produce similar results. Therefore, it seems that

Ohmic contacts are formed with diamond when the metal-semiconductor interface is not abrupt. In the literature the most commonly used contact metals with successful results for radiation detection have been in the use of carbide forming metals and so this method of contact formation will be adopted here.

The two most common carbide forming metals cited in the literature for contact formation on diamond are chromium and titanium. Titanium seems to be utilized more than chromium and studies have shown that titanium produces a less rectifying behavior than chromium.[26, 71, 74] Of course titanium will slowly oxidize when exposed to oxygen and therefore an inert layer must be applied on top of the diamond to prevent this, especially during the thermal annealing process necessary to form the carbide junction at the surface. Gold is the most common choice for the inert top metal layer because of its good bonding properties. However, titanium and gold are soluble in each other and during annealing the titanium can diffuse to the surface and oxidize, increasing the contact resistance. This is why platinum has been used between the titanium and gold layers of the contact because it acts as a diffusion barrier between the two.[73]

6.2.2 EGDS Cleaning and Metallization Process

Due to the choice of titanium being the contact metal on the diamond and the need for an electrically resistive surface the cleaning process utilized for the EGDSs was tailored at chemical oxidation of the diamond surfaces. The specific cleaning process used for all diamond samples is given below.

1. Boil in Aqua Regia/HCl:HNO_3 (3:1) for thirty minutes at 100^{o}C. This step is conducted to remove metals from the surface of the EGDSs.
2. Rinse in deionized (DI) water.
3. Boil in Base Piranha/NH_4OH:H_2O_2:H_2O (1:1:5) at 100^{o}C for thirty minutes. This step is conducted to remove particles and organics from the surface of the EGDSs.
4. Rinse in DI water.
5. Boil in Piranha/H_2SO_4:H_2O_2 (4:1) at 120^{o}C for thirty minutes. This step removes any graphitic top layers on the EGDSs and partially oxygenates the surface.
6. Rinse in DI water.
7. Boil in HNO_3:H_2SO_4:$HClO_4$ (1:1:1) at 150^{o}C for thirty minutes to further oxygenate the surfaces of the EGDSs.
8. Rinse in DI water.
9. Storage in reagent grade acetone.

Note that step numbers five and seven represents the final chemical processes which oxygenates the diamond surface. As was pointed out an oxygenated surface is needed for high surface resistivity and a good electrode contact adhesion. After cleaning the EGDSs were transferred to a class 100 clean room where they were further prepared for metallization. Note that the best way to produce electrical contacts with extreme precision in its pattern on the surface of any material is through photolithographic techniques. However, these capabilities were not available and cruder physical masking processes were required. Kapton tape was used to physically mask the edges of the

diamond. Although effective, the actual contact area on any given side is not well defined and varies between the two faces of a given EGDS and between the EGDSs. This means that the active detection volumes between the EGDSs are different and will be seen in their use for neutron detection in section 6.5.

To form the contacts on the diamond thermal evaporation utilizing a three stage thermal evaporator and tungsten boats was used for titanium and gold. For platinum the melting temperature is too high and the vapor pressure too low for effective evaporation and so sputtering was used. The sputtering was conducted using a Kurt J. Lesker 2 inch Torus RF sputtering gun. Although the sputtering gun was mounted inside of the thermal evaporator vacuum chamber there is no automated sample movement to get an accurate placement of the EGDSs for contact formation between the thermal evaporation and sputtering stages. As such an extender arm was constructed utilizing ball joint arms that allowed a mounted sample to be manipulated to optimum position for metal deposition. Still, this adjustment required opening the vacuum chamber between deposition processes and as such 20nm of gold was thermally evaporated on top of the titanium layer to prevent oxidation during the transition to sputtering platinum.

After one side of the diamond had the formed electrical contact the EGDSs were removed from the evaporator, the Kapton tape was removed and the EGDSs were flipped over and remasked. This was a delicate process because the electrical contacts formed on the first side of the diamond are very sensitive at this stage. The reason is that carbide formation at the EGDS-titanium interface has yet to take place and requires

thermal annealing. The final metallization pattern produced was Ti/Au/Pt/Au (50nm/20nm/25nm/200nm).

To gain mechanical stability and better Ohmic properties of the formed electrical contacts on the EGDSs they were thermally annealed. It has been found that the temperature in the annealing step must be raised above 400^{o}C to stimulate carbide formation but kept below about 700^{o}C to prevent graphitization of the diamond.[66] This is the general guidelines followed during the thermal annealing of all diamond samples.

The annealing chamber consisted of a bell jar and a mechanical pump. A Tungsten wire was coiled and fed through a block of boron nitride. The boron nitride served as the heating element in the annealing process. Boron, however, can diffuse into diamond if the temperature is high enough. It was found in the literature that the diffusion coefficient of boron into diamond at 800^{o}C is 10^{-19} cm^{2}/s.[75] This indicates that minimal doping of the diamond sample should take place because the annealing process is kept well below this temperature and the total annealing time is relatively small. However, for preventative care, the EGDSs were placed inside of an alumina crucible with a lid to help prevent contamination with boron during the annealing process. A second crucible was placed at the mirror image on the boron nitride block with respect to the crucible that contained the EGDSs. A thermocouple was placed inside this crucible to estimate the temperature of the base of the alumina crucible that contains the EGDSs. Another thermocouple was placed on the very center of the boron nitride to measure the annealing substrate temperature as well. The chamber was maintained at a pressure of one millibar and a continuous flow of helium was introduced into the

chamber. This was done to flush out any contaminant gases that may outgas from the chamber wall during annealing. In addition, the helium gas passed through an oxygen scrubber consisting of a pipe full of copper threads heated to a temperature above 750^{o}F. This was done to ensure that any oxygen contamination in the helium gas supply was removed before entering the annealing chamber through oxidation of the copper threads. The temperature versus time annealing process for EDGSs 1-2 and EGDSs 3-8 are shown in Figure 17.

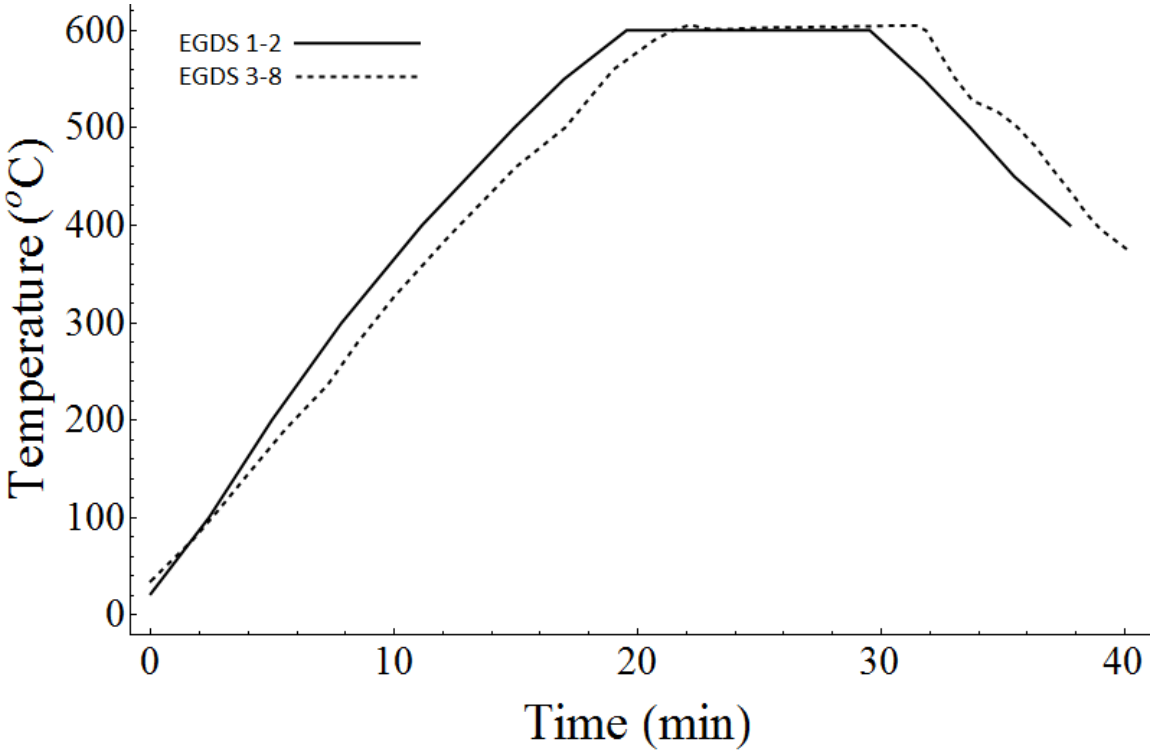

Figure 17: Thermal annealing temperature-time curve followed for the EGDSs during preparation.

After the annealing process it was found necessary to further oxygenate the surface of the EGDSs to increase surface resistivity. This is required because it was found

that current flowed across the surface rather than through the bulk if this is not done. The plasma treatments were conducted using a Harrick Plasma Cleaner PDC-32G operating in an air vacuum plasma on high RF setting for three minutes a side. The final step in the contact formation process was testing contact adhesion as well as a final cleaning process to remove any sample contamination. Both of these steps were completed through an ultrasonic bath in reagent grade acetone for ten minutes. It was found that all contacts on the EGDSs were mechanically stable. A photograph of EGDS 1 is given in Figure 18.

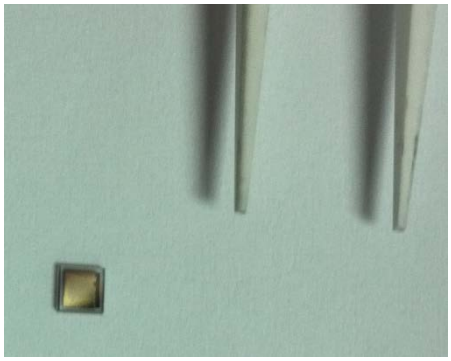

Figure 18: Picture of fully prepared EGDS ready for experiments.

6.3 Electrical Characterization of EGDSs

6.3.1 Current-Voltage Measurements

The next task in sample characterization was to take IV measurements on each EGDS to characterize its linearity and resistance. The latter is important because it dictates the leakage, or dark current that will flow in the system. A large dark current is undesirable because it raises the noise floor and therefore the lower limit of detection

of detection system. At this point it is important to point out that the diamond samples are not to be permanently mounted to any detector housing because of the need to characterize each diamond sample separately and then in a multiplexed configuration. It is for this reason that the constructed system pictorially described in Figure 19 a) was utilized in the IV measurements. In this measurement system a spring loaded electrical connection point was aligned with a narrow metal rod that was soldered to the end of a bulk head mounted SHV connector, where the spring loaded pin was soldered to a bulk head mounted BNC connector. The EGDSs were held in place between the metal rod and the spring loaded pin. The chamber wall was used as a noise shield and this system was further contained within a grounded metal box for further noise reduction and shock hazard safety. The IV measurements were conducted through the use of a Keithley 6487 picoAmmeter connected to a PC and data collection through ExceLINX. A voltage sweep between -500V and 500V was conducted in steps of 25V for each EGDS. The results of these measurements are given in Figure 19 b) through d).

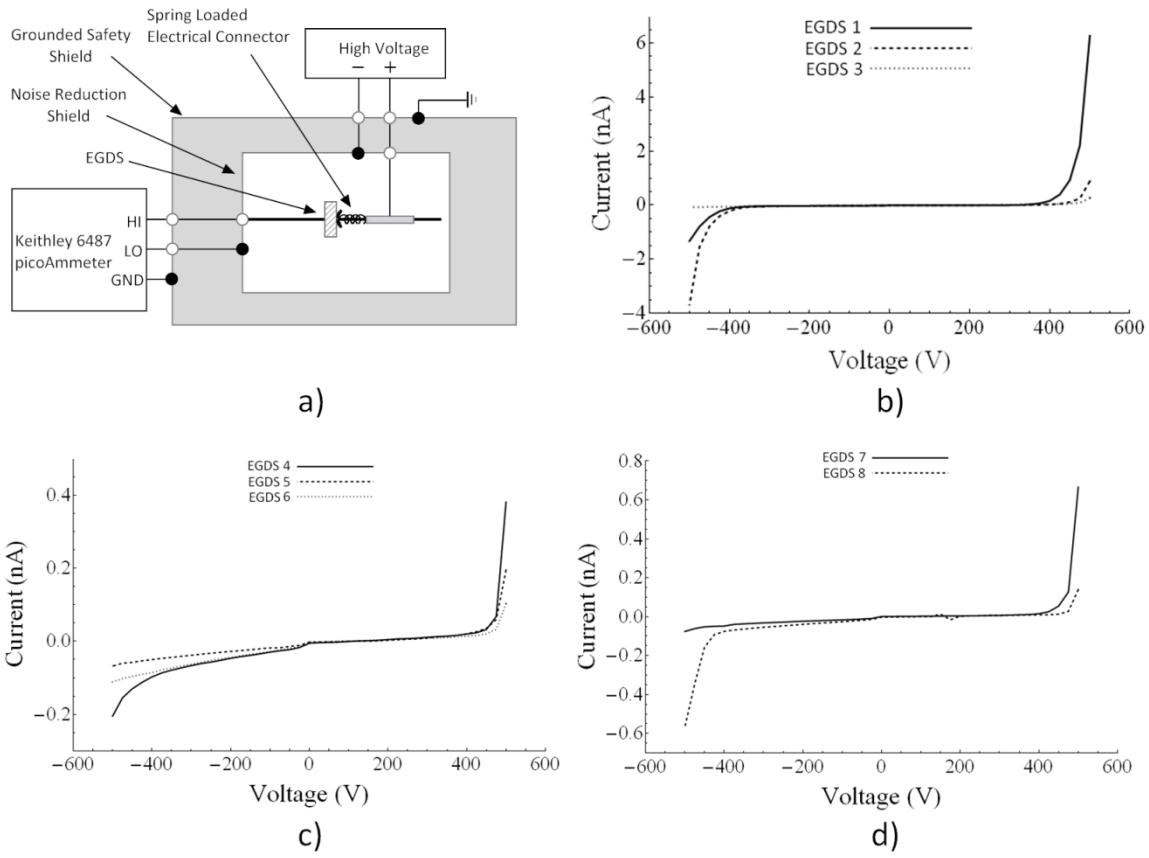

Figure 19: In part a) the measurement system used for the IV measurments is shown. In parts b) thorugh d) the IV characteristics of EGDS 1-8 are displayed.

As can be seen the slope of the IV curves displayed are relatively linear for all EGDS at low to moderate applied biases. At higher voltages the curves of almost all EGDS begin to show a nonlinear relationship between current and voltage. This could be due to thermionic emission of electrons over the barrier or due to surface conductivity starting to play a role at these higher biases. However, as will be shown in Section 6.3.2 the required bias for one-hundred percent collection efficiency is on the order of one-hundred volts and far from this non-linear region. As such these results indicate that the EGDSs behave Ohmically for the region of operation that is of interest.

6.3.2 Alpha Particle Exposures

The next task completed for electronic characterization of the EGDSs was their exposure to alpha particles and the determination of the charge collection efficiency versus applied bias. This data will give vital information on the quality of the EGDSs along with the stability of these values across all the samples. The mounting system that was developed for these measurements is shown in Figure 20. This chamber consisted of a hollow aluminum cylinder (housing base) with a plug containing a bulk head mounted SHV connector to it that has a clearance of only a few thousandths of an inch. A threaded hole was included into the side housing base and filled with a set screw to hold the plug into place. The end of the SHV connector on the plug has a pin soldered to it and the housing base had a 0.5mm hole drilled though the center of the base to allow alpha particles to interact with the EGDSs. Further, a pedestal was added to the interior of the base housing where the center hole was at the center of this pedestal. The remaining area of the base in the housing base was covered with KonForm,® a highly resistive material. This setup allowed the EGDSs to be placed on top of this pedestal and pressure contacted to the pin of the SHV connector. The pedestal and resistively coated floor of the housing base was added due to observed breakdown without it. IV measurements were taken with the EGDSs to verify that they were similar to that obtained with the IV measurement chamber.

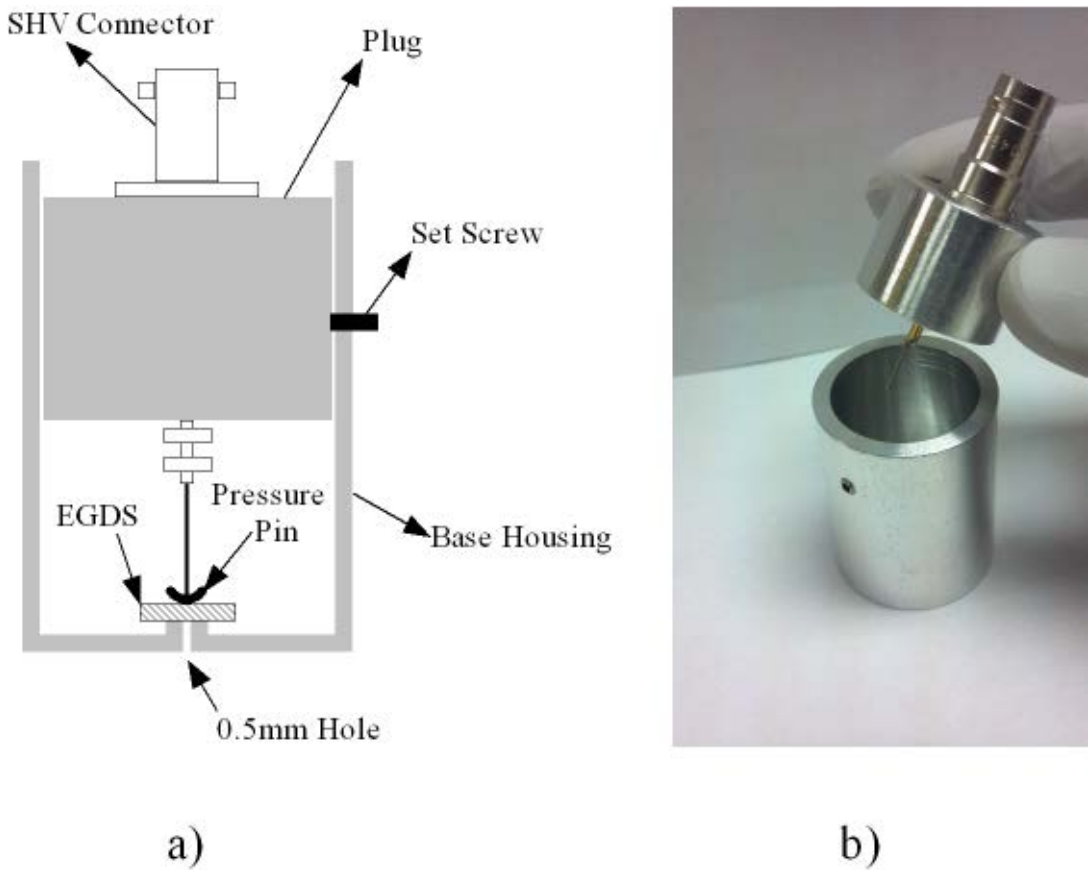

Figure 20: In part a) the diagram of the EGDS mounting sample is displayed and the actual detector housing is shown in b).

The center hole in the base housing allowed the alpha particles to travel through the electrical contacts on the diamond samples and deposit energy within the bulk. The alpha source used was a ^{210}Po high activity source from Eckert and Ziegler. This alpha source is not spectral grade and this makes the determination of the response, specifically the charge collection efficiency and energy resolution, difficult due to the broad peak and difficulty in determining the peak location. To account for this difficulty the energy spectrum of the emitted alpha particles were first measured using a Canberra Quad Alpha Spectrometer Model 7404, which utilizes a silicon surface barrier

detector. The determined alpha energy spectrum is given in Figure 21. The energy calibration was obtained through the exposure of a low activity ^{239}Pu source and it was assumed that the alpha spectrometer behaved linearly in the region of interest. The energy resolution of this alpha spectrometer measuring this non-spectral grade ^{210}Po alpha source was determined to be 2.96 percent.

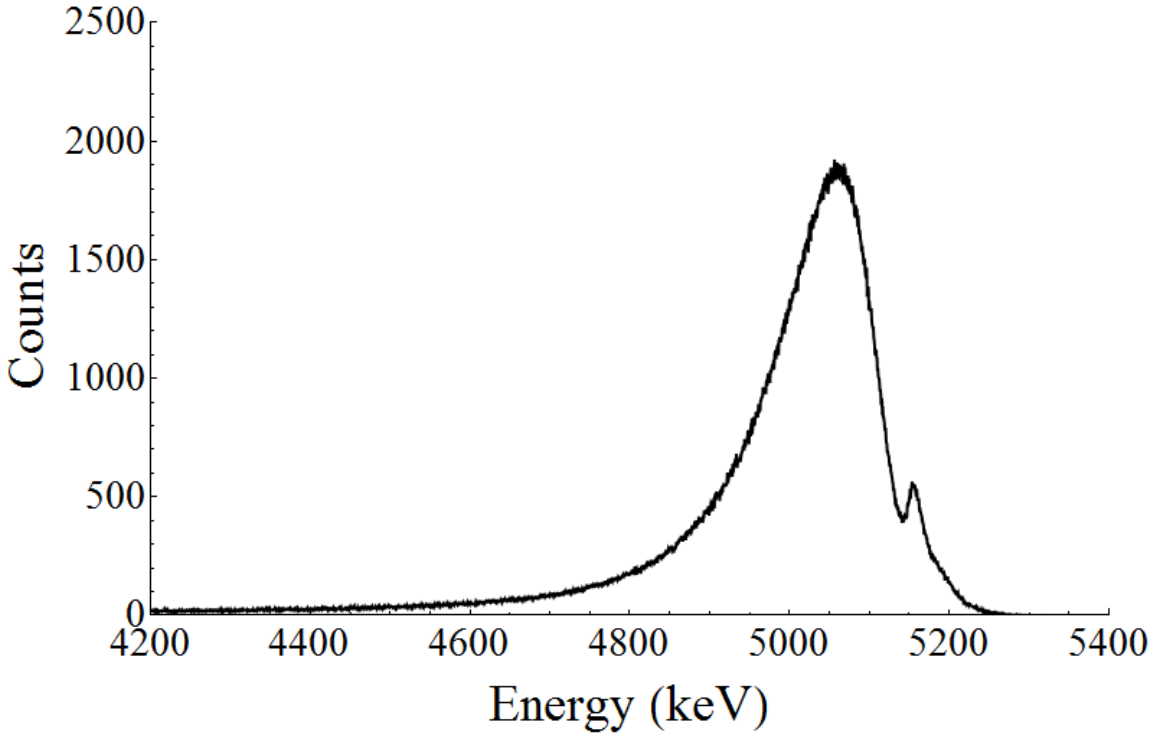

Figure 21: ^{210}Po high activity source spectrum used for the EGDS exposures.

The detector housing base was placed approximately two millimeters away from the surface of the source during all measurements. The detector was connected to an Ortec 142PC preamplifier through a six inch RG59B/U coaxial SHV cable with a nominal 21pf/ft capacitance. The preamplifier output signal was sent to a Canberra model 2026

amplifier set to a gain of 10 and a shaping time of 0.5µs. The bipolar output was sent to a Canberra Multiport II multichannel analyzer buffer and data collection was conducted through Genie™ 2000.[76] A diagram of the electronic setup is displayed in Figure 22.

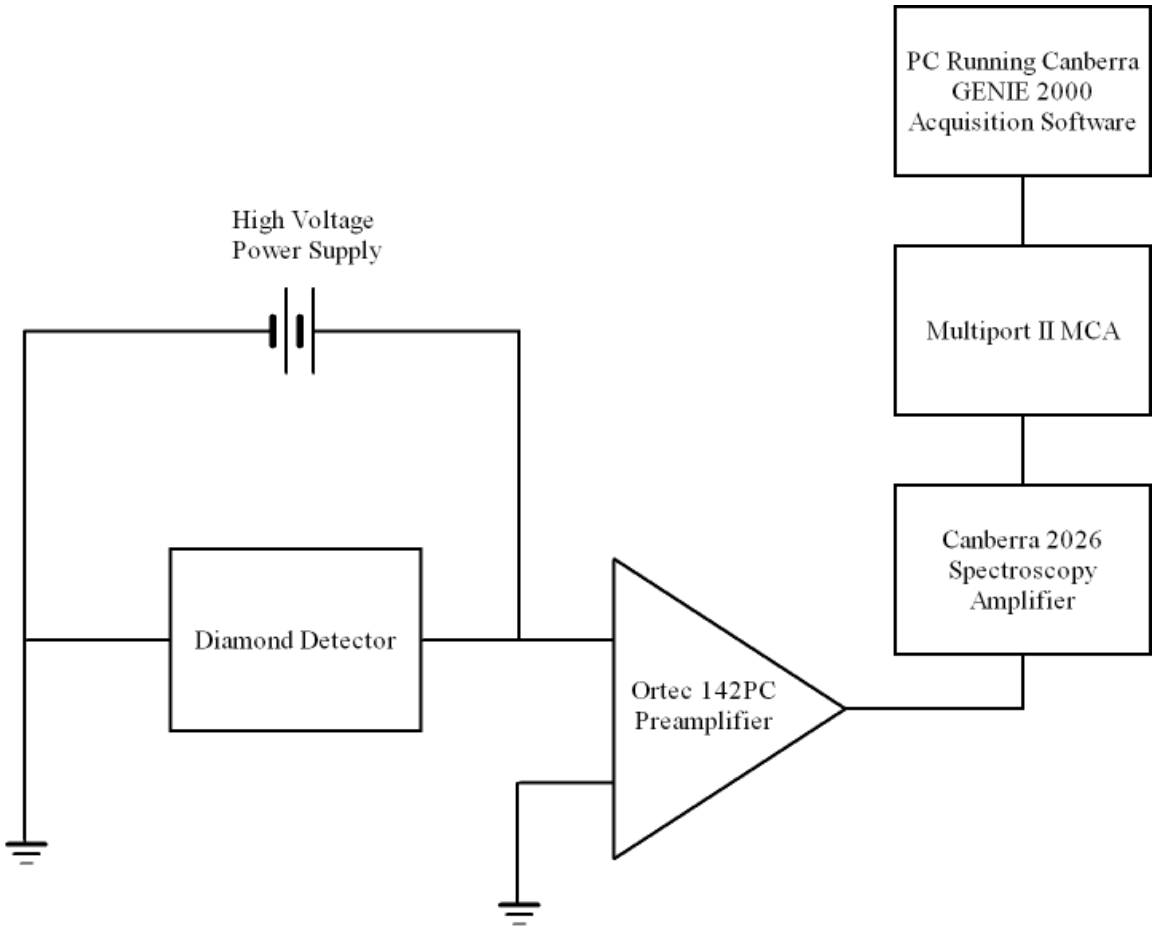

Figure 22: Basic circuit diagram describing the electronics used in all EGDS radiation measurements.

During the alpha exposures varying potential fields were applied across the diamond to characterize the charge collection created from the alpha particle interactions within the diamond. Since the preamplifier is charge sensitive the amount

of charge collected is directly proportional to the output voltage generated by the preamplifier. Therefore, by observing the change in the channel number corresponding to the alpha peak on the spectrum output as the applied bias changes some important information can be inferred. As was introduced in section 3.4, Hecht's theory describes the collected charge versus the mobility, the trapping time constant, and the generated charge as a function of distance that the charge has to travel in the detection medium before reaching the charge collection electrode.

Therefore, the plot of the channel number versus applied bias should produce a shape described by equation 6 when all interactions occur near the surface of one of the electrodes. Further, the detector thickness is equal to the charge collection distance at 63.2 percent charge collection efficiency and the ratio of the detector thickness to the applied electric field at this collection efficiency is equal to the mobility-trapping time constant product.[23, 47] So the plot previously described can be used to determine what bias is required to obtain 63.2 percent collection efficiency. With this in hand the mobility-trapping time constant can be estimated through equation 12, where $\mu_{e/h}$ is the mobility and $\tau_{e/h}$ is the trapping time constant of electrons or holes, respectively, W is the detector thickness, and E is the applied electric field across the diamond plate.

$$\mu_{e/h}\tau_{e/h} = \frac{W}{E} \qquad 12$$

However, as was previously pointed out, the ^{210}Po alpha source is not spectral grade and so determining exactly what channel corresponds to the peak maximum requires some post processing. To determine the peak maximum for a given measurement the square root was taken of the number of pulses measured in each

channel. Then it was determined how many channels had error bars that overlapped with the channel number corresponding to the maximum number of observed counts. All of these values were averaged and a standard deviation was found. In this manner an uncertainty in the spectral maximum for a given measurement was determined. An example of the differing spectrums versus applied bias for EGDS 1 is given in Figure 23. It can be seen that as the bias increases the spectrum shifts to higher channels numbers asymptotically and eventually approaches a constant value, which corresponds to complete charge collection. In addition, a single spectrum is given for EGDS 1 in Figure 23 b) with an applied bias of +50V. Note that the error defined through Poisson statistics is given in this plot and it can be seen that there are indeed a few data points that have error bars that overlap with each other.

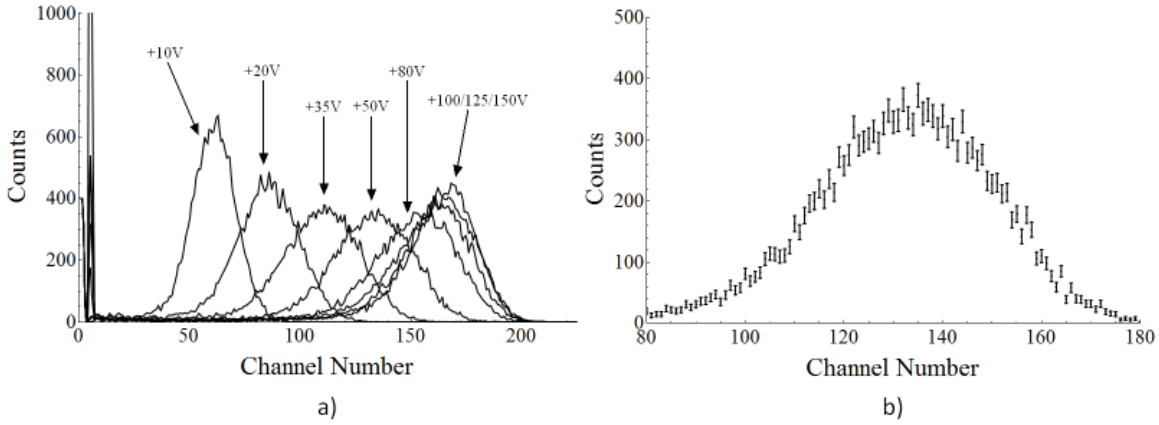

Figure 23: The spectral results from ^{210}Po alpha exposures on EGDS 1 with a varying applied voltage is displayed in a) and one of these curve with error bars found through Poisson statistics is shown in b).

Taking the ratio of the determined peak height channel numbers for all spectra for a given EGDS to the determined maximum channel number found for all measured spectra and plotting it versus the applied bias produces a charge collection efficiency curve. This curve for all EGDSs is given in Figure 24 applying a positive bias and Figure 25 for applying a negative bias. Note the error bars associated with each data point. This large error makes it hard to accurately determine at what bias the charge collection efficiency is equal to 0.632. To deal with this difficulty linear interpolation was used between the two data points that surround a y-axis value of 0.632 to determine the required bias. Further, linear interpolation was conducted between each data point's value plus its error and minus its error. This process yields a value for the required bias plus an uncertainty in the applied bias. The determined mobility-trapping time constant products of electrons for all EGDSs were determined by utilizing this data and equation 12 and are given in Table 8. The data for the mobility-trapping time constant product for holes is given in Table 9. It can be seen that the values determined for these EGDSs are two orders of magnitude lower than that reported by Isberg *et al.* in 2004,[45] which represents the best reported values to date, but the values indicated are still of sufficient quality to be considered good for radiation detection. In addition, it can be seen in all plots that the charge collection efficiency is near 100 percent at a bias less than or equal to $\pm$175V. Therefore, a bias of +175V will be used in all neutron exposures.

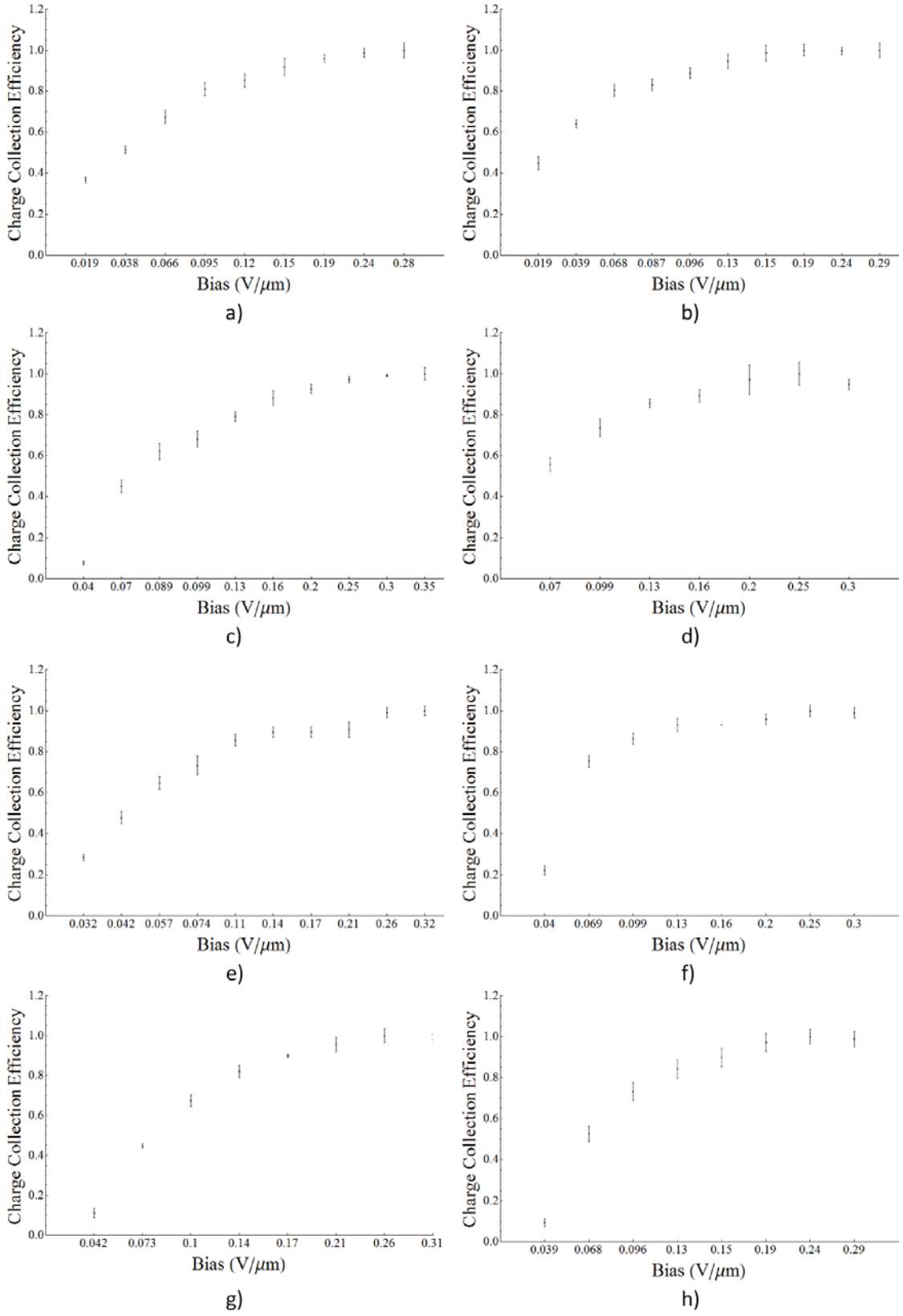

Figure 24: CCE measurements using a positive bias for EGDS 1-8 in a)-f), respectively.

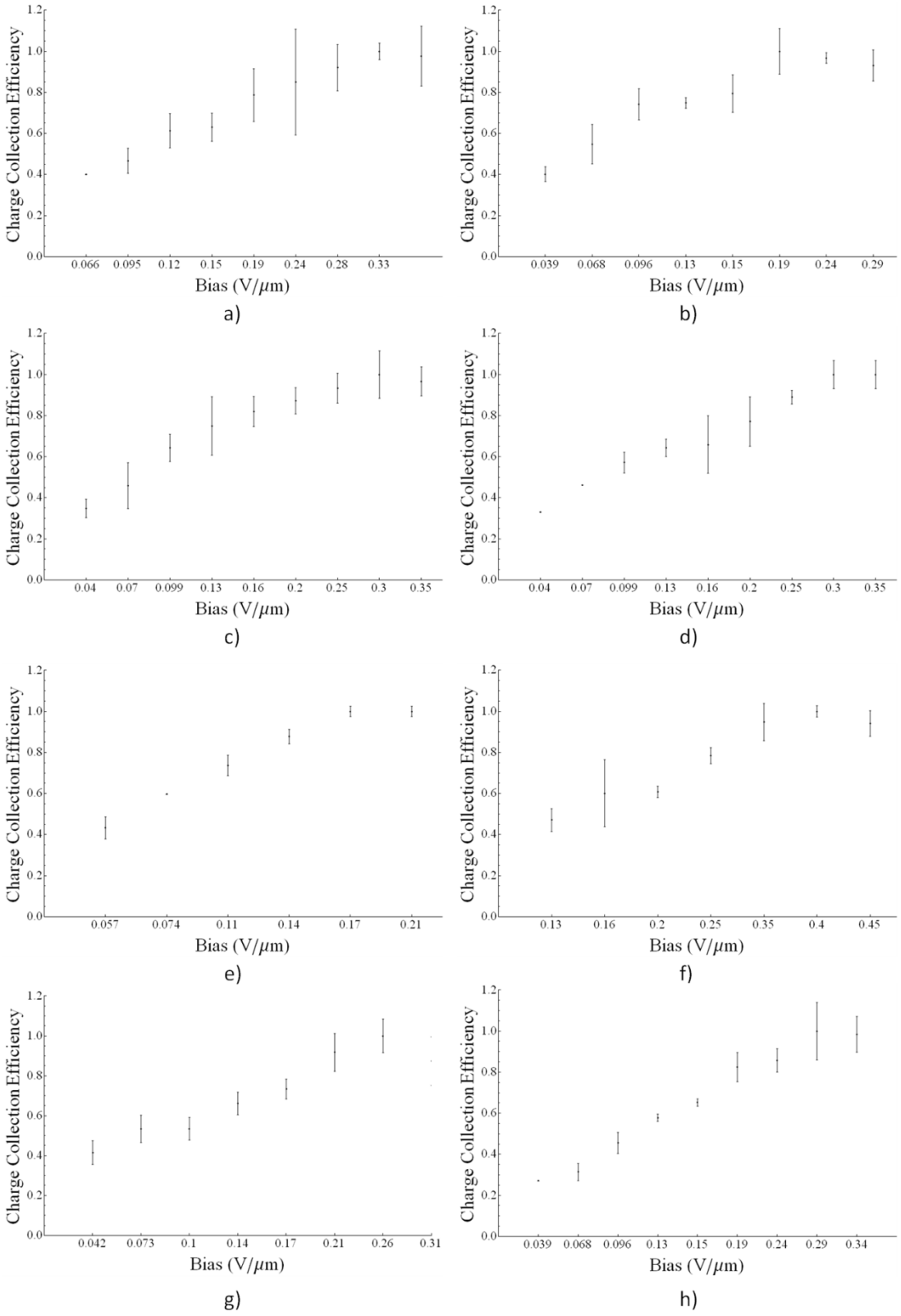

Figure 25: CCE measurements using a negative bias for EGDS 1-8 in a)-f), respectively.

Table 8: Determined electron mobility-trapping time constant product for EGDS 1-8.

EGDS	Median μτ ($10^{-6}cm^2/V$)	Maximum μτ ($10^{-6}cm^2/V$)	Minimum μτ ($10^{-6}cm^2/V$)
1	89.9	97.8	82.2
2	140	151	128
3	55.2	59.5	51.6
4	61.2	65.8	56.8
5	85.8	90.1	81.8
6	80.9	82.9	78.9
7	49.1	50.8	47.2
8	63.6	68.3	59.3

Table 9: Determined hole mobility-trapping time constant product for EGDS 1-8.

EGDS	Median μτ ($10^{-6}cm^2/V$)	Maximum μτ ($10^{-6}cm^2/V$)	Minimum μτ ($10^{-6}cm^2/V$)
1	41.7	47.1	36.1
2	64.7	79.0	56.4
3	51.4	59.3	47.3
4	40.3	48.2	35.6
5	53.6	59.1	49.2
6	30.4	31.4	29.3
7	29.8	32.6	27.4
8	35.4	37.1	33.8

6.4 Series Multiplexing and Alpha Exposures

Now that the mobility-trapping time constants of electrons and holes for each diamond sample have been evaluated the concept of series multiplexing was applied to alpha particle detection. It is true that a thicker active diamond detection medium has no benefit for alpha particle detection, but the characterization of charge transport across the multiplexed array can be characterized and the subsequent output pulse measured by the charge sensitive preamplifier. As such EGDS 2 was placed on top of EGDS 1 in the diamond detection box shown in Figure 20 in section 6.3.2. The alpha particles impinged onto the bottom of EGDS 1 and the electronic acquisition system is

identical to that described in Figures 20 and 21. The spectra and charge collection efficiency plot obtained is displayed in Figure 26. Here is can be seen that the voltage required to maximize the signal was much larger, where the charge collection efficiency curve seemed to plateau at a voltage between +425V and +500V. Using +500V this corresponds to an electric field of 0.48V/µm. This field is much larger than what was expected through estimating that the required electric field across any given diamond plate stays the same to maintain 100 percent charge collection efficiency. This indicates that the required field should be approximately 0.2V/µm, dictated by EGDS 1, which corresponds to a bias of +200V at the combined thickness of EGDSs 1 and 2.

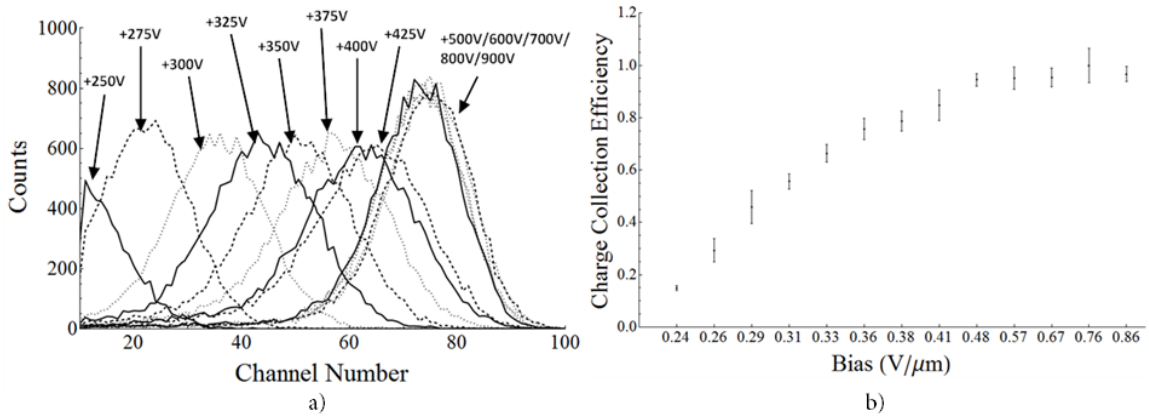

Figure 26: Measured ^{210}Po alpha spectra for a series multiplexed array of EGDs one and two is shown in a) and the determined charge collection efficiency versus applied electric field is shown in b).

Further, the maximum channel number reached was 77 ± 5 where it was channel 167 ± 6 for both EGDSs one and two. This is a factor of 0.46 ± 0.04 lower than for the single plate exposure results. This raises questions that need to be answered. A charge

sensitive preamplifier, such as the Ortec 142PC preamplifier utilized in this work, produces an output voltage equal to the ratio of the charge collected by the preamplifier to the capacitance of the feedback capacitor across the operational amplifier within its circuitry.[1] This property, however, is contingent on the fact that the total current pulse duration from the detector into the preamplifier is much less than the RC time constant of the feedback circuit across the operational amplifier in the preamplifier circuitry. The Ortec 142PC preamplifier has an RC time constant of 75μs and indicates that the current pulse duration must be less than 1μs. Work reported by M. Pomosrki *et al.* in 2006 indicated that the current pulse generated by an ^{241}Am alpha particle leaving an EGDS 325μm thick with an applied electric field of 1.23V/μm was essentially a square wave with a width of 5nm.[41] Similar current pulse widths should be arising from the EGDSs utilized in this work and indicates that the criterion on the use of a charge sensitive preamplifier for single plate diamond detectors is met.

This criterion is not necessarily met, however, in the case of a series multiplexed array. At this point the equivalent circuit of a diamond detector has not been taken into account. A diamond detection medium is actually a non-ideal capacitor, where the high resistance of the diamond impedes current flow across the diamond medium and creates charge build up on its electrodes. As such the equivalent circuit of a biased diamond detector is an ideal capacitor and resistor in series, where the ideal capacitor is the capacitance of the metalized diamond plate assuming no charge leakage between the plates and the resistor corresponds to the resistance of the diamond to current flow. A depiction of the front end electronics along with the equivalent circuit for

diamond connected to the preamplifier utilized in this work is given in Figure 27 a) and b), respectively. Now, when radiation interactions occur with the diamond plate electrons are liberated from the bound state within the valence band into the conduction band. Once in the conduction band they are free to move in the applied electric field across the diamond for subsequent detection in the charge sensitive preamplifier, where the transit time and trapping time constant dictate the efficiency of removing these generated electron-hole pairs before they are trapped within the diamond bulk. In this case the equivalent circuit is modified where a current source is added in place of the resistor in the RC equivalent circuit representing the diamond plate, as shown in Figure 27 c). In addition, since the diamond plate is also acting as a capacitor the creation and collection of charge due to the radiation interaction causes the charge on the electrodes to reduce, where in the equivalent circuit the created current pulse is discharging the front capacitor of the preamplifier, located next to I_1 and C_{D1}, as shown in Figure 27 a) and c), respectively. The high voltage power supply providing the bias to the sample then restores charge to the electrodes of the diamond plate thereby reestablishing an equilibrium state.

The charge collection efficiency measurements taken on all of the EGDSs indicate that near one-hundred percent charge collection at a voltage of ±175V. The current-voltage measurements taken on the diamond samples at this voltage are all around 10pA, which was used with Ohm's law to determine the resistance to be used in these simulations and turns out to be 15TΩ. Finally, based upon the dimensions of the

diamond the capacitance of all the EGDSs is around 1pF. These values will be used in the following simulations.

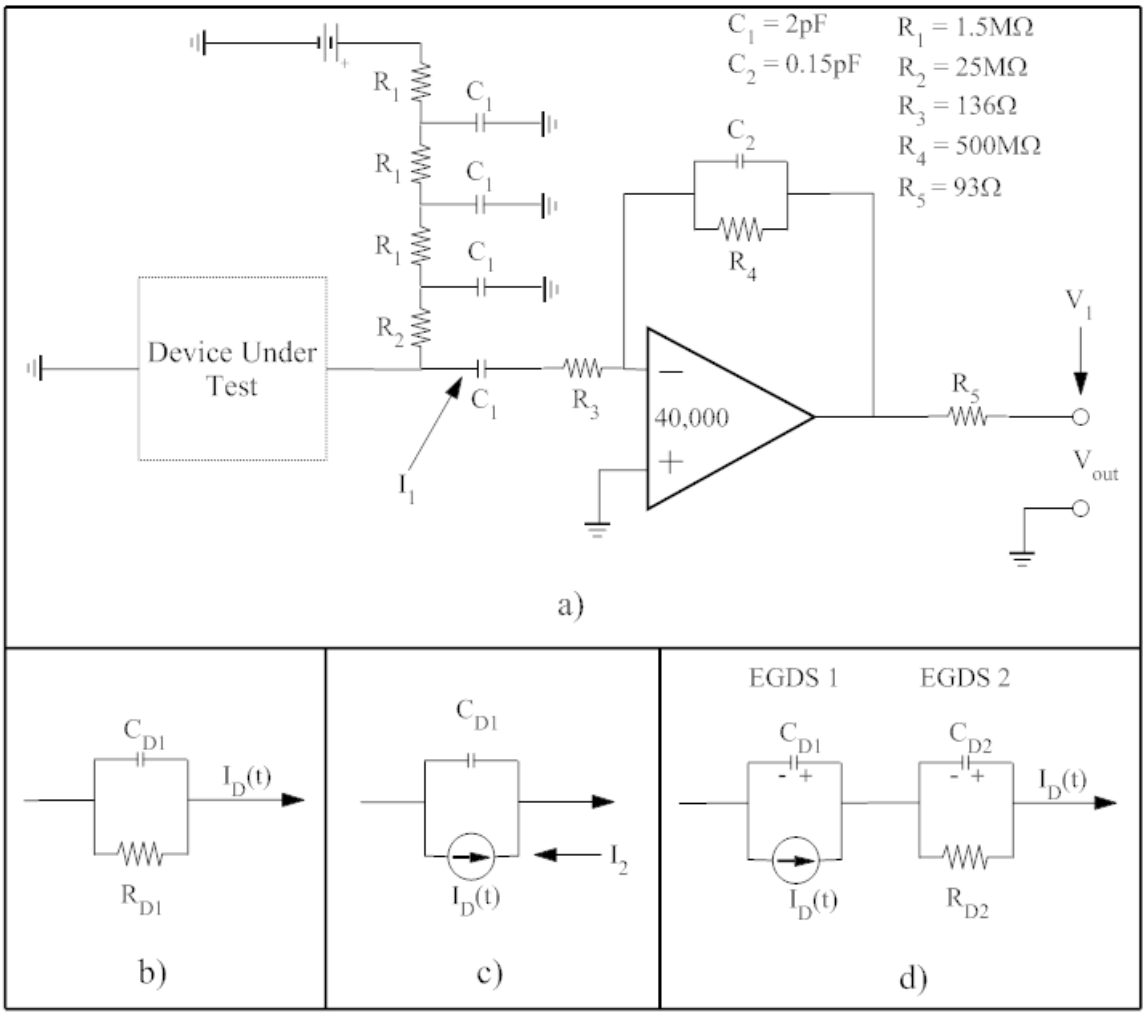

Figure 27: The simplified block diagram of the diamond detection system attached to the PC142 preamplifier in a) with b) a single diamond plate in bias, c) a diamond during a radiation interaction and d) two diamond plates in series where the diamond plate between the ground and the other diamond plate is under the influence of a radiation interaction.

The simulations on the equivalent circuits of multiplexed diamond arrays were conducted in Cadence® PSpice.[77] First, the description of the circuit was simulated to

estimate the response of the detection system as if an alpha particle of 5.5 MeV interacted with a diamond plate without losing any energy before entering the active detection volume. As such the total number of electrons that will be created, based upon a W-value of 13.2eV for diamond, is 416,667. It was assumed that a current pulse had a width of 5ns, similar to that quoted by M. Pomosrki *et al.* in 2006.[41] The current in the system was measured at locations I_1 and I_2 and the voltage output of the system was measured at the location V_1, as indicated in Figure 27 a) and c). The results from this simulation are given in Figure 28, where it can be seen that the voltage output from the preamplifier has a rise time that matches the input current pulse width, which is expected for a charge sensitive preamplifier. In addition, the decay of the output voltage from the preamplifier has a very long decay time constant, which is dictated by the RC time constant of the feedback circuit of the preamplifier, which is again the expected result for a charge sensitive preamplifier. The current pulse shown in part b) also indicates that the maximum current at the location I_1 is equal in magnitude to the current source, which is required for the proper voltage output of a charge integrating preamplifier. The maximum voltage output in this simulation from the preamplifier was determined to be -448.5mV.

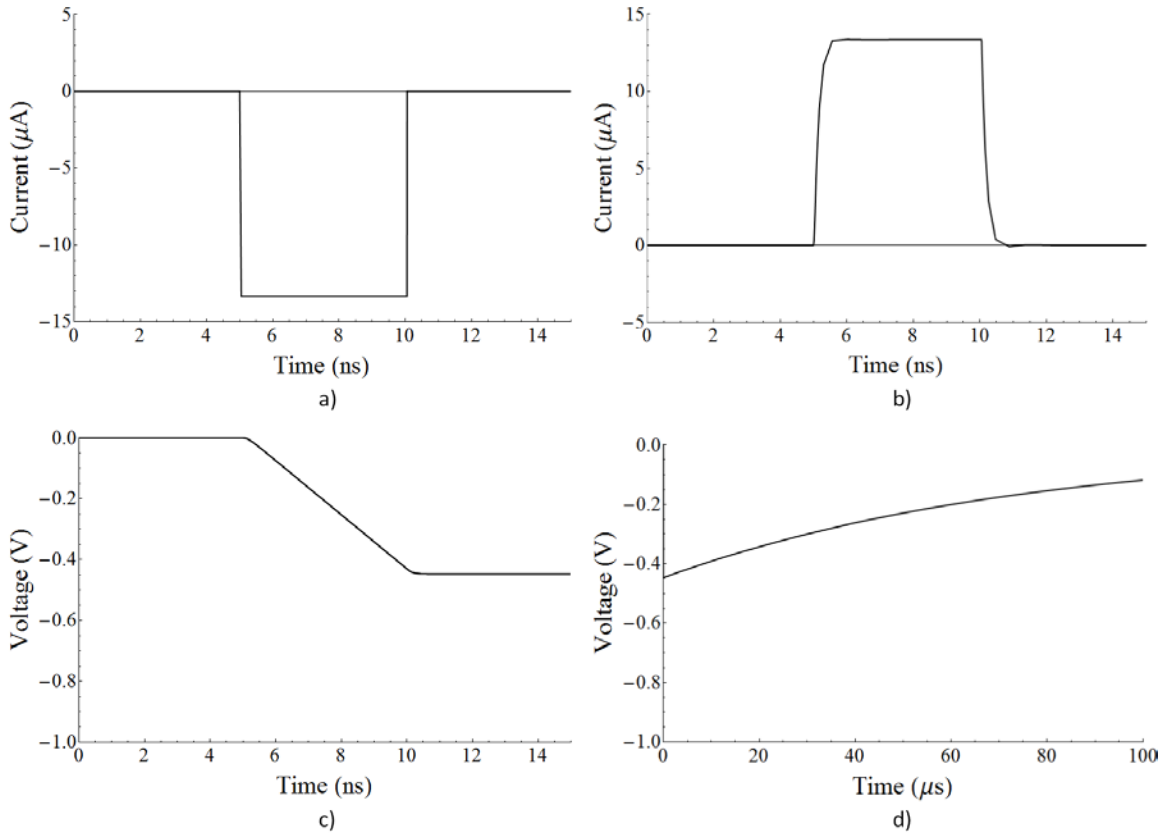

Figure 28: The current pulse introudced to the system is given in a), the current seen by the front end capacitor of the preamplifier is given in b), and the voltage rise and drop of the output of the preamplifier is given in parts c) and d), respectively.

Now that the functionality of the model has been verified for a single diamond detector a simulation was conducted that concerned the series multiplexing of two identical diamond plates. The circuit diagram of this multiplexed array is described in Figure 27 d). The diamond plate closest to the preamplifier, labeled EGDS 2 in the circuit diagram, is described as an RC circuit with the resistance determined through the IV measurements conducted on the diamond plates. The first diamond plate, labeled as EGDS 1 and has the interacting alpha particle and hence the current source, is identical in its equivalent circuit to the single diamond plate simulated previously and shown in

Figure 27 d). After the current pulse ends the current source location should be replaced with a resistor equal to the resistance of the diamond thereby becoming identical to the equivalent circuit of EGDS one. However, during a transient analysis in PSpice the elements in a circuit cannot be changed. Fortunately, the resistance of the current source to allow current to flow through itself is very high when the current source is off and was verified through noting that the potential between the two diamond plates in the circuit model was half of the total potential applied to the system. This indicates that the capacitor of EGDS 1 is charged to the appropriate value before the current source is turned on to simulate a series multiplexed array of two diamond plates and the subsequent resistance of the current source after the current pulse ends is large enough to act as the resistor in the resulting RC circuit after all created charge from the alpha particle interaction is transported out of the diamond.

Also note that the total amount of charge injected into the system from the current source is dictated by the bias across the plate and Hecht's theory. Therefore, it would seem to be that the best simulation technique would be to vary the total injected charge (time integrated current pulse) through the previously determined mobility-trapping time constant and Hecht's theory. However, of most interest is why the experimental results show an output voltage drop from the preamplifier in the series multiplexing of EGDS 1 and 2. As such a +700V bias was applied in this simulation since it was found that the channel number of maximum peak height did not increase with further voltage increases.

The results of the series multiplexing simulation of two diamond plates are given in Figure 29. In part a) the current pulse representing the charge generated from the alpha particle interaction is displayed and is identical to the current source used in the single plate simulations. In part b) the current entering the parallel capacitor to the current source in EGDS 1, labeled C_{D1}, is displayed. It can be seen that the current exiting the capacitor at the node peaks instantaneously to about 13.1μA and then quickly decays and holds a constant current of 6.7μA. The current at this point mainly stays constant for the duration of the current pulse at which point it spikes in the opposite direction to a current of -6.5μA**.** The value of the stable current across the capacitor in EGDS 1 is equal to the current in the capacitors of EGDS 2 and the preamplifier, as shown in Figure 29 c) and d), respectively. The output voltage pulse from the preamplifier has a rise time equal to the current pulse width and the decay time of this voltage pulse is hundreds of microseconds, both expected results for charge sensitive preamplifiers, as indicated in Figure 29 e) and f), respectively.

It should be pointed out here that the current spike at the beginning and end of the current pulse is expected as the parallel capacitor is supposed to be partially discharged by the current source due to the charge present on the capacitors in stable equilibrium and the sign/direction of the current pulse source representing a radiation interaction. However, the continuous current across EGDS 1 during the current source was not initially expected. In the single plate simulation these current spikes were rapid and quickly decayed to zero, but this was not the case in the series multiplexing simulation of EGDSs 1 and 2. This effect is due to the nearly equal impedances of EGDSs

1 and 2 means that the signal arising from EGDS 1 is partially loaded onto itself and onto EGDS 2. This loading of itself is the current seen on the capacitor of EGDS 1. The signal that goes into EGDS 2 sees the low load impedance at the input of the preamplifier and the resulting signal is amplified.

The sign of the charge that is on each capacitor in the equilibrium state before the current source is turned on due to the applied bias from the power supply is shown in Figure 27 d). The current coming out of the current source is negative. Therefore, the current can move to discharge the capacitor in parallel with it but it must actually charge the capacitor in EGDS 2. From the results it seems that the charging of this capacitor can only go so far in giving a signal across the RC circuit of EGDS 2 into the preamplifier because an equilibrium condition is reached between the current source injecting charge, the added voltage across the capacitor, and the capacitor in parallel with the current source. Therefore, less charge is injected into the preamplifier and the remaining charge is trapped in between the two RC circuits due to the extremely large impedances of the diamond plates. This is further verified by the fact that the voltage across EGDS 2 is increased by about 0.0332V. Using the capacitance of EGDS 2 and this voltage increase the value of the added charge to the system was determined to be 187,266 charges to maintain this voltage increase. Taking the ratio of this charge to the total charge released by the alpha particle interaction (equal to the integrated current pulse) yields a value of 0.45. This voltage increase is nearly identical in magnitude to the change in voltage across EGDS 1.

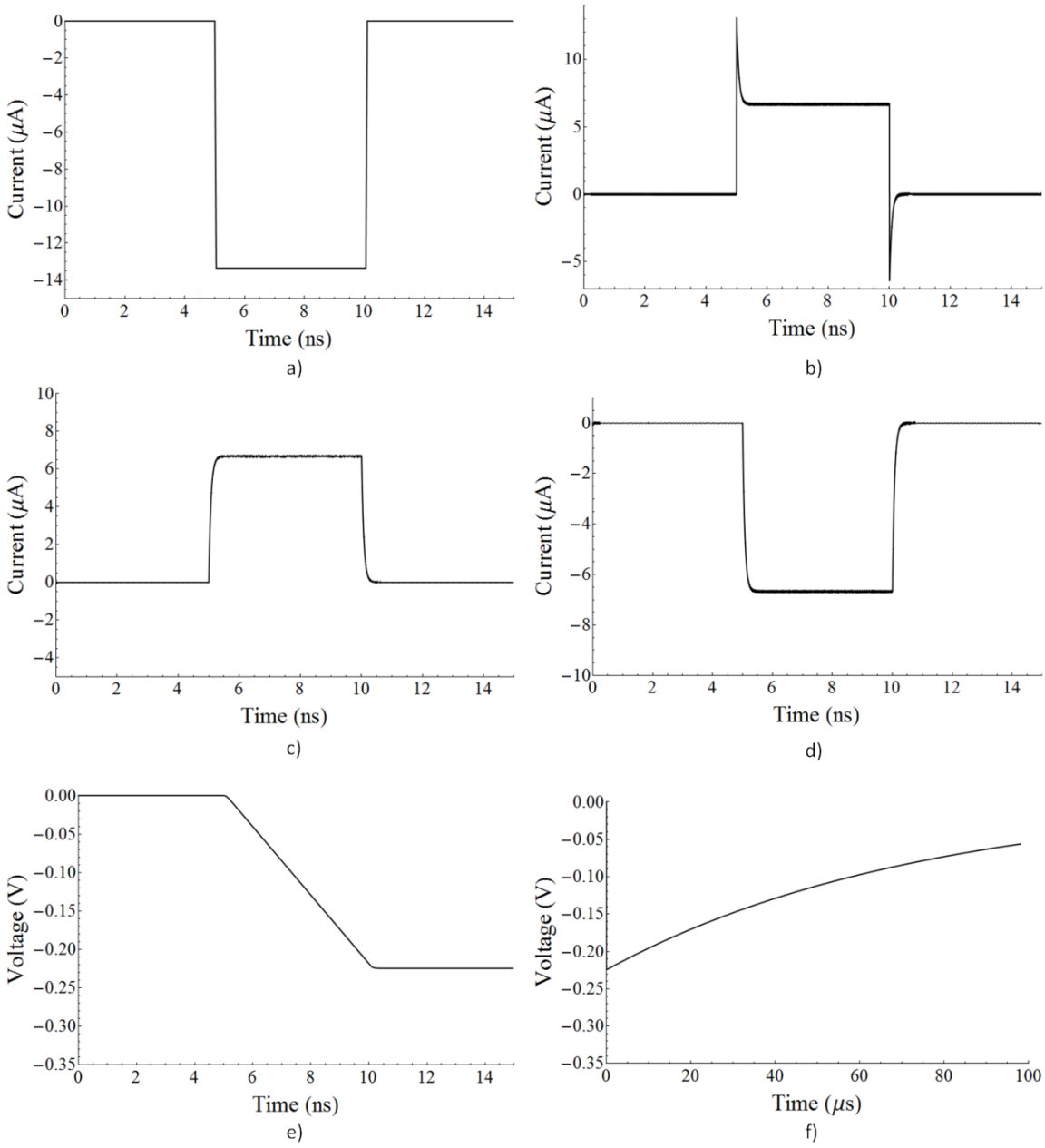

Figure 29: PSpice simulation results for the series multiplexing of two diamond plates in response to alpha particle interactions where a) the current pulse source, b) the current on the parallel capacitor with the current source or EGDS 1, c) the current on the parallel capacitor of EGDS 2, d) the current generated on front end capacitor of the PC142PC preamplifier, e) the voltage output rise and f) the decay of that voltage pulse from the 142PC preamplifier.

The output voltage from the preamplifier is given in Figure 29 e) and it is found that the maximum voltage produced is equal to -224.5mV. The voltage output in the case of a single diamond plate was found previously to be -448.5mV. Taking the ratio of these two results yields a value of 0.50 and agrees with the value obtained experimentally, which has been determined to be 0.46 ± 0.04. This value also agrees with the charge required to increase the bias across the RC circuits across the EGDSs as determined in the PSpice simulations. The experimental and verifying theoretical results presented here indicate that series multiplexing of diamond plates is inherently flawed due to the interaction of the liberated charge in one diamond plate with the rest of the multiplexed array and the associated electronics.

For the case of parallel stacking this evaluation will be conducted through neutron exposure experiments because the current detection system used for series multiplexing is not capable of testing a parallel multiplexed array of diamond plates for alpha exposures to only one of the diamond plates. In addition, the path traversed by an alpha particle when the parallel multiplexed array is close to the source varies greatly causing an energy broadening due to self-absorption of energy in its own containment and in air when not in a vacuum. Since the alpha source used in this work is not spectral grade this inherently limits the capability of testing a parallel multiplexed array of diamond plates utilizing the method used for the series multiplexed array.

6.5 Pu/Be Neutron Source and Parallel Multiplexing

The next step in the development of the neutron detection system is to expose the EGDSs to a neutron source. This work was conducted through the use of a Pu/Be

neutron source with a nominal source strength of $5\cdot10^6$ n/s. This source was chosen because of its larger number of neutrons above the detection threshold of a diamond detection system utilizing single neutron scattering (no thermalization). With this in mind it is now relevant to discuss the lower limit of detection of a diamond-based detection system. Utilizing a charge sensitive preamplifier, which is the best choice for accurate spectroscopy measurements,[78] there is an inherent lower limit of detection in the amplification of a current pulse resulting in a voltage signal above background noise. A charge sensitive preamplifier works by integrating the charge such that the output voltage is equal to the ratio of the collected charge from the radiation interaction to the value of the feedback capacitor but requires that the time it takes to collect the generated charge is much shorter than the RC time constant of the feedback circuit in the preamplifier. The basic theory of a preamplifier is that the voltage output, V, is proportional to the deposited energy in the detector, E, and inversely proportional to the product of the W-value of the detection material and the feedback capacitor in the preamplifier, W·C. Mathematically, the preamplifier's sensitivity can be described as

$$V = \frac{e*10^6}{\mathrm{W{\cdot}C}}\left(\frac{V}{MeV}\right). \qquad 13$$

For the Ortec 142PC preamplifier the value of C is 0.15pF and W is 13.2eV. This indicates that the voltage output per MeV of deposited energy in the diamond detection medium is 81mV. The average electronic noise at room temperature in the previously described electronic acquisition and data processing system is approximately 10mV peak to peak. This would seem to indicate that the lower limit of detection of a diamond-based neutron detection system using this electronic setup is 0.125 MeV of

energy deposition. However, at lower energy levels the only detectable neutron interaction that takes place is neutron scattering. Therefore, this would correspond to a neutron of 0.44 MeV. Of course this is at a maximum energy deposition as described through equation 1. Any energy deposition below this energy would not be registered above the noise floor. As such it takes a little larger neutron energy than the theoretical minimum to actually see a statistically significant effect in the pulse height spectrum protruding from the noise floor to higher channels. This has been seen to be the case in more than one study, where the noise floor in neutron detection has been determined to be an energy deposition of approximately 0.5 MeV,[20, 29] which corresponds to an impinging neutron energy of 1.76 MeV. Still, the argument supplied here implies that the lower limit of detection is more like a maximum energy deposition from a 0.7 MeV neutron.

This makes the use of a Pu/Be neutron source advantageous as the normalized number of neutrons emitted above 2 MeV to the total number of neutrons emitted is statistically higher than a typical fission neutron spectrum, as Figure 30 indicates through the comparison of a Pu/Be and ^{252}Cf neutron energy spectrums. The Pu/Be spectrum given was obtained from data reported in[79] and was scaled by a factor of ten so that a better comparison could be made to the ^{252}Cf spectrum. The latter's spectrum was determined through the use of a Maxwell energy spectrum, described by[12, 80]

$$N(E) = \frac{2\sqrt{E}}{T^{3/2}\sqrt{\pi}} Exp[-E/T], \qquad 14$$

where T is the temperature parameter, E is the energy of the emitted neutron, and N(E) describes the probability of the emission of the neutron at an energy E. The

temperature parameter can be found through noting that the transformation from the rest frame of the fission fragments to the laboratory frame, which yields the Watt spectrum, differs little from the Maxwell distribution. As such the temperature parameter can be found through[80]

$$T = T_w + \frac{2}{3}E_w, \qquad 15$$

where T_w is equal to 1.18 and E_w is equal to 0.36.

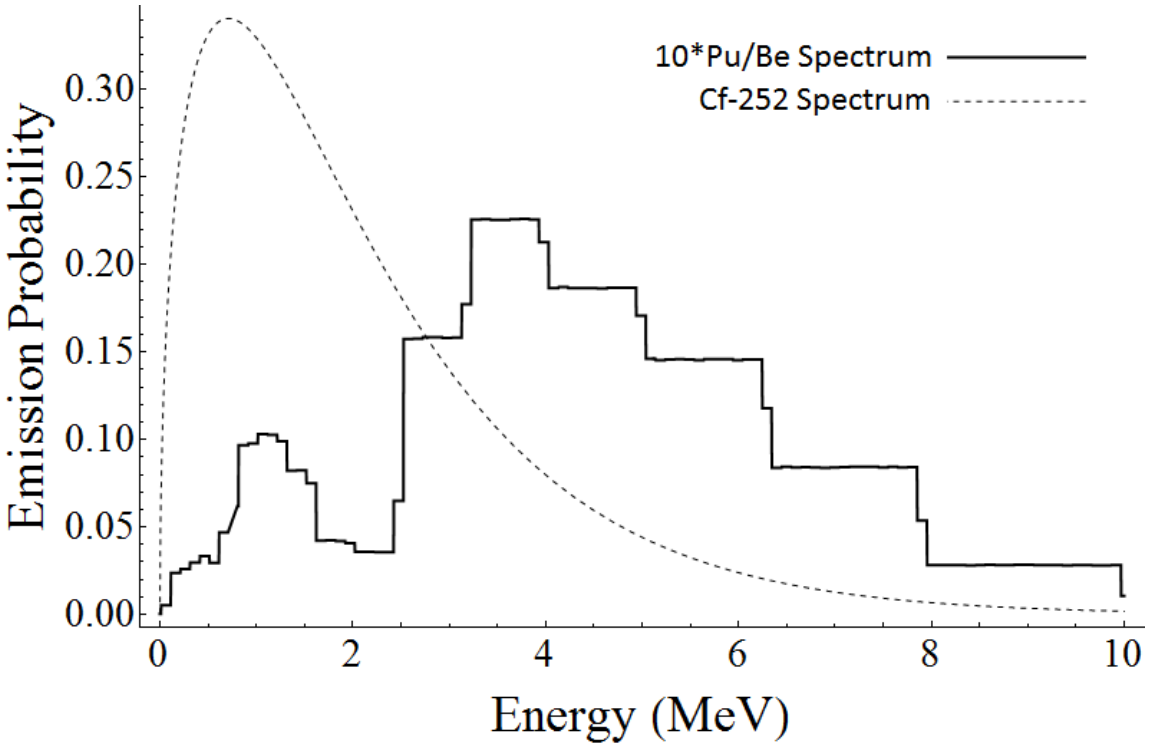

Figure 30: Neutron emission spectra for ^{252}Cf and Pu/Be neutron sources.

As was determined in the alpha particle exposures near one-hundred percent collection efficiency was obtained for all diamond plates at an applied bias of +175V and this was used in the neutron exposures of all diamond plates. The same detector

housing as shown in Figure 20 was used for the single plate exposures. The gain in these exposures was increased to 50 in this work to get a broader spectrum for a better comparison between experimental results across the diamond plates, which also indicates that neutron induced energy depositions above 2.5 MeV will not be registered in the pulse height spectrum and corresponds to a maximum energy transfer from an 8.8 MeV neutron elastic scattering event. A ^{3}He detector was placed close to the source during the measurements and was placed inside of a high density polyethylene cylinder for neutron moderation. The signal generated was passed through a single channel analyzer and a counting card was used to determine the total number of counts that was registered by the ^{3}He detector during the exposures of the EGDSs. This allowed for the determination of the relative detection efficiency of the diamond plates to the ^{3}He detector. A picture of the experimental setup is given in Figure 31. All of these neutron experiments were conducted with an acquisition time of 1000 seconds. The spectral results obtained for EGDSs 1-8 are given in Figure 32. Note that a background spectrum was obtained for these diamond samples with no neutron source nearby and the gain was low enough that no significant counts in the pulse height spectrum existed.

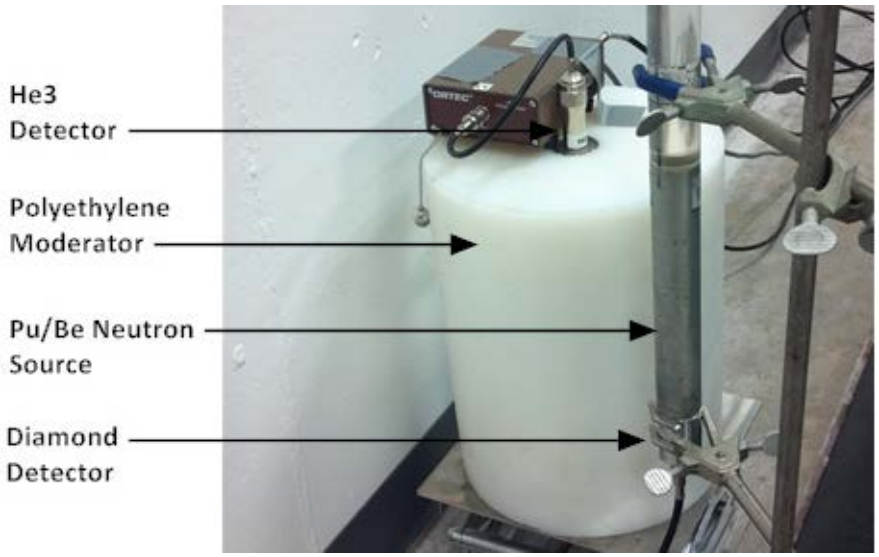

Figure 31: Experimental setup of the exposure of each EGDS to a Pu/Be neutron source.

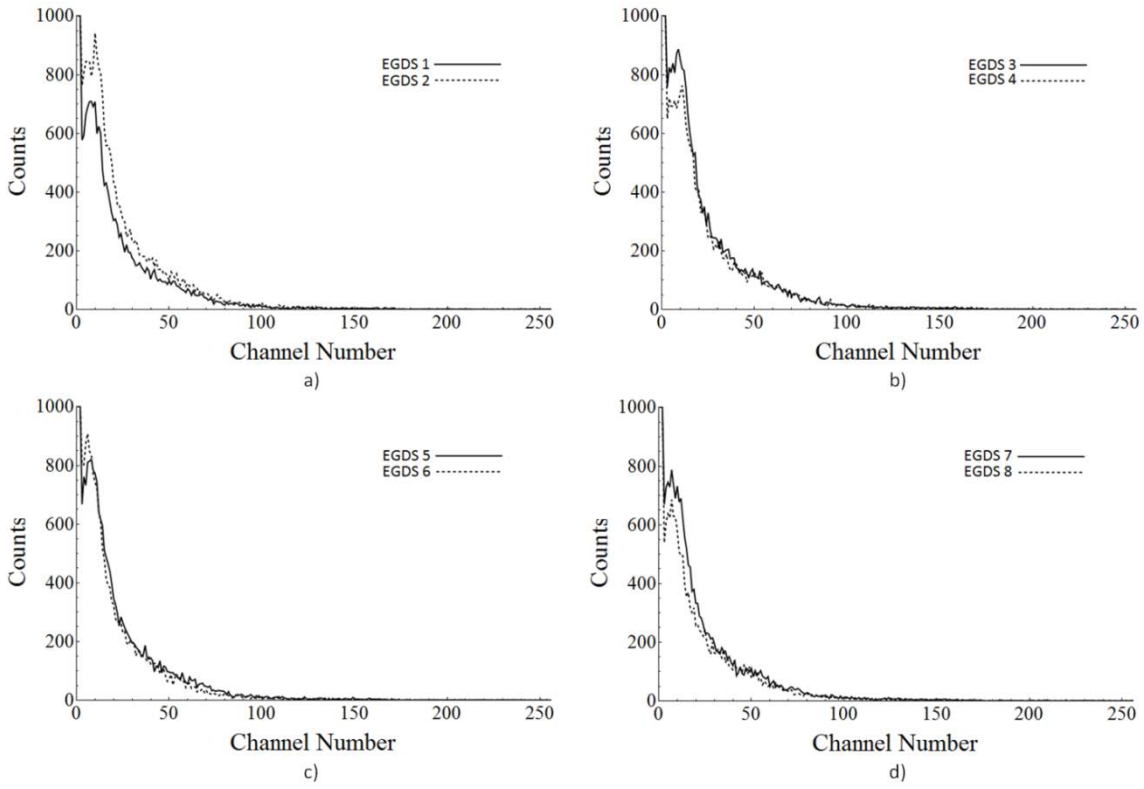

Figure 32: Measured pulse height spectrum induced by a Pu/Be neutron source on EGDSs a) one and two, b) three and four, c) five and six, and d) seven and eight.

The results shown indicate that all the EGDSs produce the same response from exposure to the Pu/Be source, where the main difference lies in the relative height of the observed spectrum for a given diamond plate. Further, the ratio of the integrated pulse height spectrum displayed to the total number of counts observed from the ^{3}He detector during the exposures is given in Table 10. This data indicates that the relative efficiency of the single plate diamond detector in the given configuration is relatively high and is attributed to the closeness of the diamond detector to the Pu/Be source and the lack of need to moderate the neutrons for detection. The large spread in the relative efficiencies between the EGDSs is attributed to the uncontrolled means by which the contacts were made, as very small differences in the electrode size or configuration on a given plate can correspond to very large relative changes in the active detection volume, and to the uneven diamond crystal dimensions.

Table 10: Determined relative efficiency of each EGDS in response to a Pu/Be source compared to the number of counts measured from a heavily moderated ^{3}He detector.

EGDS	1	2	3	4	5	6	7	8
Relative efficiency (%)	0.60	0.79	0.84	0.76	0.74	0.70	0.73	0.62

After these measurements were taken EGDSs 1-8 were all mounted onto a CPGA electronic package using a conductive silver epoxy. After curing the silver epoxy the EGDSs were wire bonded together in a parallel configuration through connecting all of their top sides together to a single bias source. A picture of the finished product is given in Figure 33.

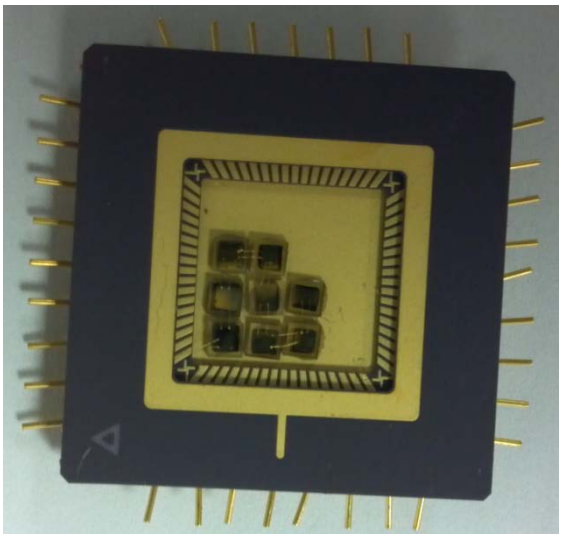

Figure 33: Picture of the parallel multiplexing of EGDSs 1-8.

This chip was mounted in an aluminum electronic enclosure insulated from the chamber wall. The surface of the diamond was approximately 1cm from the top of the electronic enclosure and the cylindrical Pu/Be source was placed directly over the location of the parallel multiplexed array. The same operational conditions that were used for the single plate exposures were used here. The result of this exposure to the parallel multiplexed array is given in Figure 34. The relative efficiency found for the parallel multiplexed array compared to the ^{3}He detector was found to be 3.14 percent. Summing the data listed in Table 10 yields a total relative detection efficiency of 5.77 percent. The differences seen are most likely due to a geometrical detection efficiency change between single plate and parallel multiplexed array exposures. This claim requires further investigation.

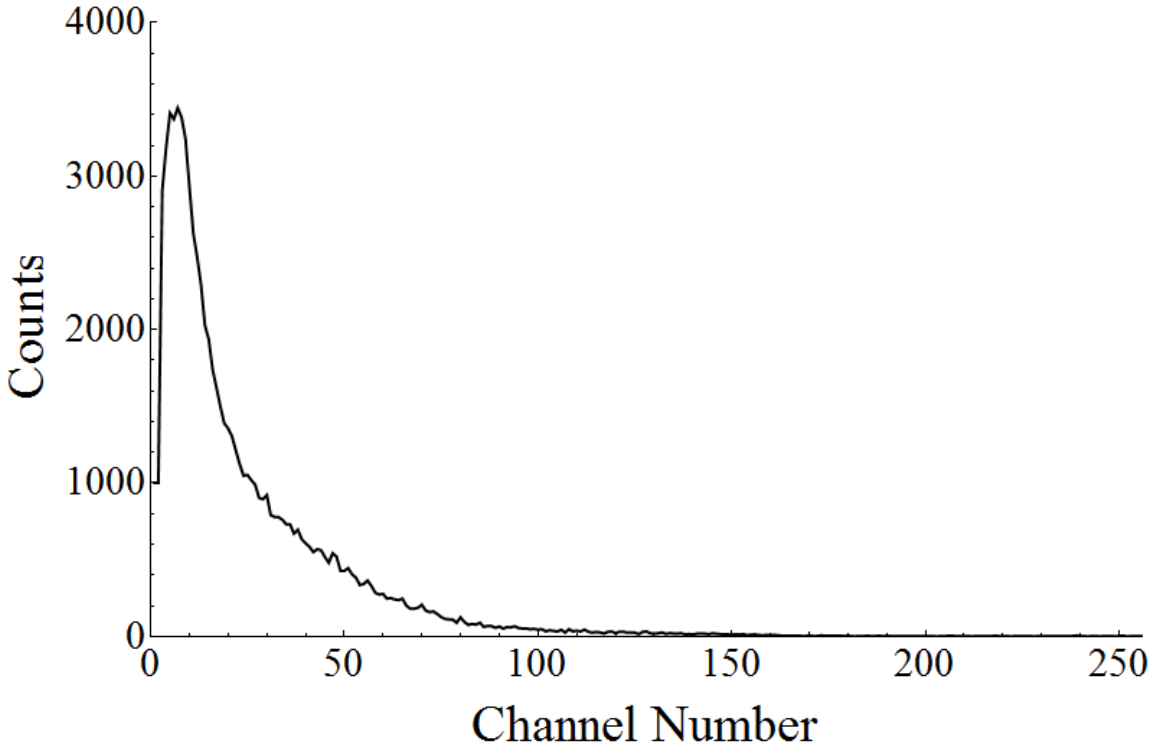

Figure 34: Spectral response of parallel multiplexed EGDSs 1-8 to a Pu/Be neutron source.

To account for the differences seen in the relative detection efficiency with respect to the ^{3}He counter for the single plate and parallel multiplexed array MCNPX simulations were conducted to take into account the geometry of the measurement system. The ISABEL/Dresner physics models were used in these simulations. The geometry of the parallel stacked array was such that the bottom surface of the Pu/Be source was approximately one centimeter away from the top of the diamond array whereas in the single plate exposures the diamond plates were only about 0.125cm away. It was found that the ratio of the total number of neutrons entering the single diamond plates to the parallel multiplexed array was 51 $\pm$ 3 percent. Multiplying this to the summed relative detection efficiencies given in Table 10 yields a total efficiency of

3.0 $\pm$ 0.2 percent. This value agrees well with the experimentally determined relative detection efficiency of the parallel multiplexed array of EGDS 1-8 of 3.14 percent.

During these simulations a pulse height spectrum was also generated and is given in Figure 35. Note that simulation parameters were designed that the figure shown is normalized to the intrinsic detection efficiency of the diamond plate. As can be seen the number of pulses expected drops to insignificant values above a neutron energy of 1.5 MeV. Looking at the experimental results it can be seen that this occurs at a channel number of approximately 100. This corresponds to a voltage input of 3.91V and therefore a deposited energy of approximately 1 MeV through solving back through the sensitivity of the Ortec 142PC preamplifier. This is a factor of one-third below the theoretical pulse height spectrum utilizing the ISABEL/Dresner physics models, but the model here did not take into account the partial thermalization of the hard neutron spectrum due to the room. In addition, it has already been pointed out that the ISABEL/Dresner physics models do not accurately model diamond detectors and so this result is mainly qualitative in that the same general shape in the pulse height spectrum is seen between the two, which is the expected result.

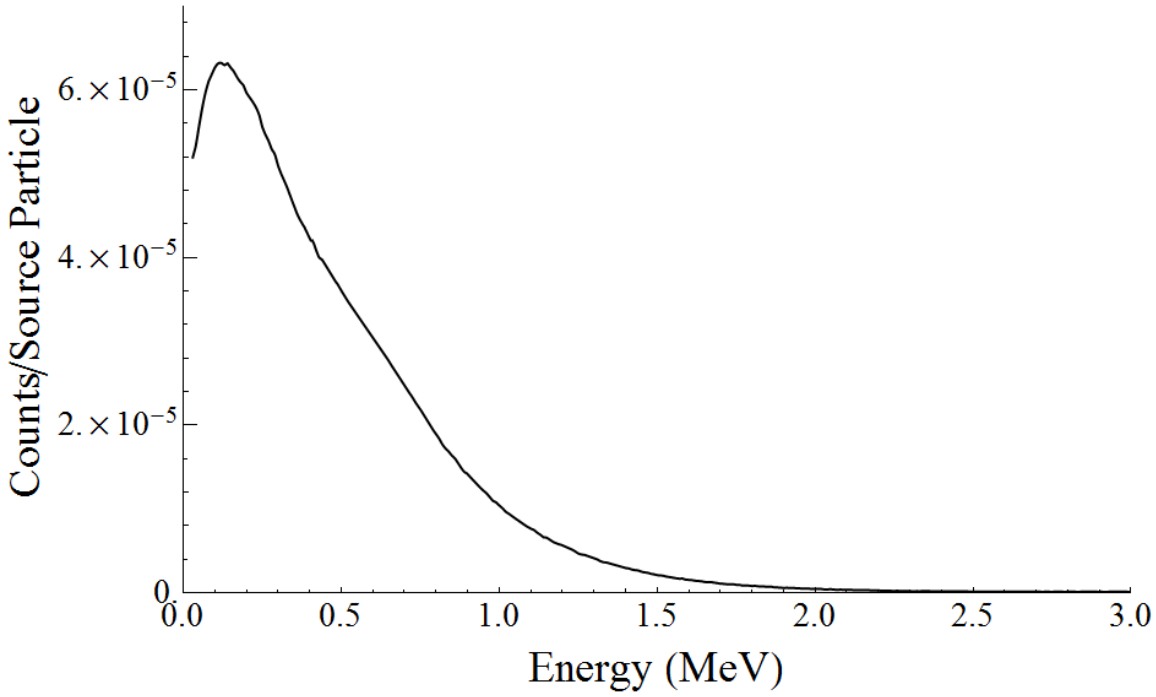

Figure 35: MCNPX simulation results for the expected pulse height spectrum on a single diamond plate using a Pu/Be source.

Finally, it should be noted that, as the number of parallel plates in the multiplexed array increases, the dark current of the system increases. In addition, the input capacitance to the preamplifier also necessary increases. The effect of these two changes to the preamplifier input/output were investigated in PSpice as seven RC circuits, as shown in Figure 27 b), in parallel with one current source in parallel to a capacitor, as shown in Figure 27 c). The same values were used for this simulation as the others except that the off-state current of the current source was varied between that seen through one diamond plate to that of eight diamond plates. It was found that this minimal increase in the current before and after the current pulse simulating a radiation interaction did not affect the results. However, the addition of seven more capacitors

and seven resistors did affect the system. The results are given in Figure 36. In a) the current across one of the parallel capacitors to the current source is given and this result is identical to that across all capacitors to the current source. It can be seen that the rapid spike, which is expected, has a very long decay time, which is not consistent with a single diamond plate. In Figure 36 b) the current across the input capacitor to the preamplifier is given where it is shown that the charging and discharging time is much larger than it was in the case of a single diamond plate. It can be seen that the current value across this capacitor very closely approaches the source current value. The voltage output shown in Figure 36 c) and d) indicate that the maximum voltage achieved was 1.5mV lower than for a single diamond plate and the discharging time was also longer. Also note that the time it takes for the voltage source to reach maximum value before starting its long decay is a little longer than in the case of one diamond plate.

A test was conducted that increased the capacitance further and it was found that the maximum current seen across the input capacitance starts to become less than the current source value and the time to maximum voltage output increased significantly with a much lower total voltage output. This indicates that there is a limitation to parallel multiplexing in that the signal for lower energy depositions will become lost due to the added input capacitance, although the system can still maintain a proportionality to the generated charge as long as this extra added capacitance is taken into account. Finally, it should be noted that the Ortec 142PC preamplifier, like similar charge sensitive preamplifiers, has its intrinsic noise increased as the input capacitance increases, such that the lower threshold of detection also increases, where

the input capacitance of this preamplifier is quoted by the manufacturer to allow only an input capacitance between 0-100pF.

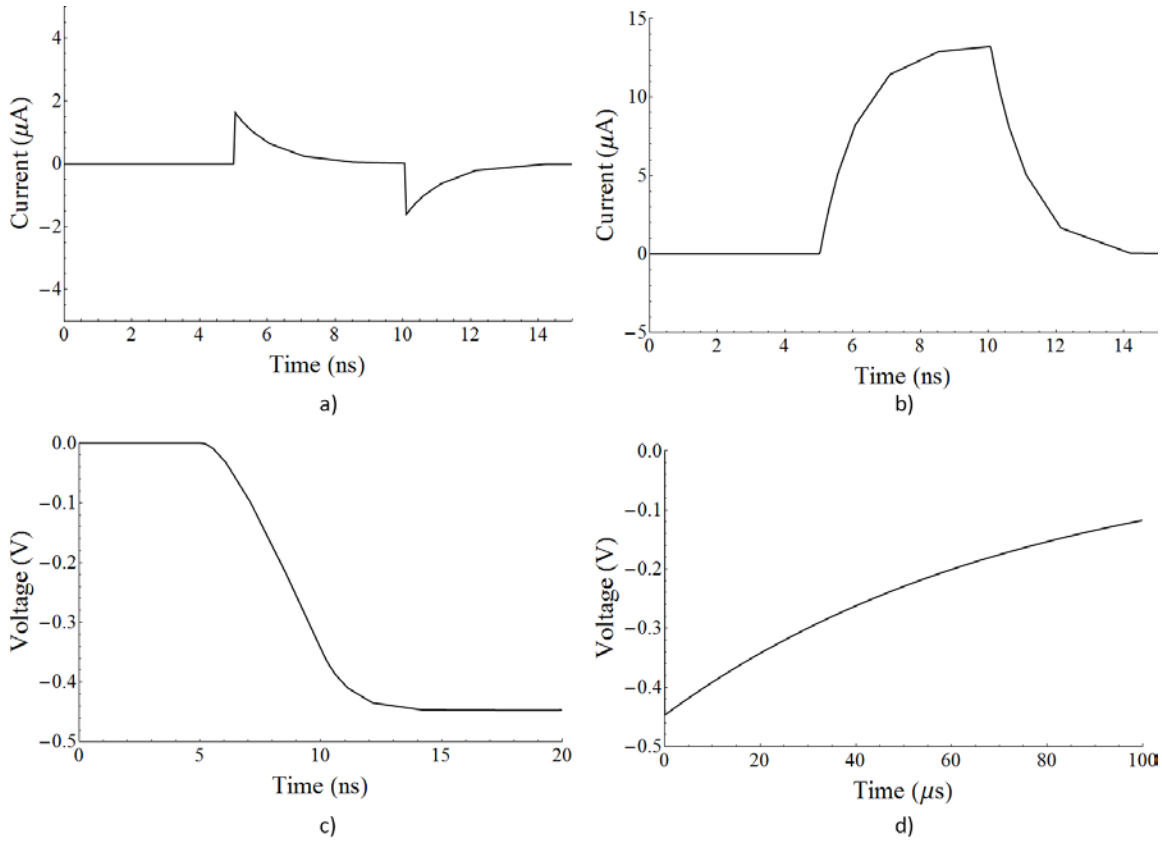

Figure 36: PSpice simulation results for the parallel multiplexed array for EGDSs 1-8. In a) the current across one of capacitors parallel to the current source is given. In b) the current through the input capacitor to the preamplifier is shown, and in c) and d) the output voltage from the preamplifier is given.

7. CONCLUSION

The simulations in this work indicate that the intrinsic detection efficiency of a diamond-based neutron spectrometer can be increased using a reasonable number of commercially available electronic grade diamond plates. The models used in this work are not capable of highly accurate modeling of the response of diamond detection systems due to the uncoupled nature of secondary charged particles created from neutron interactions and the inaccuracy of the available physics models. However, the simulations were adequate to draw some conclusions on the capability of multiplexing. Of most importance is that the energy resolution suffers little through multiplexing the diamond plates in a series multiplexing configuration that increases the intrinsic detection efficiency as compared to other neutron detectors. It was also shown that photon interactions with diamond multiplexed arrays may inhibit the detection of lower energy neutrons, but could be accounted for through a secondary gamma ray detector such as an HPGe detector to unfold/correct the lower part of the energy spectrum in the event of high photon flux fields.

Experimental results indicate that series multiplexing of diamond plates is inherently limited when used with a charge sensitive preamplifier. The series RC circuits representing each diamond plate causes half of the current generated in a diamond plate located between ground and the other diamond plate in series with it to travel into its own parallel capacitor rather than into the associated electronics for detection. Each diamond plate that is added into the multiplexed array further reduces the output

voltage and indicates that the voltage required to collect any charge from the detection medium for actual detection quickly becomes unreasonable. However, parallel multiplexing has shown great promise. Experimental results indicate that the pulse height spectrum observed from a parallel array of eight diamond plates produces the same spectrum as a single diamond plate and the detection efficiency scales linearly with the number of plates in the multiplexed array. PSpice simulations indicate that this is indeed the case. However, as the detector input capacitance to the charge sensitive preamplifier increases, the time it takes for the charge to become integrated into the preamplifier increases. In actuality, this also increases the noise of the system, thereby lowering the energy threshold that can be detected. This indicates that this method does have some limitations. The number of diamond plates that can be multiplexed together using an Ortec 142PC preamplifier is theoretically 100 diamond plates with the properties of the plates used in this work.

It is important to note that the parallel multiplexing configuration can be made to satisfy various detection requirements, such as increasing both geometrical and/or intrinsic detection efficiencies. Whether the advancement of CVD diamond growth occurs or not, the same limitation exists because the input capacitance is directly proportional to the area of the contacts. Having thicker diamond plates will reduce the input capacitance, but this can only go so far due to charge collection efficiency concerns. Still, advancement in this area is vital as the simulated results presented indicate that a centimeter thick diamond crystal, with good intrinsic detection efficiency,

would have a lower input capacitance due to this thickness, thereby making larger scale diamond-based detection systems than reported here possible.

The areas that still need to be investigated in this work include the various stacking mechanisms that can be achieved with parallel multiplexing; only stacking that increased the geometrical efficiency of the detection system was investigated in this study. In addition, using conversion layers such as hydrogenous materials and ^{6}LiF thermal neutron conversion layers in multiplexed arrays can allow for the detection of both thermal and epithermal neutrons in addition to fast neutrons with good detection efficiency that will allow for one of the most diverse spectroscopic neutron detection systems available. Finally, looking at the signal acquisition electronics to see if the capacitance input limitation can be overcome is also something that should be investigated to increase the scale of parallel multiplexed diamond arrays that can be achieved without advancing CVD diamond growth capabilities producing commercially available electronic grade single diamond crystals.

BIBLIOGRAPHY

1. G. F. Knoll, *Radiation Detection and Measurement*, 3rd ed. (Wiley, New Jersey, 2000).
2. G. Aigeldinger and A. Vance, (SAND2007-1570) (2007).
3. S. Vaughn, Air Force Institute of Technology, 2003.
4. D. Reilly, N. Ensslin and J. Hastings Smith, *Passive Nondestructive Assay of Nuclear Materials*. (Los Alamos National Laboratory, 1991).
5. G. Grosshoeg, Nuclear Instruments and Methods **162** (1-3), 125-160 (2002).
6. C. Leroy and P.-G. Rancoita, *Principles of Radiation Interaction in Matter and Detection*, 2nd ed. (World Scientific, Singapore, 2009).
7. A. Murari, T. Edlington, M. Angelone, L. Bertalot, I. Bolshakova, G. Bonheure, J. Brzozowski, V. Coccorese, R. Holyaka, V. Kiptily, I. Lengar, P. Morgan, M. Pillon, S. Popovichev, P. Prior, R. Prokopowicz, A. Quercia, M. Rubel, M. Santala, A. Shevelev, B. Syme, G. Vagliasindi and V. L. Z. R. Villari, Nuclear Instruments and Methods A **593**, 492-504 (2008).
8. D. A. Neamen, *Semiconductor Physics and Devices*, 3rd ed. (McGraw-Hill, New York, 2003).
9. A. N. Caruso, P. A. Dowben, S. Balkir, N. Schemm, K. Osberg, R. W. Fairchild, O. B. Flores, S. Balaz, A. D. Harken, B. W. Robertson and J. I. Brand, Materials Science and Engineering: B **135** (2), 129-133 (2006).
10. K. Osberg, N. Schemm, S. Balkir, J. I. Brand, M. S. Hallbeck, P. A. Dowben and M. W. Hoffman, IEEE Sensors Journal **6** (6), 1531-1538 (2006).
11. D. Emin and T. L. Aselage, Journal of Applied Physics **97** (2005).
12. C. A. Bertulani, *Nuclear Physics in a Nutshell*. (Princeton, UK, 2007).
13. M. A. Prelas, G. Popovici and L. K. Bigelow, *Handbook of Industrial Diamonds and Diamond Films*. (Marcel Dekker, New York, 1998).
14. A. V. Krasilnikov, E. A. Azizov, A. L. Roquemore, V. S. Khrunov and K. M. Young, Review of Scientific Instruments **68** (1), 553-556 (1997).
15. M. Pillon, M. Angelone and A. V. Krasilnikov, Nuclear Instruments and Methods B **101**, 473-483 (1995).
16. H. E. Spear and J. P. Dismuhes, *Synthetic Diamond: Emerging CVD Science and Technology*. (Wiley, New York, 1994).
17. J. Isberg, J. Hammersberg, E. Johansson, T. Wikstrom, D. J. Twitchen, A. J. Whitehead, S. E. Coe and G. A. Scarsbrook, Science **297** (2002).
18. National Nuclear Data Center, www.nndc.bnl.gov.
19. S. V. Gvozdev, V. V. Frunze and V. N. Amosov, Instruments and Experimental Techniques **52** (5), 637-645 (2009).
20. A. Zimbal, L. Giacomelli, R. Nolte and H. Schuhmacher, Radiation Measurements **45** (10), 1313-1317 (2010).

21. M. Pillon, M. Angelone, A. Krasa, A. J. M. Plompen, P. Schillebeeckx and M. L. Sergi, Nuclear Instruments and Methods in Physics Research A **640**, 185-191 (2011).
22. M. Pillon, M. Angelone, G. Aielli, S. Almaviva, M. Marinelli, E. Milani, G. Prestopino, A. Tucciarone, C. Verona and G. Verona-Rinati, Journal of Applied Physics **104**, 054513 (2008).
23. G. J. Schmid, J. A. Koch, R. A. Lerche and M. J. Moran, Nuclear Instruments and Methods in Physics Research A **527**, 554-561 (2004).
24. V. I. Polyakov, A. I. Rukovishnikov, N. M. Rossukanyi, V. G. Ralchenko, F. Spaziani and G. Conte, Diamond and Related Materials **14**, 594-597 (2005).
25. L. Jakubowski, M. J. Sadowski, J. Zebrowski, M. Rabinski, K. Malinowski, R. Mirowski, P. Lotte, J. Gunn, J.-Y. Pascal, G. Colledani, V. Basiuk, M. Goniche and M. Lipa, Review of Scientific Instruments **81** (2010).
26. A. Galbiati, S. Lynn, K. Oliver, F. Schirru, T. Nowak, B. Marczewska, J. A. Deunas, R. Berjillos, I. Martel and L. Lavergne, IEEE Transactions on Nuclear Science **56** (4), 1863-1874 (2009).
27. R. D. Benedetto, M. Marinelli, G. Messina, E. Milani, E. Pace, A. Paoletti, A. Pini, S. Santangelo, S. Scuderi, A. Tucciarone, G. Verona-Rinati and G. Bonanno, Diamond and Related Materials **10**, 698-705 (2001).
28. E. Pace, R. D. Benedetto and S. Scuderi, Diamond and Related Materials **9**, 987-993 (2000).
29. V. N. Amosov, E. A. Azizov, V. D. Blank, N. M. Gvozdeva, N. V. Kornilov, A. V. Krasilnikov, M. S. Kuznetsov, S. A. Meshchaninov, S. A. Nosukhin, N. B. Rodionov and S. A. Terent'ev, Instruments and Experimental Techniques **53** (2), 196-203 (2010).
30. S. Seltzer, (NIST Standard Reference Database 126, 2004), Vol. 2012.
31. S. Seltzer, (NIST Standard Reference Database 124, 2005), Vol. 2012.
32. R. S. Balmer, J. R. Brandon, S. L. Clewes, H. K. Dhillon, J. M. Dodson, I. Friel, P. N. Inglis, T. D. Madgwick, M. L. Markham, T. P. Mollart, N. Perkins, G. A. Scarsbrook, D. J. Twitchen, A. J. Whitehead, J. J. Wilman and S. M. Woollard, J. Phys: Condens. Matter **21** (2009).
33. G. Lindstrom, M. Ahmed, S. Albergo, P. Allport, D. Anderson, L. Andricek, M. M. Angarano, V. Augelli and N. Bacchetta, nuclear Instruments and Methods in Physics Research A **466**, 308-326 (2001).
34. A. Lohstroh, P. J. Sellin, S. Gkoumas, H. Al-Barakaty, P. Veeramani, M. E. Ozsan, G. Prekas, M. C. Veale, J. M. Parkin and A. W. Davies, Diamond and Related Materials **19**, 841-845 (2010).
35. S. Almaviva, M. Angelone, M. Marinelli, E. Milani, M. Pillon, G. Prestopino, A. Tucciarone, C. Verona and G. Verona-Rinati, Journal of Applied Physics **106**, 073501 (2009).
36. M. Angelone, M. Pillon, A. Balducci, M. Marinelli, E. Milani, M. E. Morgada, G. Pucella, A. Tucciarone, G. Verona-Rinati, K. Ochiai and T. Nishitani, Review of Scientific Instruments **77**, 023505 (2006).

37. M. Pomorski, E. Berdermann, W. d. Boer, A. Furgeri, C. Sander and J. Morse, Diamond and Related Materials **16**, 1066-1069 (2007).
38. E. Berdermann, M. Pomorski, W. d. Boer, M. Coibanu, S. Dunst, C. Grah, M. Kis, W. Koenig, W. Lange, W. Lohmann, R. Lovrincic, P. Moritz, J. Morse, S. Mueller, A. Pucci, M. Schreck, S. Rahman and M. Trager, Diamond and Related Materials **19**, 358-367 (2010).
39. P. Bergonzo, D. Tromson, C. Mer, B. Guizard, F. Foulon and A. Brambilla, Phys. Stat. Sol. (a) **185** (1) (2001).
40. S. Almaviva, M. Marinelli, E. Milani, G. Prestopino, A. Tucciarone, C. Verona, G. Verona-Rinati, M. Angelone, D. Lattanzi, M. Pillon, R. M. Montereali and M. A. Vincenti, Journal of Applied Physics **103** (2008).
41. M. Pomorski, E. Berdermann, A. Caragheorgheopol, M. Ciobanu, M. Kis, A. Martemiyanov, C. Nebel and P. Moritz, Phys. Stat. Sol. (a) **203** (12), 3152-3160 (2006).
42. P. Bergonzo, A. Brambilla, D. Tromson, C. Mer, B. Guizard, F. Foulon and V. Amosov, Diamond and Related Materials **10**, 631-638 (2001).
43. J. H. Kaneko, T. Tanaka, T. Imai, Y. Tanimura, M. Katagiri, T. Nishitani, H. Takeuchi, T. Sawamura and T. Iida, Nuclear Instruments and Methods in Physics Research A **505**, 187-190 (2003).
44. S. M. Sze and K. K. NG, *Physics of Semiconductor Devices*. (John Wiley & Sons, Hoboekn, New Jersey, 2007).
45. J. Isberg, J. Hammersberg, H. Bernhoff, D. J. Twitchen and A. J. Whitehead, Diamond and Related Materials **13**, 872-875 (2004).
46. Element Six, King's Ride Park, Ascot, UK.
47. E. Berdermann, M. Coibanu, S. H. Connell, A. M. O. D. d. Costa, L. Fernandez-Hernando, A.Oh and J. P. F. Sellschop, Phys. Stat. Sol. (a) **201** (11), 2521-2528 (2004).
48. M. Angelone, D. Lattanzi, M. Pillon, M. Marinelli, E. Milani, A. Tucciarone, G. Verona-Rinati, S. Popovichev, R. M. Montereali, M. A. Vincenti and A. Murari, Nuclear Instruments and Methods in Physics Research A **595**, 616-622 (2008).
49. D. Lattanzi, M. Angelone, M. Pillon, S. Almaviva, M. Marinelli, E. Milani, G. Prestopino, A. Tucciarone, C. Verona, G. Verona-Rinati, S. Popovichev, R. M. Montereali, M. A. Vincenti and A. Murari, Fusion Engineering and Design **84**, 1156-1159 (2009).
50. V. N. Amosov, S. A. Meshaninov, N. B. Rodionov and R. N. Rodionov, Diamond and Related Materials **20**, 1239-1242 (2011).
51. S. Almaviva, M. Marinelli, E. Milani, G. Prestopino, A. Tucciarone, C. Verona, G. Verona-Rinati, M. Angelone and M. Pillon, Applied Radiation and Isotopes **67**, S183-S185 (2009).
52. A. Pietropaolo, G. V. Rinati, C. Verona, E. M. Schooneveld, M. Angelone and M. Pillon, nuclear Instruments and Methods in Physics Research A **610**, 677-681 (2009).

53. P. Batistoni, M. Angelone, P. Carconi, U. Fischer, K. Fleischer, K. Kondo, A. Klix, I. Kodeli, D. Leichtle, L. Petrizzi, M. Pillon, W. Pohorecki, M. Sommer, A. Trkov and R. Villari, Fusion Engineering and Design **85** (7-9), 1675-1680 (2010).
54. D. B. Pelowitz, *MCNPX User's Manual*. (Los Alamos National Laboratory, 2011).
55. D. Brown, (Brookhaven National Laboratory, NNDC, 2011).
56. A. J. Koning and D. Rochman, 2011.
57. E. Padovani and S. A. Pozzi, (Polytechnic of Milan, 2002).
58. R. E. Prael and H. Lichtenstein, 1989.
59. Y. Chen, M. Ogura, S. Yamasaki and H. Okushi, Semiconductor Science and Technology **20**, 860-863 (2005).
60. M. Werner, Semiconductor Science and Technology **18**, S41-S46 (2003).
61. Y. Y. Wang, C. M. Zhen, Z. Y. Yan and Q. F. Guo, International Journal of Modern Physics B **16** (6 & 7), 927-931 (2002).
62. *Edition: Version* (Wolfram Research Inc., Champaign Illinois).
63. W. D. Ehmann and D. E. Vance, *Radiochemistry and Methods of Nuclear Analysis*. (John Wiley & Sons, New York, 1991).
64. L. Feng-Bin, W. Jia-Dao, C. Da-Rong and Y. Da-Yun, Chinese Physics B **18** (5), 2041-2007 (2009).
65. F. Maier, J. Ristein and L. Ley, Physical Review B **64** (2001).
66. C. Jany, F. Foulon, P. Bergonzo and R. D. Marshall, Diamond and Related Materials **7**, 951-956 (1998).
67. L. Rossi, P. Fischer, T. Rohe and N. Wermes, *Pixel Detectors From Fundamentals to Applications*. (Springer, Verlag Berlin Heidelberg, 2006).
68. G. Lutz, *Semiconductor Radiation Detectors*. (Springer, Verlag Berlin Heidelberg, 2007).
69. H. Gamo, M. N. Gamo, K. Nakagawa and T. Ando, Journal of Physics: Conference Series **61**, 327-331 (2007).
70. M. Yokoba, Y. Koide, A. Otsuki, F. Ako, T. Oku and M. Murakami, Journal of Applied Physics **81** (10), 6815-6821 (1997).
71. D. Doneddu, O. J. Guy, P. R. Dunstan, T. G. G. Maffeis, K. S. Teng, S. P. Wilks, P. Igic, D. Twitchen and R. M. Clement, Surface Science **602**, 1135-1140 (2008).
72. T. Tachibana, B. E. Williams and J. T. Glass, Physical Review B **45** (20), 11975-11981 (1992).
73. C. Zhen, X. Liu, Z. Yan, H. Gong and Y. Wnag, Surface and Interface Analysis **32**, 106-109 (2001).
74. D. A. Evans, O. R. Roberts, G. T. Williams, A. R. Veary-Roberts, F. Bain, S. Evans, D. P. Langstaff and D. J. Twitchen, Journal of Condensed Matter Physics **21** (2009).
75. W. Tsai, M. Delfino, D. Hodul, M. Riaziat, L. Y. Ching, G. Reynolds and C. B. Cooper, IEEE Electron Device Letters **12** (4), 157-160 (1991).
76. (Canberra Industries Inc., Meriden, CT, Genie 2000).
77. (Cadence Design Systems, Inc., Portland, Oregon, 2011).
78. R. S. Sussmann, *CVD Diamond for Electronic Devices and Sensors*. (John Wiley & Sons, West Sussex, U.K., 2009).

79. IAEA, "Compendium of Neutron Spectra and Detector Responses for Radiation Protection Purposes," 2001.
80. Martin and Karlsson, Lund Unversity, 1997.

VITA

Eric Lukosi was born on March 2, 1984 in Denver, Colorado. His high school career was split between two high schools, Alameda and Colorado's Finest. Eric played soccer throughout his youth and continued during his undergraduate studies at Benedictine College where he majored in Physics and Astronomy. From here he attended the University of Missouri to attain his Master of Science and Doctor of Philosophy in nuclear engineering with an emphasis in nuclear nonproliferation and neutron spectroscopy. While attending the University of Missouri he married Michelle Ismert.